SPATIAL STRUCTURE OF VERY LOW FREQUENCY MODULATED IONOSPHERIC CURRENTS

A DISSERTATION
SUBMITTED TO THE DEPARTMENT OF ELECTRICAL ENGINEERING
AND THE COMMITTEE ON GRADUATE STUDIES
OF STANFORD UNIVERSITY
IN PARTIAL FULFILLMENT OF THE REQUIREMENTS
FOR THE DEGREE OF
DOCTOR OF PHILOSOPHY

Joseph Allen Payne Jr.

August 2007

I certify that I have read this dissertation and that, in my opinion, it is fully adequate in scope and quality as a dissertation for the degree of Doctor of Philosophy.

_____

Umran S. Inan   Principal Adviser

I certify that I have read this dissertation and that, in my opinion, it is fully adequate in scope and quality as a dissertation for the degree of Doctor of Philosophy.

_____

Timothy F. Bell

I certify that I have read this dissertation and that, in my opinion, it is fully adequate in scope and quality as a dissertation for the degree of Doctor of Philosophy.

_____

Antony C. Fraser-Smith

Approved for the University Committee on Graduate Studies.

Abstract

The High Frequency Active Auroral Research Project (HAARP) heater has been used to generate Extremely Low Frequency and Very Low Frequency (ELF/VLF) electromagnetic radiation in the lower ionosphere since March 1999. The HAARP beam modulates the conductivity of the ionospheric plasma in a region where a small ambient electric field exists. This produces a modulated distribution of currents that primarily radiate at the modulation frequency.

In an attempt to image the structure of these currents, a set of nine interferometric instruments was built and deployed around the HAARP facility. Data was collected and an attempt was made to directly invert the measurements into a spatial current map. While providing some interesting comparison of inversion methods, the direct approach was unable to resolve the system to a scientifically useful accuracy and a second approach was needed.

Using a ray tracing algorithm that models the interaction of the HAARP HF beam with the ionospheric plasma, a set of three-dimensional conductivity maps are generated for a range of ionospheric profiles. These conductivity maps are transformed into a primary current map and then input into a Finite Difference Time Domain (FDTD) code which models the interaction of these primary source currents with the plasma.

The output of the FDTD simulation shows the formation of an upwardly directed whistler wave that propagates along the magnetic field. The simulations also show that a simple distributed current source coupled with a free space propagation model reasonably approximates the FDTD predicted ground-based electromagnetic fields. This simple model is compared with data collected at multiple recording sites during

the imaging campaign. The model predictions and the data are shown to be in substantial agreement.

Acknowledgment

After spending seven years in the VLF group at Stanford University, it is with a very small tinge of sadness that I finalize my dissertation to start the next chapter of my life. It has been a pleasure and an honor to work with the wonderful people in the VLF group, and I hope to have the opportunity to work with many of you again in the future.

First, I would like to thank my adviser, Professor Umran Inan for his remarkable dedication to research and for his tireless promotion of both the VLF group and his students. I am truly grateful for the experiences and research that I have been exposed to over the last few years. I am also very thankful for the help of Dr. Timothy Bell, someone who has spent many hours illuminating me on the intricasies of the continuity equation and on VLF heating in general. I would like to thank Professor Antony Fraser-Smith for many hours of enlightening discussion on any number of interesting topics. I would especially like to thank Piero Pianetta for chairing my oral defense committee.

Jeff Chang played many roles in the Interferometer Campaign, from layout and assembly all the way through deployment. Without Jeff's help, this work would never have gotten off the ground, and I thank him sincerely. Tim Chevalier also had many roles, including designing the antenna structures, helping to deploy three antennas, and allowing me to use his FDTD code to model current formation in the ionosphere. Henceforth, I propose to call said FDTD code, the "Graduator".

I would also like to thank the entire crew who helped deploy the instrumentation, which included Ben Cotts, Mark Golkowski, and Jeff Chang. The "Antenna Site Setup" campaign included some of the worst days of my life, but watching these

three suffer actually made my days tolerable. Robb Moore, Tim Chevalier, and Troy Wood also helped erect three antennas a month before the main campaign. Without their work, there is no way that we could have completed all nine units in the time alloted.

Mike McCarrick, Dave Seafolk-Kopp, and Marty Karjala were all instrumental in keeping the HAARP facility running during the Stanford Interferometer Campaign, and I thank them for their time and expertise. Additionally, the owners of the Chistochina B&B, Norma and Doyle Traw, took excellent care of me and the other members of our deployment crew, and I thank them for their support. Finally, Gene Wescott helped a great deal in obtaining site permits for our receivers and in determining optimum receiver locations.

I would like to thank Robb Moore, both for constant enlightening discussions and for the explanation and access to his HF modulation code upon which my HF code is heavily based. Without Robb, my path to graduation would have been extended by many months and for this help, I am sincerely grateful.

I would like to thank Forrest Foust for taking Tim Chevalier's code and adapting it to model ionospheric currents. Forrest saved me several months of coding and did a fantastic job getting the code to run efficiently and stably.

This work would not have been possible if it were not for the love and support of my family. My parents, Joseph and Diane, have supported me through my entire academic career and have reassured me that seven years is NOT a long time to graduate!

Words cannot express the love and gratitude that I feel toward my beautiful wife Amy. Amy has put up with my compulsive work schedule and has stood by me for the last three years, gently nudging me forward. Without her banning the purchase of a Nintendo Wii until after thesis completion, I would probably have spent another year in graduate school.

JOSEPH A. PAYNE JR.

Stanford, California
August 1, 2007

Contents

List of Tables

List of Figures

Chapter 1

Introduction

Since completing initial construction work in March 1999, the High Frequency Active Auroral Research Project (HAARP) heater has been used to generate Extremely Low Frequency and Very Low Frequency (ELF/VLF) electromagnetic radiation in the lower ionosphere. While not consistent in the literature, a commonly used division of bandwidth classifies the spectrum from 20 Hz to 3 kHz as the ELF band, while the spectrum from $3-30$ kHz is classified as the VLF band [*Tascione*, 1994, p117]. This radiation is generated by modulating the Earth's natural auroral electrojet current with a focused High Frequency (HF) radiowave. As the plasma in the lower ionosphere absorbs energy from the wave, the electron temperature is altered, modulating the Hall, the Pedersen, and the Parallel conductivities of the plasma. The change in conductivities produces currents which generate the observed ELF/VLF radiation [*Stubbe and Kopka*, 1977]. There have been several attempts to theoretically deduce the structure of these ionospheric electrojet currents produced by modulated HF heating. However, the campaign that led to the data used in this dissertation constitutes the first attempt to empirically image the three-dimensional structure of such currents. Figure 1.1 illustrates the HF to VLF conversion process.

The purpose of the Stanford VLF Interferometer Campaign is to characterize the three-dimensional structure of the modulated electrojet currents from ground electromagnetic observations and compare the result to the theoretical models. It is hoped that better spatial knowledge of the modulated electrojet currents may lead
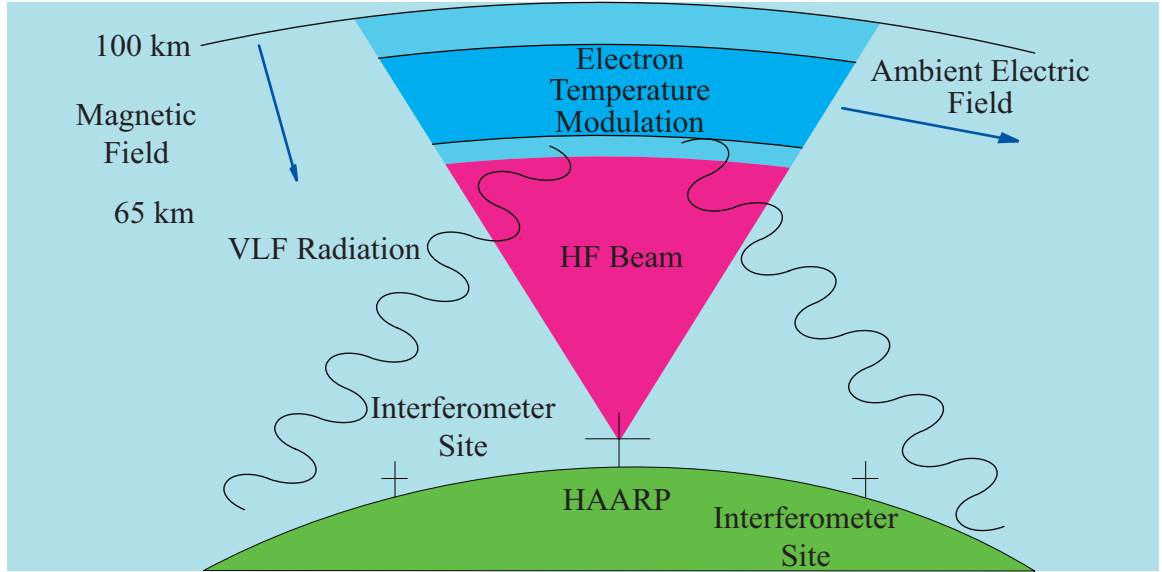
Figure 1.1: Cartoon showing VLF modulation of the D-region of the ionosphere. The pink

to better methods of generation with increased HF to ELF/VLF coupling efficiency.

The purpose of this thesis is to describe the Interferometer Campaign beginning with the construction of the autonomous ELF/VLF receiver units and ending with the determination of ionospheric currents. Chapter 1 provides a basic understanding of the ionosphere and discusses past experimental and theoretical work on HF to VLF conversion. Chapter 2 details the design and construction of the Interferometer Units, the performance of the devices, and discusses the Interferometer Campaign. Chapter 3 describes the direct L_1 norm minimization technique used to estimate ionospheric currents from received VLF data, and the practical reasons why this method was unsuccessful. Chapter 4 discusses the forward modeling techniques, including the theoretical methods to determine the conductivity modulation above an HF heater. The output of the HF heating model is fed into a full wave plasma interaction Finite Difference Time Domain (FDTD) code that estimates the response of the ionospheric plasma to the change in conductivity. Chapter 5 shows actual data and discusses the comparison of this data to the theoretical predictions. In Chapter 6, a brief summary is given and some ideas for future experiments are offered.

1.1   The Ionosphere

The ionosphere was first postulated by Lord Kelvin in the late 19th century as a conducting medium separating the neutral atmosphere and near-Earth space. This conducting medium can be attributed to photoionization of the Earth's atmosphere, ionizing cosmic radiation, and energetic electron precipitation which work together to produce a weakly ionized plasma that extends from 50 to 70 km at its lower limit to approximately 2000 km at its upper limit. The effects of this plasma layer were observed in long distance radio transmissions first attempted in the early 20th century [*Tascione*, 1994, p89].

A major source of electron dissociation during daytime in the lower ionosphere is the alpha ionization of nitrogen oxide through the absorption of solar x-rays [*Reid*, 1976]. The strength of these x-rays is dependent both on solar activity and the inclination of the sun with respect to the ionosphere. At nighttime, the total ionization of the lower ionosphere decreases substantially as the primary dissociation method is removed. However, energetic electrons precipitating from the radiation belts [*Potemra and Zmuda*, 1970; *Reid*, 1976], ionizing galactic cosmic rays [*Ratcliffe*, 1972, p19], and ionizing alpha radiation scattered from the exosphere all help to support the ionization of the lower ionosphere at night [*Davies*, 1990, p57].

In addition to the temporal and diurnal variation of the ionosphere, the ionosphere also varies strongly with geomagnetic latitude. This variation can be coarsely modeled by separating the ionosphere into three regions: low-latitude, mid-latitude, and high-latitude. The low-latitude ionosphere has a nearly horizontal magnetic field, leading to an intense current sheet known as the equatorial electrojet that flows an altitude of approximately 100 km [*Tascione*, 1994, p103]. The mid-latitude ionosphere is generally free of the phenomena associated with a horizontal magnetic field, and is also free of the influence of energetic particle precipitation associated with the auroral zone [*Tascione*, 1994, p104]. The high-latitude ionosphere is directly coupled to the magnetospheric tail by the stretched auroral magnetic field lines [*Tascione*, 1994, p89]. Because the Stanford Interferometer Campaign was held at night in Alaska, the high-latitude nighttime ionosphere is relevant for this dissertation.

In this section, some basic terminology and background regarding the ionosphere are addressed that prove important throughout this thesis.

1.1.1 Weakly Ionized Plasma

The ionosphere is composed of an anisotropic cold plasma that strongly interacts with radiowaves propagating through it [*Budden*, 1985, p4]. The dominant plasma constituent to consider for propagation at radio frequencies is the electrons, as the ions are too massive to respond to a quickly changing electric field. Because of the presence of the Earth's magnetic field, the plasma in the ionosphere is anisotropic, meaning that the plasma responds differently to an electric field applied in different directions [*Budden*, 1985, p4-5].

It is convenient to represent the current density generated in a magnetized plasma in response to an applied electric field by using a conductivity tensor as shown below.

$$
\begin{bmatrix} J_x \\ J_y \\ J_z \end{bmatrix} = \begin{bmatrix} \sigma_P & \sigma_H & 0 \\ -\sigma_H & \sigma_P & 0 \\ 0 & 0 & \sigma_{||} \end{bmatrix} \begin{bmatrix} E_x \\ E_y \\ E_z \end{bmatrix} \tag{1.1}
$$

In Equation 1.1, the magnetic field is aligned along the $\hat{\mathbf{z}}$ direction, σ_P represents the Pedersen conductivity, σ_H is the Hall conductivity, and $\sigma_{||}$ is the Parallel conductivity. The resultant currents that are generated due to the Pedersen, Hall, and Parallel conductivities are respectively known as the Pedersen, Hall, and parallel currents [*Bittencourt*, 2003, p245].

The conductivity tensor and its different components are discussed in greater detail in Chapter 4.

1.1.2 Chapman Layers

A model to estimate the altitude profile of ionization in the ionosphere was first proposed by Sydney Chapman [*Tascione*, 1994, p90], who studied the absorption of parallel rays of monochromatic radiation obliquely striking the Earth's upper atmosphere. While his assumptions were simplistic, the so-called Chapman model provides

a framework for studies of ionospheric phenomena.

A simple Chapman layer is defined as

$$N_e(z) = (\frac{q_{\mathrm{m}}}{\alpha_{\mathrm{eff}}})^{1/2} \exp^{\left[\frac{1}{2}\left(1 - z_1 - \exp^{-z_1}\right)\right]} \tag{1.2}$$

$$z_1 = \frac{z - z_{\mathrm{m}}}{H} \tag{1.3}$$

where z_{m} is the height of maximum ionization, q_{m} is the maximum production rate, α_{eff} is the effective recombination rate, and H is the scale height of an assumed exponential atmospheric density [*Tascione*, 1994, p90-91].

To accurately model the ionosphere, a number of Chapman layers are constructed with appropriate values of z_{m}, q_{m}, and α_{eff}. These well chosen layers are labeled the D, E, F1, and F2 regions, the superposition of which constitutes an ionization model that approximates the actual ionosphere [*Tascione*, 1994, p92]. For the Stanford Interferometer Campaign, only the D and the lower part of the E-region are relevant as nearly all of the HF energy gets absorbed at the base of the ionosphere [*Stubbe and Kopka*, 1977].

The nighttime D-region generally ranges from $50-90$ km in altitude, with the E-region extending from roughly $90-160$ km [*Tascione*, 1994, p90]. Figure 1.2 shows the various regions of the ionosphere and their approximate altitudes.

1.1.3 Auroral Electrojet

The auroral electrojet is an intense horizontally directed current that flows along an oval curve in the high latitude polar region [*Akasofu et al.*, 1965]. Using incoherent backscatter radar, the center of the westward flowing current has been determined to be at an altitude of 100 km, while a smaller eastward current is shown to flow at 120 km altitude [*Kamide and Brekke*, 1993]. Inversion of the IMS Alaska meridian magnetometer chain observatory data shows that the total current in the auroral electrojet can vary from a few thousand amperes to nearly 1.8 million amperes [*Kamide et al.*, 1982]. Figure 1.3 shows the auroral oval.

For the purpose of this thesis, the most important aspect of the auroral electrojet
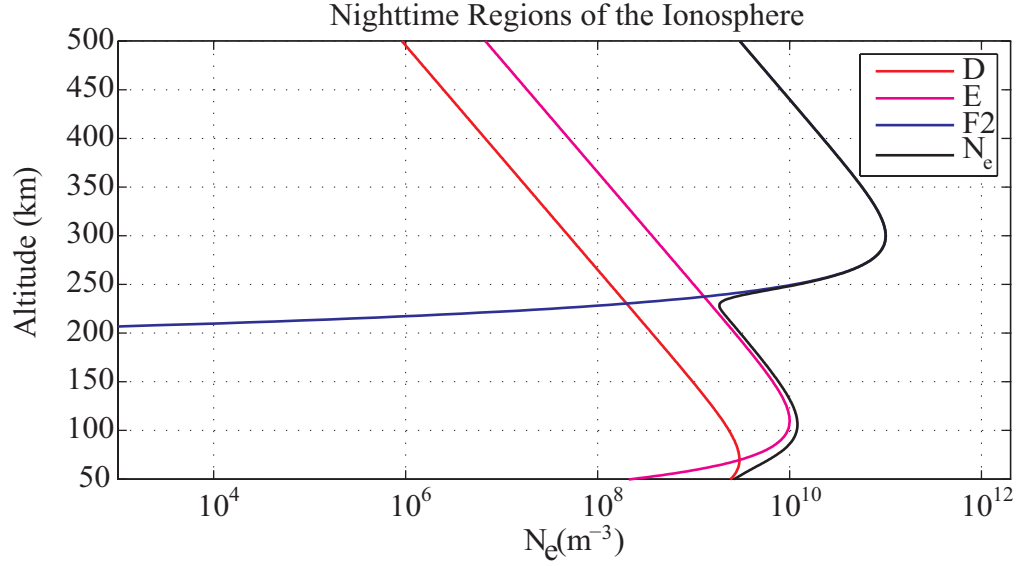
Figure 1.2: Sample ionospheric Chapman layers and approximate altitudes. The F1 layer is absent at night, and the D-region is only weakly ionized. N_e is the total ionization.

are the forces which drive it. The ionized plasma in the E and F-layers of the ionosphere provide a conductive medium for the current to flow. However, it is a large electric field present in this region which imparts the energy necessary to support a large current. The electric field is thought to arise because of the influx of a large amount of current from the magnetosphere which flows down the magnetic field lines [*Casey*, 2005, p48]. The flow of this current through regions of varying conductivity determines the distribution of the electric fields in the auroral region [*Tascione*, 1994, p71]

This electric field present in the E and F-layers is mapped down into the D-region because the ambient parallel conductivity connecting these altitudes is relatively high [*Werner and Ferraro*, 1990]. The ambient Hall and Pedersen conductivities in the D-region are too low to facilitate a large ambient DC current, but the conductivities can be readily modified through changes in electron temperature due to HF heating [*Stubbe and Kopka*, 1977].

The ambient electric field in the D-region is of prime importance in determining the efficiency of HF to VLF conversion. Using an incoherent scatter radar in Chatanika,
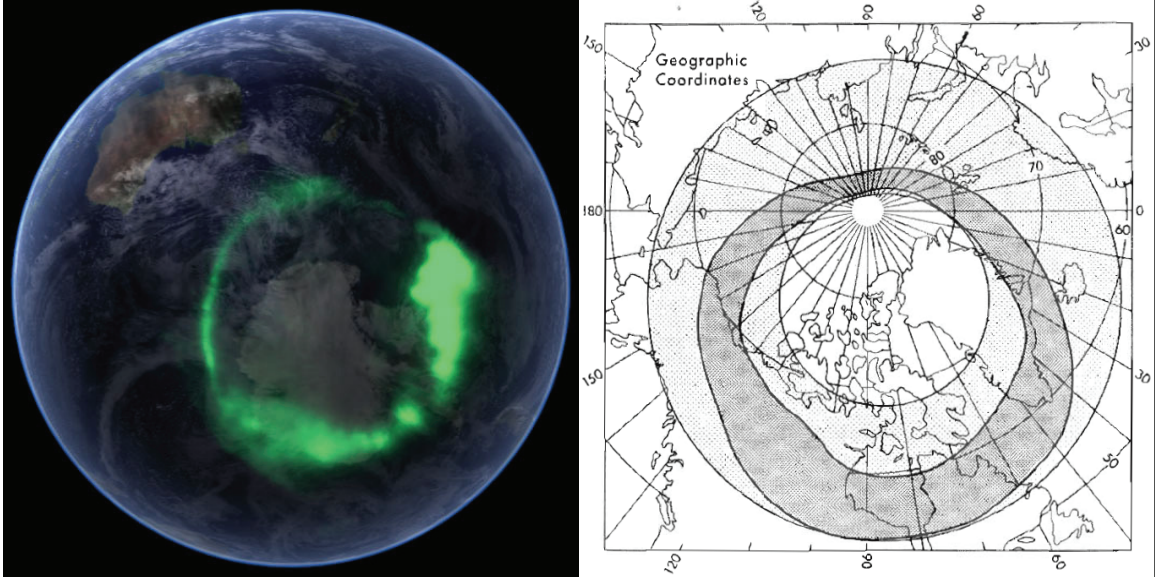
Figure 1.3: The left panel shows a photograph of the auroral electrojet taken with the IMAGE satellite (courtesy NASA). The right panel shows a map of the auroral oval during moderate magnetic storm activity. Dark shading shows the oval at 0800 UTC and the light shading indicates the area swept over the oval during the day [*Knecht*, 1972, p74].

Alaska, *Banks and Doupnik* [1975] were able to track electric field variations in the ionosphere over several days. It was found that the direction and the magnitude of the electric field varies greatly as a function of time. The electric field ranged anywhere from less than 5 mV/m to almost 100 mV/m in absolute strength. Many theoretical works on HF heating base their models on an 'average' electric ambient field strength of 25 mV/m [*Stubbe and Kopka*, 1977].

1.1.4   D-Layer Properties

The D-region of the ionosphere is primarily composed of molecular nitrogen and oxygen, N_2 and O_2. At night, this layer is weakly ionized through energetic electrons precipitating from the radiation belts [*Reid*, 1976], ionizing galactic cosmic rays [*Ratcliffe*, 1972, p19], and ionizing alpha radiation scattered from the exosphere [*Davies*, 1990, p57]. NO^+ and O_2^+ are the two dominant positives ions. Because it is only

weakly ionized, the D-region is not a particularly good reflector of radiation above 100 kHz and remote diagnostic tools available for this region are very limited [*Sechrist*, 1974].

For the purpose of this thesis, the ambient N_2 and O_2 concentrations and the neutral temperatures given by the *MSIS-E-90 Atmosphere Model* are used. This model is supported by the NASA Goddard Space Flight Center and can be accessed using the following URL: (http://modelweb.gsfc.nasa.gov/models/msis.html). The location and time of the Interferometer Campaign is input into the model which produces the concentrations and temperatures shown in the two left panels of Figure 1.4.

The electron density in the nighttime D-region exhibits large variations both during a given night and from night to night. Because HF heating models are very dependent on the electron density profile, three ionospheric profiles are used in this thesis, creatively labeled I, II, and III, which are identical to those used in past Stanford work on VLF heating [*Rodriguez et al.*, 1994] and other D-region modeling studies [*Pasko and Inan*, 1994].

Profile I is based on an exponential profile given in *Wait and Spies* [1964]

$$N_e = 1.43 \times 10^{13} \exp\left[(\beta - 0.15)\, h - \beta h'\right] \tag{1.4}$$

where h is the altitude in km and $\beta = 0.5$ km^{-1} at night [*Wait and Spies*, 1964], and $h' = 85.0$ km [*Inan et al.*, 1990].

Profile II has been used to study energetic particle precipitation effects on VLF wave propagation [*Poulsen*, 1991, p8]. Finally, Profile III is an increase by a factor of 10 over Profile II between 70 and 90 km and represents a disturbed ionosphere due to increased ionization. The right panel of Figure 1.2 shows the three sample profiles.
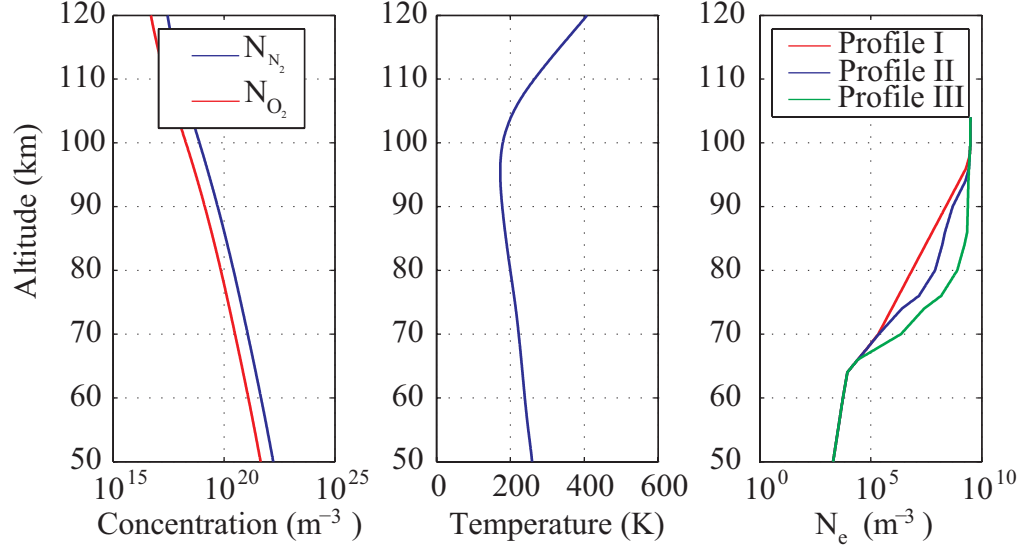
Figure 1.4: Ambient N_2, O_2 concentrations, neutral temperature (T_n), and sample electron density profiles.

1.2 Previous Ionospheric Heater Work

1.2.1 Early Soviet Experiments

The first purposeful experiment designed to observe HF to VLF conversion in the iono-sphere was by *Getmantsev et al.* [1974]. In this experiment, Getmantsev modulated a 5.75 MHz HF radio transmitter at various VLF frequencies around 2 kHz. Using a narrowband receiver, he observed VLF radiation which was roughly proportional to the power of the HF beam. Getmantsev attempted to estimate the current generated by the HF heater in terms of the ionospheric plasma parameters, but stopped short of speculating on any type of current distribution.

Kapustin et al. [1977] used a modulated HF heater to show that the HF to VLF conversion efficiency is strongly correlated with the strength of the auroral electrojet. In this work, Kapustin also shows that proximity of the heated region to the auroral electrojet is very important in determining the conversion efficiency.

Kapustin's work is followed by *Budilin et al.* [1977]. Budilin used modulated HF heating of the ionosphere at a range of frequencies from $1.25 - 7.0$ kHz. By looking

at the slope of the received VLF phase as a function of modulation frequency, a rough estimate of the height of VLF generation was obtained. On various days, the generation height was found to be between $70 - 81$ km, with an average height of 75 km. This early height estimate remains nearly equivalent to the modern estimates made today.

1.2.2 Tromsø Experiments

Between 1977 and 1980, the Tromsø heating facility in Ramfjordmoen, Norway was built by the *Max-Plank-Institut für Aeronomie* in cooperation with the University of Tromsø. This facility consisted of 36 crossed dipole antennas with an output power of 1.2 MW and an Effective Radiated Power (ERP) of 300 MW. After a storm destroyed much of the facility in 1985, the array was rebuilt in 1990 with 144 crossed dipoles and an ERP of 1200 MW. Much of the current understanding of ionospheric modification comes from the use of this facility by many experimenters [*Stubbe*, 1996].

Stubbe et al. [1981] presents the earliest measurements of ELF/VLF generation using the Tromsø heater. During this experiment, the electrojet exhibited "extreme variability" and this variation produced confusing results regarding ELF/VLF wave production as a function of modulation frequency. However, this work also was the first experimental evidence that X-mode HF more efficiently generated ELF/VLF than O-mode HF heating [*Barr*, 1998]

Stubbe et al. [1982] presents a more comprehensive set of data collected from the Tromsø heater. In this set of experiments, the ionosphere is heated by an HF signal that is square-wave modulated at a range of frequencies between $975-4975$ Hz. The generated VLF waves are recorded on both N/S and E/W magnetic loop antennae. It is shown that the polarization of the received magnetic field is usually an ellipse, indicating that the received VLF is the superposition of the right and left hand modes. Rarely does one of the modes dominate to the point where the received signal has circular polarization. *Stubbe et al.* [1982] also show that there is a resonance effect at 2 kHz and harmonics, which is explained as a possible Earth-ionosphere waveguide phenomenon. Additionally, even harmonics of ELF/VLF waves were identified in the

data, which could only be generated by non-linearities in the ionospheric HF to VLF conversion.

Rietveld et al. [1983] conducted a very interesting experiment where the polarization ellipse of generated VLF radiation was compared to the inferred direction of the electric field. Using the STARE auroral radar system, the Doppler shift of radar pulses reflected from electron clusters was measured, which allows the drift rate of particles in the E-region to be inferred. Since electrons drift opposite to the electric field, this measurement yields a reliable estimate of the direction and strength of the ambient electrojet electric field. The polarization ellipse of the N/S to E/W magnetic field is compared to the electric field direction. Depending on ionospheric conditions and the time of day, the received radiation is inferred to be generated either via the Hall or Pedersen conductivities. During the day, the Pedersen conductivity seemed to slightly dominate, while at night, the Hall conductivity dominated. Apparent source heights were estimated by measuring the amplitude ratio of the received ELF/VLF fundamental frequency with the first harmonic using three fundamental frequencies. The average height was found to be roughly 73 km at night, consistent with Budilin's previous experiment [*Budilin et al.*, 1977]. This result was produced by averaging over several hours of data, but for any particular sub-interval the method can produce a large range of estimated source heights [*Rietveld et al.*, 1983, 1987].

James et al. [1984] observed VLF radiation on the ISIS 1 spacecraft originating from ionospheric HF modulation at Tromsø. All five fundamental modulation frequencies and their harmonics were observed, but the amplitude ratio of the harmonics was different from the ratios detected on the ground. This difference was attributed to the different frequency response of the Earth-ionosphere waveguide, as later confirmed by *Barr and Stubbe* [1993]. The observations on ISIS 1 were compared with ray tracing theory and showed qualitative agreement.

Barr et al. [1985] estimated the total radiated power due to ELF modulation of the ionosphere above Tromsø using multiple receivers and waveguide theory. During the experiment, the total estimated ELF output power ranged from 50 μW to 2 W depending on ionospheric conditions. The upper value agrees with previous theory for an ambient electric field of 25 mV/m. Additionally, this observation was the

first long distance measurement of ELF modulation during the Tromsø experiments; signals were detected as far away as 554 km from the heater.

Barr et al. [1986] showed that the first quasi-transverse-electric (QTE) mode is coupled into the Earth-ionosphere waveguide by modulating the ionosphere with an HF heater. This inference was based on the observation of a sharp reduction in radial magnetic field below 2 kHz at a receiver located 554 km from the heating transmitter. Evidence for the excitation of the quasi-transverse-magnetic (QTM0), QTM1, and QTE1 modes are presented. It is also shown that the waveguide cutoff frequency varies temporally, probably due to changes in the ionospheric reflection height. *Barr et al.* [1986] note a sharp decrease in magnetic field strength between 3.5 and 5 kHz that is explained as either waveguide effects, or source current interference. Comparing experimental work to theoretical modeling, it is shown that radiation from a horizontal dipole at the maximum Hall source height proves to be a reasonable match to the experimental data.

Rietveld et al. [1986] deduced the characteristic heating and cooling times of the ionospheric currents using time averaged pulses. The characteristic heating time was found to be about 70 μs while the characteristic cooling time was found to be 120 μs. The apparent source height and reflection height of the ionosphere were deduced by determining the round trip time delay of pulses generated by the HF heater. The reflection height was found to be about 75 km, while the apparent source height was deduced to be 88 km.

James et al. [1990] detected modulated ELF generation on the DE 1 spacecraft while it was 11,000 km away from the Tromsø heater. Unlike previous satellite measurements, the harmonics of the modulation frequencies were not detected. Using the Omega VLF transmitters as a reference, the total VLF power generated was estimated to be about 30 W, at least an order of magnitude greater than previous estimates.

Barr and Stubbe [1991a] reported early results using the repaired and upgraded Tromsø heating facility. Attempting to use the imbalance in heating and cooling times to improve efficiency, this experiment used square-wave modulation with varying duty cycles. It is shown that there is a relative increase in HF to VLF conversion efficiency

with decreased modulation duty cycle. However, the absolute VLF field strength received is found to be maximized when the duty cycle is very close to 50%.

Barr and Stubbe [1991b] concluded that the doubling of gain in the new Tromsø antenna was canceled by the fact that the spot size of the beam shrank by half. The effective ELF generated is shown to be roughly the same as with the old Tromsø configuration [*Barr*, 1998].

1.2.3 Arecibo

Located near the famous Arecibo radio observatory is an array of 4 by 8 log-periodic dipoles. This HF array can operate between $2-12$ MHz with an ERP of $160-320$ MW. It was used in the early 1980s to explore HF modulation of the low-latitude ionosphere [*Barr*, 1998].

Ferraro et al. [1982] shows the first experimental evidence of HF to VLF conversion using the Arecibo HF array. The signals received were of a maximum strength of 1 fT, 3 orders of magnitude below the signals observed at Tromsø. The main difference between Arecibo and Tromsø is the geographic latitude, since otherwise the heaters both have similar output power, gain, and frequency response. This experiment confirms that ambient ionospheric conditions are much more conducive to HF to VLF conversion in the polar latitudes when compared to mid-to-low-latitudes at which there is no electrojet.

Ferraro et al. [1984] show that typical signal amplitudes are in the $10-30$ fT range, rather than the previously reported figures. These values are still far below the average received Tromsø signals. Additionally, it is shown that the polarization ellipse of the received magnetic field correlates to the direction of the modified ionospheric currents as computed using magnetometer data. Finally, this experiment shows that the received VLF amplitude is proportional to the power in the modulated HF beam over the range of $20-200$ kW.

1.2.4   HIPAS Experiments

HIPAS is an array of 8 crossed dipoles oriented in a circle located near Fairbanks, Alaska. Each dipole is capable of radiating 150 kW, for a total of 1.2 MW. Because the array is comparatively small, the total gain from the array phasing is low, which results in a low ERP of 84 MW [*Barr*, 1998].

Ferraro et al. [1989] presents the first evidence of ELF/VLF modulation from the HIPAS array. *McCarrick et al.* [1990] measured the ELF response of the ionosphere and found that there existed very little difference between X-mode and O-mode when modulating at ELF. Only at higher modulation frequencies, in the high ELF through the VLF range, does the ionosphere show a marked increase in efficiency when using an X-mode HF beam. In general, the results obtained from HIPAS modulation were consistent with the previously reported results at Tromsø [*Barr*, 1998].

Bell et al. [1995] shows measurements of the amplitude and phase of electromagnetic waves generated by the NPM transmitter in Hawaii that have propagated beneath a region of ionosphere modulated by the HIPAS heater. It is shown that the majority of the signals recorded exhibit a measurable change in amplitude and phase that tracks the modulation pattern of the HIPAS HF transmissions. It is also shown that these amplitude and phase changes are useful as a diagnostic tool to determine characteristics of the ambient electron density profile above an HF heater.

1.2.5   HAARP Experiments

The High Frequency Active Auroral Research Project (HAARP) is the newest HF heater that is available for ionospheric modification experiments. The Filled Development Prototype (FDP) of the HAARP facility was a 6 by 8 array of crossed dipoles that could generate 960 kW of total output power with an antenna gain of approximately 13.6 dB (depending on HF frequency). The Final Ionospheric Research Instrument (FIRI) version of HAARP has a 15 by 12 array of crossed dipoles and can generate 3.6 MW of output power with an antenna gain of about 20.8 dB.

Milikh et al. [1999] is the first work to report the detection of ELF radiation created by modulation of the HAARP HF beam. This work attempts to model the

formation of the current structure as Horizontal Magnetic Dipoles and compare the model predictions to data, but the presented agreement between data and theory is less than convincing.

Papadopoulos et al. [2003] shows that the maximal efficiency of ground detected HF to ELF/VLF conversion is around 2 kHz. It is also demonstrated that the conversion efficiency decreases rapidly as the HF modulation frequency is decreased in the ELF range, a phenomena explained by the temperature saturation of the electrons in the plasma. Using a 1-D heating code and comparing to ground based near-field measurements, this work estimated the ambient electrojet electric field in the ionosphere to be 30 mV/m.

Bell et al. [2004] reports observations from the Cluster satellite of lower hybrid waves generated from electromagnetic whistler mode waves. The whistler mode waves are created by using the HAARP HF array to modulate the lower ionosphere. Unlike previous measurements which observed this phenomenon at altitudes ≤7000 km, these measurements are made at altitudes ≥20,000 km, outside of the plasmasphere. This work provides strong evidence that whistler mode waves are continuously transformed into lower hybrid waves as the whistler mode propagates beyond $L \sim 4$.

Platino et al. [2004] reports the observation of HAARP modulated VLF signals on several Cluster satellites at distances greater than 10,000 km from HAARP. In addition to the directly coupled waves, lower hybrid waves were detected which may have been generated through linear mode coupling as a result of scattering of the injected ELF/VLF signals by field aligned irregularities.

Inan et al. [2004] describes an experiment to measure the generated VLF waves near HAARP as well as at the magnetic conjugate point in the southern hemisphere. Magnetospherically injected VLF radiation and triggered emissions were successfully measured at the conjugate point. Simultaneously, many reflections of this signal were detected near HAARP, indicating that the generated and magnetospherically amplified signals were bouncing between the ionosphere above HAARP and the magnetic conjugate point. This experiment showed that a facility like HAARP may be used to study magnetospheric wave particle interactions by carrying out controlled ELF/VLF wave-injections experiments.

Papadopoulos et al. [2005] shows the magnetic response of the ionosphere to various length HF pulses generated by HAARP. The pulse response is attributed to the time derivate of the current, $\partial\mathbf{J}/\partial t$, and a model Green's function is presented to describe the resulting radiation.

Platino et al. [2006] shows the detection of HAARP modulated ELF/VLF signals on the low altitude DEMETER spacecraft. The ELF/VLF power generated by the heated region of the ionosphere was estimated as $0.32-4$ W based on data from DEMETER, and between $2.71-4.22$ W based on simultaneous data from ground based measurements. This observation is the most consistent measurement of ionospheric generated ELF/VLF power between spacecraft and ground based sites.

Moore et al. [2006] presents evidence of power saturation in the generation of VLF radiation using the HAARP heater. An empirical saturation function is derived that shows how the first, second, and third harmonics of the modulation frequency behave at various power levels. This analysis is important because previous studies generally assume that VLF amplitude is proportional to HF beam power. If saturation effects occur, higher HF power levels might not provide as much increase in VLF production, thus leading to reduced efficiency of the HF to VLF conversion.

1.3 Overview of ELF/VLF Modulation Theory

In this section, a quick overview of the theory of HF to ELF/VLF conversion is presented. The details are neglected herein and are instead treated in detail in later chapters that explicitly discuss modeling.

While there are earlier works that discuss modification of electron temperature in the lower ionosphere, the first paper to comprehensively assemble a picture describing ionospheric modulation is *Stubbe and Kopka* [1977]. The paper provides early insight into how to approach HF radiation interaction with D-region electrons. Rotational and vibrational N_2 and O_2 loss terms are taken into consideration, as is the relationship between electron temperature and the Hall and Pedersen conductivities. It is recognized that small polarization fields arise due to gradients in the various conductivities and these are analytically calculated based on simplifying assumptions.

Finally, radiation on the ground is computed by modeling the heated currents as free space antenna elements.

Stubbe and Kopka [1977] provided a firm conceptual framework for future theoreticians to follow. However, there were numerous assumptions made which make this work unsuitable for modeling HAARP-related phenomena. Firstly, it is assumed that temperature variations are small compared to the average ambient temperature, an assumption that is not true in the case of large ionospheric heaters such as Tromsø, HIPAS, or HAARP. The temperature is also assumed to vary sinusoidally for a square-wave modulated HF signal, which ignores both the harmonics contained in the square-wave itself, and the harmonics generated due to non-linearities in the absorption process. A non-kinetic relationship between the temperature and the Hall and Pedersen conductivity was used, and the parallel conductivity was ignored altogether. Finally, a free space propagation model is used which ignores the complex behavior of the Earth-ionosphere waveguide, especially when the sources are within the waveguide medium [*Barr*, 1998].

Tomko et al. [1980] greatly improves upon the theory of the interaction between HF radiation and electron temperature. This work models the temporal variation of electron temperature as a function of height due to various HF pulses. The asymmetry in the heating and cooling times is predicted, as is the large effect of self-absorption. The electron temperature profiles are used to accurately predict the attenuation of diagnostic waves reflected from the lower ionosphere.

Tomko [1981] improves upon the theory relating electron temperature to conductivity values by incorporating kinetic terms, accounting for the fact that the collision rates are themselves temperature dependent. The full derivation involves integrating the temperature dependent loss rates over electron energy using an assumed Maxwell-Boltzmann electron distribution function.

Ferraro et al. [1982] uses a non-kinetic derivation connecting electron temperature to conductivity due to HF heating above Arecibo. The resulting Hall and Pedersen conductivity changes are multiplied by an assumed ambient electric field. The volume space intersected by the heated region and the HF beam is decomposed into ELF/VLF source current sheets. ELF/VLF produced by each of these current sheets is radiated

to the ground using a free space propagation method.

Stubbe et al. [1982] offers an intuitive circuit diagram to model the path of current flow during conductivity modulation. In this simple model, some of the current flows through the directly modulated region, some flows around the modulated region due to the perturbing electric field, and the last bit of current flows up the magnetic field lines and reconnects at a greater altitude in the ionosphere. Using approximated impedances, it is shown that at ELF and VLF frequencies, the predominant current to consider is the current which flows directly through the modulated region.

Barr and Stubbe [1984] is the first paper related to ionospheric heating that tackles the Earth-ionosphere waveguide excitation problem. Although it was recognized in *Stubbe et al.* [1982] that the receivers detected strong evidence of waveguide effects, the complications involved in determining how currents couple into the waveguide were ignored due to the complexity of the problem. *Barr and Stubbe* [1984] uses reciprocity theory to compare the efficiency of excitation of the Earth-ionosphere waveguide with an arbitrarily excited dipole in the ionosphere versus a vertical ground-based dipole. This comparison is done as a function of height, using the first few excited waveguide modes. By computing the modulation depth of the Hall and Pedersen conductivities, an approximation for the current as a function of height is obtained. The resulting current dipoles are transformed to ground based dipoles through the use of the reciprocity efficiency calculation. These ground based dipoles then excite various modes in the Earth-ionosphere waveguide which are compared to actual data.

An interesting result from *Barr and Stubbe* [1984] is that while the Pedersen and Hall conductivities are modulated similarly, the fact that the Pedersen conductivity has its maximum modulation depth several kilometers higher in altitude has a drastic effect on its ability to couple ELF/VLF radiation into the waveguide. This effect could be used to explain why the Hall conductivity modulation seem to dominate ground based observations in a number of different experiments.

Papadopoulos et al. [1990] uses a kinetic derivation to model the Hall and Pedersen conductivities during ELF modulation. Detailed temporal plots of the electron temperature, the Hall conductivity, and the Pedersen conductivity are shown. Additionally, the sensitivity of the conductivities as a function of power is determined to

indicate regimes where increased conversion efficiencies are possible.

Zhou et al. [1996] takes a very mathematical approach to the determination of current flow due to the primary conductivity modulation. In this work, it is shown that a consequence of heating in the ELF range is currents that run along the magnetic field lines. If enough time is present for charge to accumulate at the lateral edge of the heated region due to the primary conduction currents, a perturbing electric field results. This perturbing electric field tends to push current down the magnetic field lines because the ambient parallel conductivity is two orders of magnitude greater than the ambient Hall or Pedersen conductivities.

1.4 Experimental and Theoretical Summary

From the numerous experimental and theoretical works discussed above, it is possible to draw a number of conclusions. Firstly, the theory that explains the interaction of the HF beam with electrons that leads to electron temperature changes is well developed. Given an accurate ambient ionospheric profile, it is possible to reliably and accurately model the electron temperature modifications, so long as the heating does not continue long enough for the electron concentrations to be modified through thermal diffusion and/or ionospheric chemistry. With the length scales involved, it is unlikely for thermal diffusion to have much of an effect unless heating continues for several minutes. Such effects are certainly negligible in the case of ELF/VLF modulation, with cycle times of at most tens of milliseconds.

The theoretical work that connects electron temperature to conductivity parameters is equally well developed. Once the electron temperatures have been deduced, it is a straightforward process to determine how the direct currents are modulated.

What is not as well developed is the structure of the secondary currents that inevitably arise because the direct modulated currents cause perturbing fields in the ionospheric plasma. Theoretical work seems to indicate that secondary conduction currents play a large role at ULF and at the low end of the ELF range. Additionally, theoretical considerations indicate that it is not likely for modulated heating at mid-VLF frequencies to give rise to significant secondary currents [*Stubbe et al.*, 1982].

However, it is not entirely clear what role such secondary currents may play at the transition frequencies between ELF and VLF.

Experiments have indicated that the Earth-ionosphere waveguide may play a large role in determining the intensity of VLF fields observed at line of site receivers. However, the theory that connects ionospheric currents to arbitrary ground based measurements is sorely lacking, largely because the system is hugely complicated and simplifying approximations are not possible. Theory does seem to agree that the ability of a current to couple radiation into the Earth-ionosphere waveguide is very sensitive to its altitude and orientation.

Finally, experiments have shown that Hall currents seem statistically to be the dominant contributor to the ELF/VLF radiation generated via HF modification of the D-region at night. However, individual measurements can either be more Hall-like, or more Pedersen-like depending upon ionospheric conditions. Without independently collected electric field measurements, it has proved difficult to determine the ratio of the relative contributions of the Hall to Pedersen currents using any single ground-based measurement.

1.5 Contributions of this Work

During the tenure of the author in the VLF group at Stanford University, three separate remote sensing instruments were developed, and two of them were personally deployed[1]. For this dissertation, the only hardware discussed relates to the first instrument, the so called ELF/VLF Interferometer Unit. The remainder of the thesis deals with the use of computer models and the data collected during the Interferometer Campaign to estimate the spatial currents above a modulated HF heater.

The contributions included in this dissertation, broken down by chapter are as follows:

Chapter 2: A new instrument design for VLF remote sensing is presented, described,

---

[1]Interferometer Unit, Automated Geophysical Observatory (AGO) broadband receiver for Antarctica, and a broadband receiver for the WIPER satellite experiment.

and characterized. The Interferometer Unit is the first portable battery powered instrument that combines precise time synchronization, low-power, and the ability to survive the hostile Alaskan winter. Nine of these units were built and deployed for the Stanford HAARP Interferometer Campaign which utilized the largest number of time synchronized sites for simultaneous measurements of HF to VLF conversion on record.

Chapter 3: Using a conic quadratic solver, a method to invert highly singular matrices formed by relating electromagnetic observations to source currents is presented. While this method fails to solve the inversion problem due to extreme sensitivities to systematic measurement errors, the technique is a significant improvement over standard inversion techniques and may prove useful in other ill-posed problems.

Chapter 4: Existing methods for modeling ionospheric conductivity changes due to HF heating of the lower ionosphere are optimized in C++ to permit the production of detailed 3-D conductivity maps. These 3-D maps are input into a full wave electromagnetic plasma interaction FDTD code to determine the response of the plasma to the conductivity change in the presence of an ambient electrojet field. The spatial current distribution during HF modulation is estimated using the output of the HF heating model and the FDTD code.

Chapter 5: The data collected during the Interferometer Campaign is compared and shown to be consistent with the predicted current structure given in Chapter 4. A new method for determining the net dipole current moment of the VLF radiation source is presented. This orientation method is used to align the ground radiation predictions from the models to the data recorded at the Interferometer sites.

Chapter 2

Instrumentation and Experiment

One of the unique challenges of the Interferometer project was to collect calibrated, time coherent data from portable battery powered devices spread throughout the Alaskan wilderness. While it is nearly always the case that off the shelf equipment is more cost effective and less risky than custom built hardware, at the time of the Interferometer Campaign no solution existed that could meet the performance requirements. With an adventurous heart, these problems were overcome by custom designing and building a data recording network at Stanford.

This chapter is divided into two parts. The first part is an explanation of the Interferometer Unit and its various capabilities. The second part is a description of the Interferometer Campaign, which utilized nine of the Interferometer Units.

2.1 Instrumentation

The purpose of this section is to describe the design and capabilities of the custom built Interferometer Unit. The section begins with an examination of the device requirements and then explains the various parts of the Interferometer and the basic characteristics of each circuit. Finally, the methods used to calibrate the magnetic and electric channels are discussed
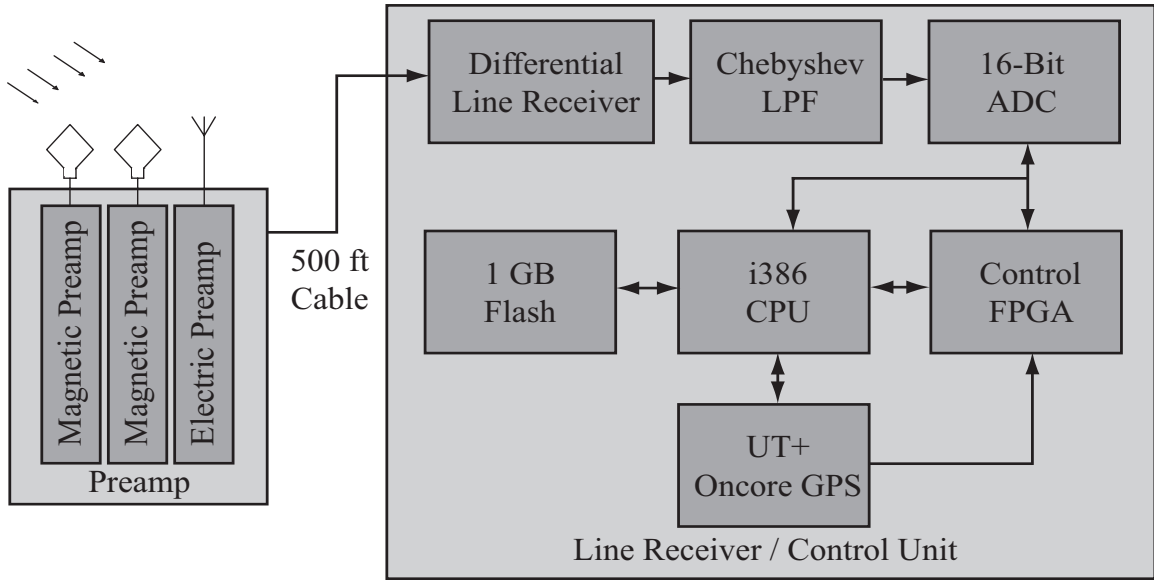
Figure 2.1: Functional block diagram of the Interferometer Unit.

2.1.1 Requirements and Block Diagram

The device requirements for the Interferometer were put forth in the program proposal and then revised throughout the development of the project. The basic requirements were as follows:

1. Maximum continuous power utilization of 1 W

2. 10 ksps sample rate

3. Three independent channels that are sampled simultaneously

4. Survive and operate in -40° C temperatures

5. Record at least two days of data before a download is required

6. Timing drift from UTC less than 1 μs

7. System sensitivity sufficient to measure ELF/VLF signals of approximately 1 s duration with intensities as low as 0.01 pT

The basic design consists of three separate units: an antenna cluster, a preamplifier assembly, and a data recording unit (see Figure 2.1). The preamplifier is mounted directly on the antenna cluster to minimize signal degradation and noise pick-up. The preamplifier sends data over a 500 ft cable to the data recording unit which is in an enclosed wooden box. This separation is necessary to prevent digital switching noise from being collected by the antennae. Batteries are stationed near the data recording unit, which regulates the power both for itself and for the preamplifier assembly.

All of the requirements except the power were met. Despite a great deal of effort, the power dissipated could not be brought down to 1 W; the actual power dissipated eventually increased to roughly 3.0 W, with most consumption due to the CPU needed to control the various aspects of the device. The extra power consumption was compensated by running the entire system off three gel-cell batteries with 40 A-H of charge.

In the next few sections, each part of the Interferometer Unit is discussed in more depth. A complete overview of every circuit is unnecessary for this thesis; however, where important and relevant, individual pieces of the circuitry are described.

2.1.2   Antennas

Loop Antenna

It is sometimes easy to underestimate the difficulty in collecting high fidelity femtotesla strength VLF signals from the ionosphere. Because the signals are so tiny, it is imperative that a large antenna be used to maximize the power of the collected signal and enhance the resultant Signal to Noise Ratio (SNR). It is equally important that the impedance of the antenna properly matches the input of the preamplifier; otherwise, large amounts of the collected signal are wasted as mismatch losses.

For an air-core loop antenna, there are four basic design parameters: loop shape, loop area (A), wire diameter (d), and the number of loop turns (N).

The loop shape of the Interferometer antenna is that of a square. While the maximum collection area for a set length of wire is a circle, a large circular antenna

is exceedingly difficult to erect in practice. A square loop offers a reasonable com-
promised between maximizing collection area for a set length of wire and ease of
deployment. Because VLF loop antennas are very small compared to the wavelength
of the measured radiation, the radiation resistance of the antenna is negligible com-
pared to the ohmic resistance of the wire [*Watt*, 1967].

The DC resistance of the antenna is

$$R_{\mathrm{a}} = \frac{16\rho N \sqrt{A}}{\pi d^2} \ \Omega \tag{2.1}$$

where ρ is the resistivity of the wire, N is the number of loops, A is the area of the
square loop, and d is the diameter of the wire [*Paschal*, 1988, p30].

The inductance of the antenna is [*Paschal*, 1988, p31]

$$L_{\mathrm{a}} = 8 \times 10^{-7} N^2 \sqrt{A} \left[\ln \left(\frac{4\sqrt{A}}{\sqrt{N}d} \right) - 1.217 \right] \ \mathrm{mH} \tag{2.2}$$

Calculating d, N, and A is an iterative process that is described in [*Paschal*,
1988, p35-37]. The target impedance chosen for the loop antenna is 1 Ω, 1 mH and
is realized by using a 4.9 m per side square loop antenna with 16 AWG wire and 6
complete turns.

Whip Antenna

The requirements of the electric antenna design are more about physical resilience
than about electrical specifications. At VLF frequencies, a small monopole electric
field antenna has a very large impedance as viewed from the terminals. Using a short
monopole model, the input impedance can be modeled as

$$Z_{\mathrm{a}} = [(R_{\mathrm{r}} + R_{\mathrm{ohmic}}) + iX_{\mathrm{a}}] \ \Omega \tag{2.3}$$

where Z_{a} is the total input impedance, R_{r} is the radiation resistance, R_{ohmic} is the
ohmic losses, and X_{a} is the reactance [*Stutzman and Thiele*, 1998, p43-44].

The surface resistance of the antenna is computed as

$$R_{\mathrm{s}} = \sqrt{\frac{\pi f \mu}{\sigma}}\ \Omega \tag{2.4}$$

where μ is the permeability of the antenna material, f is the frequency of operation, and σ is the conductivity of the antenna material [*Stutzman and Thiele*, 1998, p45].

The radiation resistance is determined from

$$R_{\mathrm{r}} = 40\pi^2 \left(\frac{h}{\lambda}\right)^2 \Omega \tag{2.5}$$

where h is the length of the monopole and λ is the wavelength of the radiation [*Stutzman and Thiele*, 1998, p66].

The ohmic resistance of the antenna is found from

$$R_{\mathrm{ohmic}} = \frac{h}{\pi a}\frac{R_{\mathrm{s}}}{6}\ \Omega \tag{2.6}$$

where R_{s} is the previously computed surface resistance [*Stutzman and Thiele*, 1998, p46, p66].

Finally, the reactance of the antenna is computed as

$$X_{\mathrm{a}} = -\frac{30\lambda}{\pi h}\left[\ln\left(\frac{h}{a}\right) - 1\right]\ \Omega \tag{2.7}$$

where a is the radius of the antenna wire [*Stutzman and Thiele*, 1998, p46].

The antenna chosen was a military grade 4.9 m whip antenna, the AT-1011/U. Using approximate values, the estimated parameters of the antenna are summarized

below:

$$h = 4.9 \text{ m} \tag{2.8}$$

$$\lambda = 150 \text{ km} \tag{2.9}$$

$$a = 1 \text{ cm} \tag{2.10}$$

$$\sigma = 1.724 \times 10^{-8} \text{ } \Omega \cdot \text{m} \tag{2.11}$$

$$R_{\text{r}} = 4.21 \times 10^{-7} \text{ } \Omega \tag{2.12}$$

$$R_{\text{ohmic}} = 0.003 \text{ } \Omega \tag{2.13}$$

$$X_{\text{a}} = -1.51 \text{ M}\Omega \tag{2.14}$$

These numbers show that the antenna is almost entirely capacitive, justifying the use of a simple high impedance input on the electric field preamplifier.

2.1.3 Preamplifiers

Magnetic Preamplifier

The signal sensed by the loop antenna must be amplified before being passed to the line receiver. The line receiver is separated from the antenna to isolate the digital electronics from the sensor and to prevent self injected noise from entering the system. The purpose of the magnetic preamplifier is to match the impedance of the antenna, amplify the tiny current signal, and drive a large capacitive cable to the line receiver. It must do this with 100 dB of linear dynamic range. See Appendix A for a schematic of the magnetic preamplifier. This particular preamplifier was originally designed by Dave Shafer [*Shafer*, 1992]. In this section, a cursory overview of the circuit is presented.

The first stage of the preamplifier, shown in Figure 2.2, consists of a transformer matching circuit. T1 converts the input impedance of the amplifier stage to match the 1 Ω, 1 mH impedance of the loop antenna. When current flows through the primary of T1, it excites a voltage across the secondary which is connected to the emitters of the matched differential pair Q3. The output of Q3 is a differential signal
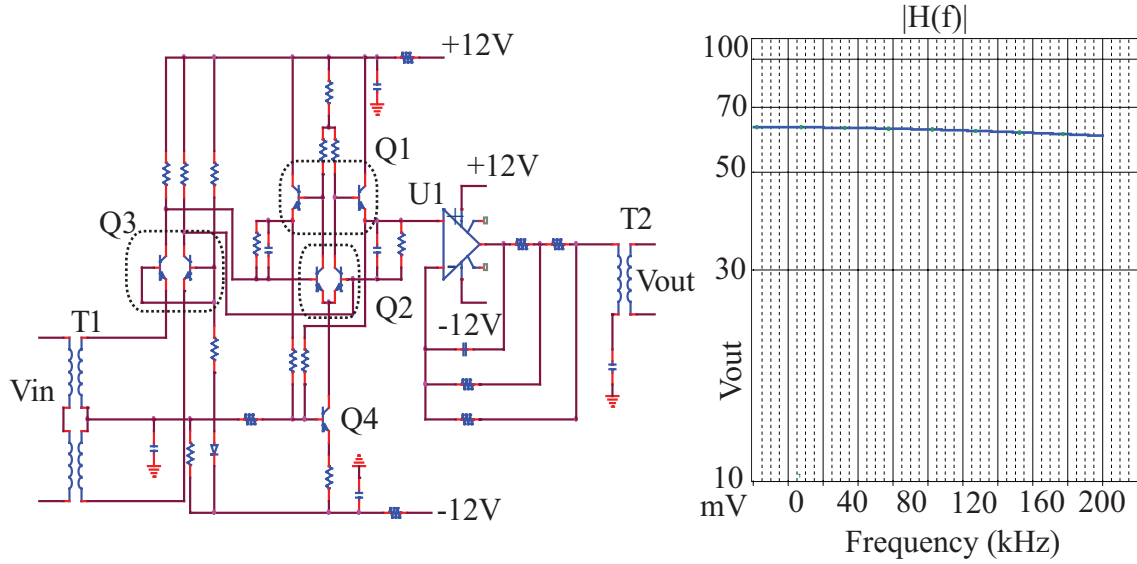
Figure 2.2: Magnetic field preamplifier circuit and the associated transfer function. The input signal is a 1 V amplitude sinusoid to the primary coil of transformer T1. Notice the flat response over the frequency band of interest. The values of components are not shown to conserve space, but are given in Appendix A.

at the collectors of the transistor pair. This output is fed into the base of a second differential pair, Q2. The collectors of Q2 are fed into the bases of a third differential pair, Q1. Q1 and Q2 are jointly biased by Q4, which is configured to change the bias point based on the common mode of the input signal. This configuration keeps the amplifier from railing upon the addition of small common mode signals. Finally, the output of Q1 is taken as a single-ended signal into a high input impedance non-inverting operational amplifier. This amplifier drives a second transformer which acts to match the output impedance of the cable to the output impedance of the circuit (75 Ω).

Electric Preamplifier

Like the magnetic field signal, the electric field signal must be amplified before it is passed to the line receiver. Fortunately, the high impedance of the monopole antenna means that an amplifier designed around simple op-amp circuits can be used
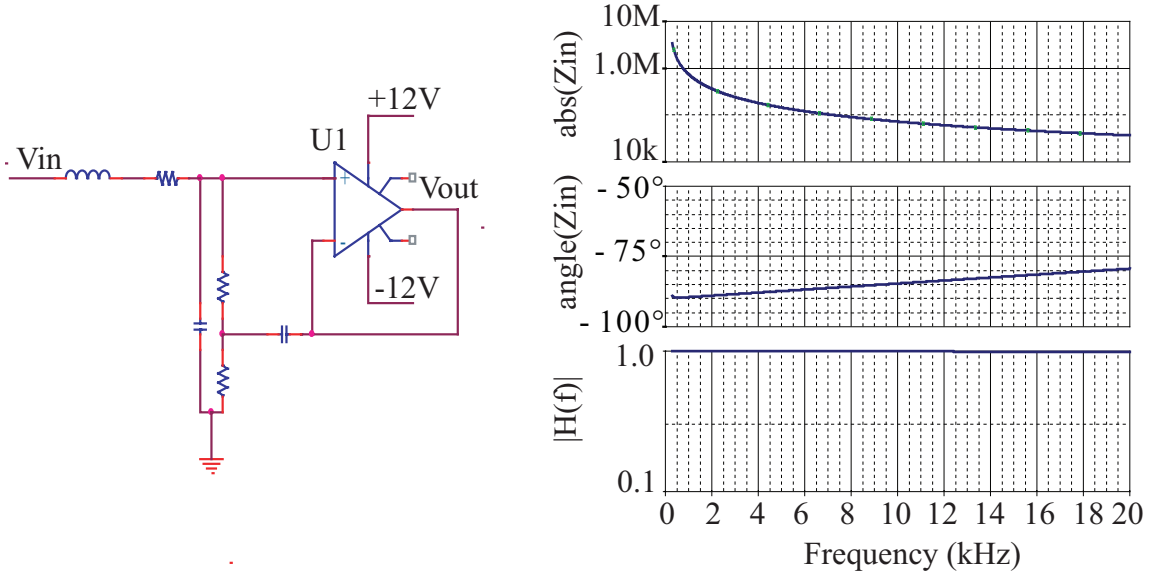
Figure 2.3: The matching input stage of the electric preamplifier is shown on the left. On the right, the input impedance as a function of frequency is shown in the top two plots, while the transfer function is shown in the bottom plot.

as a simple input stage. The left panel of Figure 2.3 shows the basic input stage used for the electric preamplifier. The first op-amp stage, U1, is designed to have a reasonably flat frequency response from DC to 10 kHz, while also having a rather high real impedance and a highly capacitive imaginary impedance. The frequency response and input impedance of the circuit are shown in the right panel of Figure 2.3.

The second stage of the preamplifier is designed to eliminate the VLF signals from LORAN-C navigational transmitters that operate between $90-110$ kHz. There are five LORAN-C transmitters located in the state of Alaska. Notches are placed in the transfer function of the second stage of the amplifier at 88.5 kHz and 108 kHz to suppress the LORAN-C signals and prevent the line receiver from clipping. The second stage schematic and transfer function are shown in Figure 2.4.

The third stage of the preamplifier has a gain of 100, and is a negative inverting amplifier built around op-amp U3. Op-amp U3 feeds the output op-amp which drives the output transformer. This output transformer is directly coupled to the 75 Ω
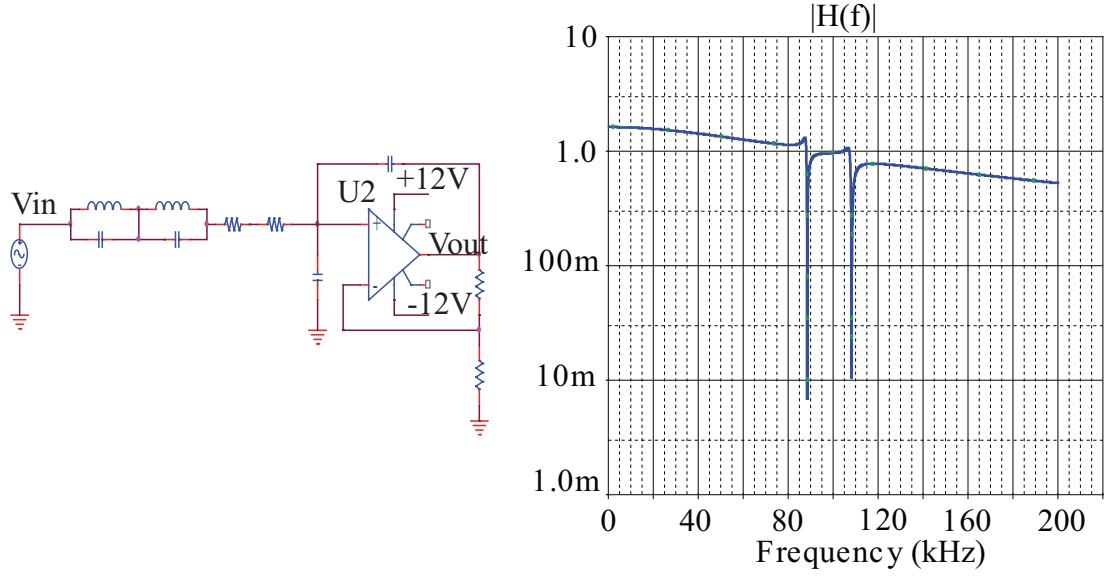
Figure 2.4: The second stage of the electric preamplifer is shown on the left, while the transfer function is shown on the right. Notice the notches in the transfer function where competing VLF signals are removed.

impedance cable which runs to the line receiver.

2.1.4   Line Receiver

The three line receiver circuits are of identical design, regardless of whether the circuit is connected to the magnetic or electric preamplifier. A basic three op-amp instrumentation amplifier is used because of its high common mode rejection ratio (CMRR), along with its high differential gain and tolerance of small resistor mismatch [*Horowitz and Hill*, 1989]. The Analog OP400 low power op-amp is used as the building block for the instrumentation amplifier.

Unfortunately, a resistor was inadvertently misplaced during schematic translation. As a result, what should have been a transfer function of

$$V_{\text{out}} = V_+ - V_- \tag{2.15}$$

was actually implemented as

$$V_{\text{out}} = 2V_+ - V_- \qquad (2.16)$$

This mistake eliminated the good CMRR that was expected of the device, allowing a good deal of 60 Hz noise to leak into Interferometer sites that were located in relatively close proximity to power transmission lines. Fortunately, ELF/VLF signals generated by the HAARP ionospheric heater were strong enough to be nevertheless detectable at all Interferometer sites.

2.1.5   Anti-Aliasing Filter

The largest frequency that is intentionally sampled in the Interferometer campaign is 2.5 kHz. To allow some margin for the filter response relative to the received signals, the sampling rate is set at 10 kHz. The Nyquist Sampling Theorem dictates that any signal above 7.5 kHz will interfere with our primary signal band (0−2.5 kHz).

For the Interferometer experiment, a reasonably linear phase response and a large attenuation per pole is required. For these two reasons, a Chebyshev filter was selected and implemented using standard Sallen-Key filter blocks. In a Chebyshev filter, some passband ripple is tolerated in exchange for greater attenuation in the stop band. Because the frequency response of the Interferometer is well calibrated, this passband ripple is acceptable. Despite using a Chebyshev filter and accepting passband ripple, only 60 dB of attenuation could be obtained at the critical 7.5 kHz alias frequency, thus compromising the 16-bit dynamic range (96 dB) available in the analog to digital converters. Fortunately, the received VLF signal strength was both high and narrowband, preventing this filter handicap from greatly affecting the results. Figure 2.5 shows the transfer function of the anti-alias filter used in each Interferometer Unit.

2.1.6   Sampling Card

The major obstacle in this experiment is in providing precise timing to each of the remote stations. The experiment requirements specify a maximum timing offset from
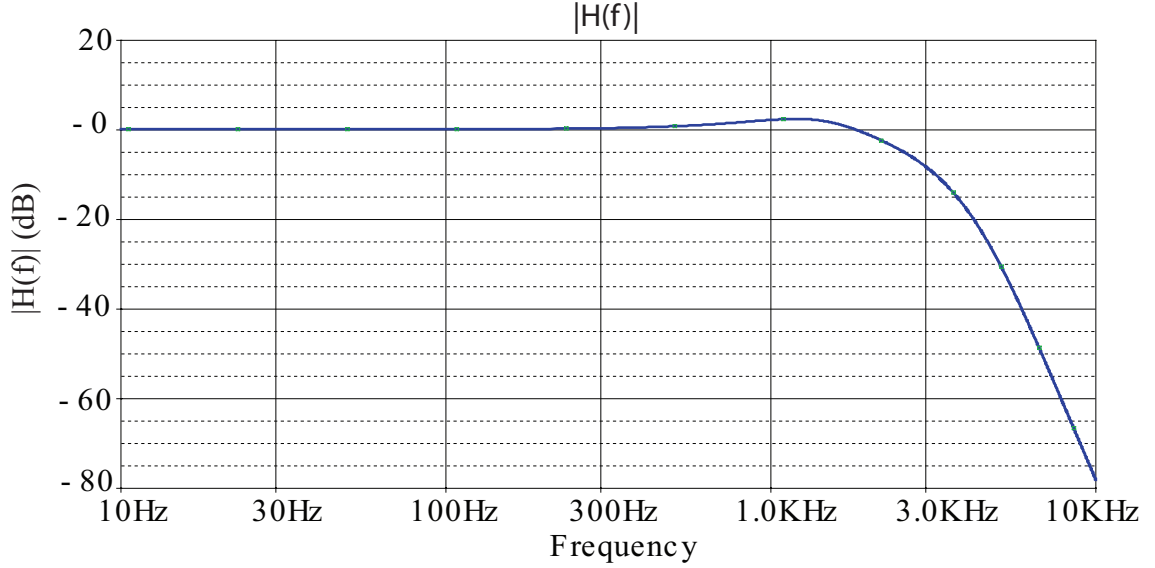
Figure 2.5: Transfer function of 8-pole Chebyshev filter used in the Interferometer Unit.

GPS time of 1 μs. This goal was met for the entire array. Initial timing information for every interferometer unit is received from a Motorola Oncore GPS unit. Once four GPS satellites are acquired, each GPS unit is synchronized to within 100 ns of UTC. The output from the GPS card is a 1 pulse per second (PPS) signal that is sent to the control Field Programmable Gate Array (FPGA) on the sample board.

The control FPGA is the heart of the timing system of each Interferometer. Along with the 1 PPS GPS signal, the FPGA is fed a very stable timing signal from a 10 MHz oven controlled oscillator (OCX) manufactured by Vectron International. The absolute accuracy of the local oscillator is guaranteed to 0.5 parts per million (ppm). The FPGA counts the 10 MHz OCX down to a 10 kHz internal signal. To keep the 10 kHz signal linked to absolute GPS timing, the FPGA counter is designed to reset at each GPS output 1 PPS pulse. This reset prevents large accumulation errors from destroying the coherency of the system. Adding all sources of errors, the worst drift from absolute time during the 1 s period between GPS pulses is approximately 700 ns for each site. In the worst case when another site has all possible errors in the other direction, a total mismatch of 1.4 μs is thus the maximum difference between
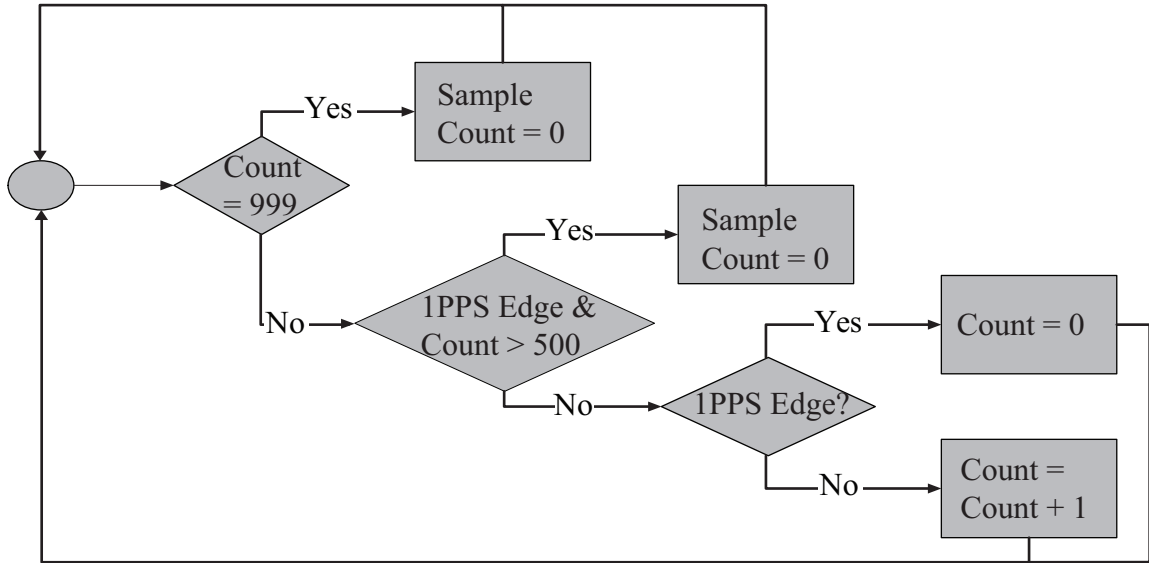
Figure 2.6: Flow chart illustrating method of ensuring time synchronization.

sites. See Figure 2.6.

The sample signal is output to three independent ADC chips. Each of these is an LTC1606 16-bit, 250 ksps converter, with input range of ± 10 V. This chip runs from a single 5 V supply and dissipates only 75 mW of power during operation. It is also rated to function at temperatures down to -40° C.

2.1.7   Compact Flash Storage

CompactFlash cards have been popular in camera and hand held electronic devices for a few years. The standard is well codified and the devices are small, robust, and require very little power. For these reasons, CompactFlash cards are used as the storage medium for each Interferometer unit.

The CompactFlash card shares the 16-bit data bus on the digital microcontroller board. A section of memory is mapped to the card for easy device management. Drivers for the CompactFlash allow basic I/O functions at a high level; these drivers were custom designed in C. Detailed information on the CompactFlash standard can be found at (http://www.compactflash.org/).

2.1.8 Software

The entire digital architecture is built around a single board computer (SBC), the Tern i386 Card. This SBC has a built in memory unit, local oscillator, low power i386 microcontroller, and a development environment that allows easy programming and debugging in C and C++.

The program that runs on the i386 contains a main loop that compares current date and time with a stored list of record times. When the SBC determines that it is time to start sampling, a flag is sent to the FPGA on the sample board for it to begin recording; the sample board begins to record on the next 1 PPS GPS pulse. The data is read from each ADC in sequence and temporarily stored to RAM on the SBC. Between ADC reads, the SBC sends data to the CompactFlash card. Once the required amount of data has been collected, the SBC signals the FPGA to stop sampling through the use of the flag.

2.1.9 Calibration

One of the least glamorous, but most important tasks regarding any new instrument is its proper calibration. In this section, the calibration method used on each device is briefly described. For actual calibration results, see Appendix B. For a more in-depth discussion regarding calibrating loop antennas, see *Paschal* [1988].

Magnetic Field

Figure 2.7 shows the basic circuit used to calibrate the magnetic field channels of the Interferometer Unit. V_{cal} is the voltage injected into the calibration circuit, R_{cal} and C_{cal} are the resistance and capacitance of the calibration circuit, R_a, L_a, and V_a are the resistance, inductance, and voltage of the simulated loop antenna, and Z_p is the impedance of the primary loop of the transformer.

The basic idea is to relate the signal across the antenna terminals (V_a) to the signal being injected into the calibration circuit (V_{cal}). Using antenna theory, the magnetic field is then related to the voltage across the antenna. Assuming that the impedance of the transformer is much larger than R_{cal} and R_a, the following approximation is

valid

$$I_{\text{cal}} \simeq \frac{V_{\text{cal}}}{R_{\text{cal}} \left(1 + \dfrac{f_{\text{cal}}}{if}\right)} \tag{2.17}$$

where $f_{\text{cal}} = (2\pi C_{\text{cal}} R_{\text{cal}})^{-1}$.

The input current to the primary coil of the transformer is $I_1 - I_2$. After a bit of algebraic manipulation we find:

$$I_{\text{in}} \simeq \frac{V_{\text{cal}} \left(1 + f_{\text{a}}/if\right)}{R_{\text{cal}} \left(1 + f_{\text{cal}}/if\right)} \frac{i2\pi f L_{\text{a}}}{R_{\text{cal}} \left(Z_{\text{p}} + R_{\text{a}} + i2\pi f L_{\text{a}}\right)} = \frac{2V_{\text{a}}}{Z_{\text{p}} + R_{\text{a}} + i2\pi f L_{\text{a}}} \tag{2.18}$$

where $f_{\text{a}} = R_{\text{a}} \left(2\pi L_{\text{a}}\right)^{-1}$.

By relating the voltage across the loop antenna to the magnetic field strength, the magnetic field amplitude can be related to the calibration voltage

$$V_{\text{a}} = i2\pi f N A B_{\omega} \tag{2.19}$$

$$B_{\omega} = \frac{L_{\text{a}}}{2NAR_{\text{cal}}} \left(\frac{1 + f_{\text{a}}/if}{1 + f_{\text{cal}}/if}\right) V_{\text{cal}} \tag{2.20}$$

where N is the number of loops and A is the area of the antenna. To simplify the equations and make the calibration frequency independent, f_{cal} is set equal to f_{a} in which case Equation 2.20 simplifies to

$$B_{\omega} = \frac{L_{\text{a}}}{2NAR_{\text{cal}}} V_{\text{a}} \tag{2.21}$$

Each receiver and associated magnetic preamp is hooked to the calibration circuit. A precision signal generator is then connected to the input of the calibration circuit, and the response of the entire receiver is measured just before the ADC at both 1875 Hz and 2500 Hz. In this way, each receiver is fully characterized at the primary ELF/VLF tone frequencies transmitted during the Interferometer Campaign.

Electric Field

The calibration of the electric field channel is made difficult by the complicated relationship between the antenna voltage and the intensity of the electric field. For rigidity, the structure supporting the electric field antenna is constructed from aluminum tubing. This aluminum tubing distorts the electric field pattern near the Interferometer and makes it difficult to use simple antenna theory to relate the antenna voltage to the vertical electric field strength. A proper analysis would require a full finite element calculation to numerically derive the antenna pattern and impedance. Because this is a highly involved time consuming process, the electric fields are estimated using a much simplier method.

To approximately calibrate the electric field strength, recordings of natural signals such as radio atmospherics (produced by lightning) are examined on all three channels. Long distance lightning discharges couple into the Earth-ionosphere waveguide primarily in the TM_0 mode [*Wait*, 1957]. This implies that

$$E \simeq cB \qquad (2.22)$$

By averaging over a number of spherics using actual data obtained at each location, an approximate calibration for the electric field channel can be deduced by comparing the recorded magnetic and electric fields.

This method of calibration did not turn out to be highly accurate. In any future campaign, the support structure for the antennae should be made from a non-metallic composite material to simplify the vertical electric field calibration.

2.2 Experiment

2.2.1 Philosophy of Experiment

The desired goal of the Interferometer Campaign was to determine the spatial structure of the ELF/VLF modulated currents above an HF heater by using ground based receivers to measure the radiation from many different locations. The measurements
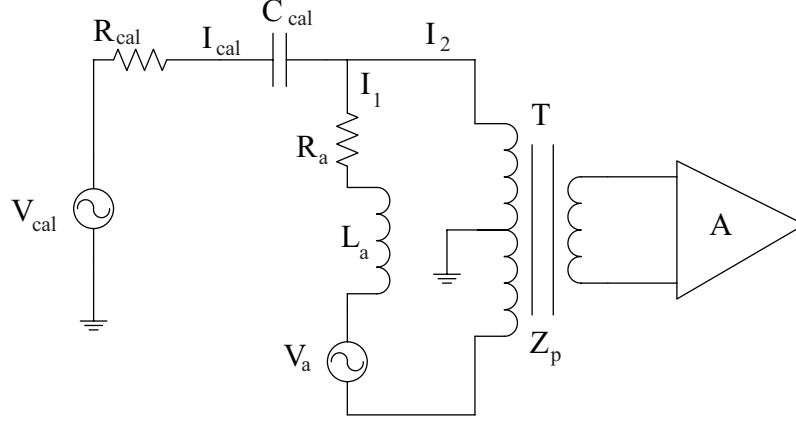
Figure 2.7: Magnetic field preamplifier calibration circuit [*Paschal*, 1988].

are then related to a set of radiating currents by using an electromagnetic propagation matrix. Using linear algebra techniques, the propagation matrix is inverted to determine the currents from the measurements.

Because this process requires many more linearly independent measurements than the number of instruments that are affordable, the experiment assumes that the radiating currents remain invariant if the HF spot is displaced by a small distance. By phasing the elements in the HAARP antenna array properly, the position of the heated spot is altered in a predetermined pattern. At each constant dwell angle, the heated spot remains at a fixed location for one second, giving the Interferometer Units time to record many cycles of the ELF/VLF radiation. This spatial invariance assumption effectively multiplies the number of receivers by the number of dwell angles to obtain the required number of linearly independent measurements.

2.2.2 Campaign Description

From March 31 to April 14, 2003, Stanford University conducted a campaign using nine Interferometer Units. Each day, at 0600, 0700, and 0800 UT, HAARP broadcast
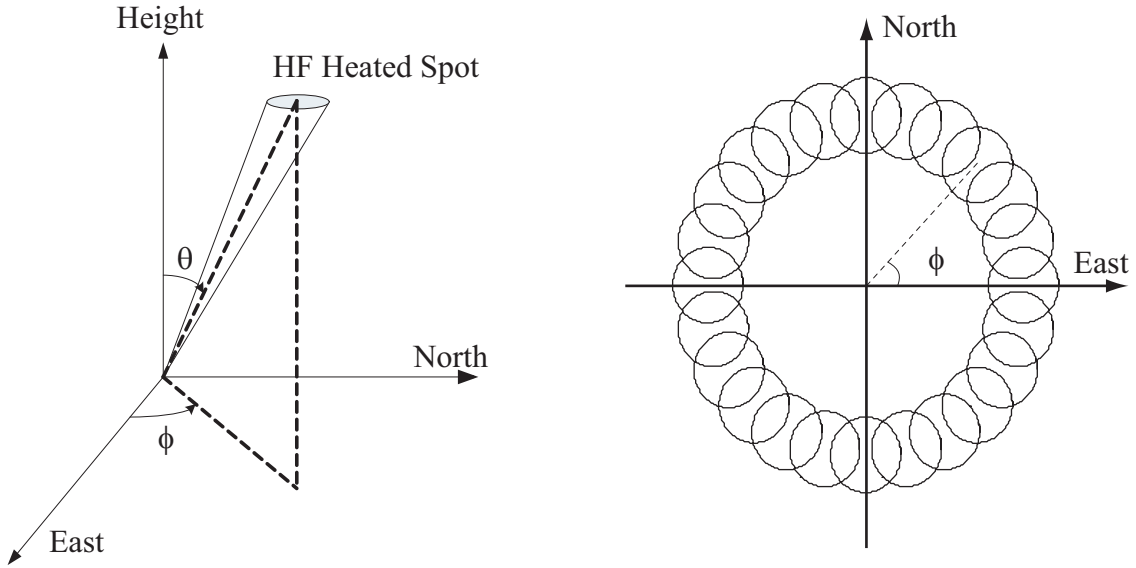
Figure 2.8: The HAARP HF beam was pointed in different directions by rephasing the elements in the transmitter array. As the HF beam moves, the heated spot in the ionosphere is displaced. If the elevation angle is held constant and the azimuth is varied, the heated spot traces out a pattern like the one displayed in the right panel.

a twenty minute predetermined modulation pattern. During this modulation pattern, the array of the HAARP antenna was adjusted to point the HF beam at various positions in the ionosphere. Both 1875 Hz and 2500 Hz signals were generated using sinusoidal and square-wave modulation at each beam dwell angle (HF transmissions were at all times in the X-Mode at 3.2 MHz). The movement of the heated spot and the coordinate system used during the experiment are shown in Figure 2.8.

The location of each site was preselected to create the largest number of independent measurements possible. This involved spacing the Interferometer Units on a giant X that luckily coincided with road patterns near the HAARP facility. Actual locations are given in Table 2.1 and are visually displayed in Figure 2.9. The magnetic declination data for the site locations is taken from the National Oceanographic and Atmospheric Administration website:
(http://www.ngdc.noaa.gov/seg/geomag/jsp/Declination.jsp).

At each site, the preamplifier was bolted onto the antenna structure to keep the circuitry out of the snow. A 500 ft cable was attached to the preamplifier and stretched

Figure 2.9: Map of receiver locations. The HAARP site is designated as HRP.

Site	Lat (N)	Lon (W)	Alt (m)	Dec	Inc
HRP	62° 24.718'	145° 09.420'	604.4	23.6825°	75.7354°
SLA	62° 41.586'	143° 54.711'	676.7	24.2573°	76.1513°
PAX	63° 03.067'	145° 31.332'	947.0	23.8493°	76.1406°
LKL	62° 09.013'	146° 28.920'	919.9	23.0718°	75.3211°
KNL	61° 42.343'	144° 52.722'	420.9	23.4511°	75.2652°
TOK	63° 13.144'	143° 02.536'	548.3	24.8222°	76.6787°
BLK	63° 38.720'	145° 53.639'	566.9	23.9932°	76.5114°
SHP	61° 48.869'	147° 31.194'	911.0	22.5284°	74.9004°
VAL	61° 11.365'	145° 36.373'	516.9	22.9624°	74.7586°

Table 2.1: Interferometer site locations. The table fields given are the site acronym, the latitude, the longitude, the altitude, the declination, and the inclination.

as far as possible. At the end of the cable, a makeshift plywood box was situated, into which the batteries and the line receiver were placed (see Figure 2.10). An attempt was made to accurately align the N/S antenna with Magnetic North and the E/W antenna with Magnetic East. However, some of the sites had limited space for setup and it was not always possible to exactly align the antennae with Magnetic North and Magnetic East. In these cases, a measured skew angle for each antenna was recorded, labeled θ_{skew}.

During the two week campaign, the author drove nearly 18,000 miles collecting data and correcting various errors that occurred. At intermittent times, GPS units failed, batteries died, and CompactFlash devices fried. However, despite these setbacks, the majority of the nine VLF Interferometer systems were kept functioning throughout the campaign.

2.2.3 Post Campaign Data Processing

After the campaign was completed, the data was meticulously cataloged and copied to a data storage computer. During data examination, a number of problems were encountered that must be addressed. This section discusses the various problems and their resolution.
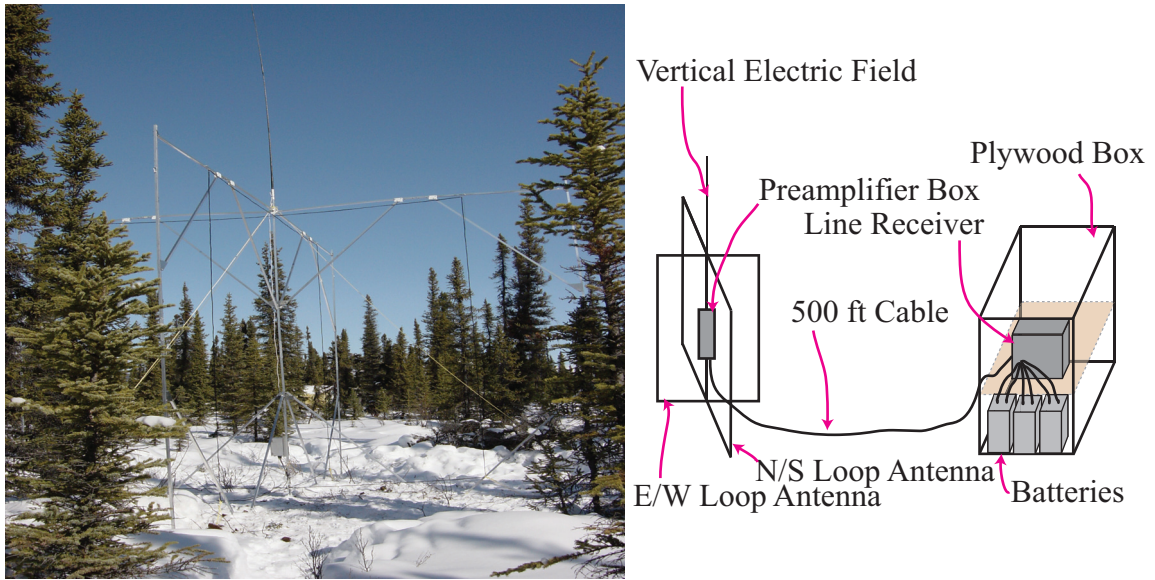
Figure 2.10: The left panel is a photograph of the Interferometer antennae in the field. The right panel is a cartoon example showing the relative location of the magnetic field antennae, the electric field antenna, the preamplifier, and the line receiver.

Time Correlation Error

A timing error occurred sporadically during the campaign because CompactFlash cards were taken from each site, downloaded, and then put into another Interferometer Unit. If a unit failed during a write operation, the data stored on the Compact-Flash would not be new, but would instead be data that had already been downloaded from the previous site. To solve this problem, a program was written to compare data segments between files to ensure the uniqueness of each data sector. If data duplication occurred, the oldest data set was assumed to be valid, while any subsequent copies were discarded.

Data Write Error

When exposed to cold temperatures, the CompactFlash cards were not always able to keep-up with the raw data rate. Data was burst to each card in 128 kB blocks. If a block of data arrived before the previous block was transfered, then the card actually missed the first few bytes of the new block. When looking at the data, these skips

are readily apparent because the data is interleaved by channel, and missing a byte of data causes the channels to exchange! This exchange occurs because the analysis software expects to see CH_1, CH_2, and CH_3 written in order to the CompactFlash. If CH_1 does not write correctly and its spot is taken by CH_2, then the software assumes CH_2 is actually the CH_1 data.

Fortunately, a miss on one block of data is not propagated to the next block. To eliminate such block errors, each data set was examined by hand to determine the location of these errors. These blocks were then removed from any subsequent analysis.

Final Data Check

As a final check on the reliability of the data, each time slot of data from one unit was compared to the same time slot from the other units. Spheric events and their associated timing were compared to ensure that each data set was measured at the correct time. Additionally, each site exhibited a distinct noise background that made recordings from one site unique when compared against recordings at other sites. Using these two basic methods, the remaining data was certified to be valid.

Ensuring Consistency of Antenna Orientation

In practice, loop antennas have a 180° ambiguity with respect to orientation. This occurs because it is very difficult to determine which direction the antenna was wound once the antenna has been fully assembled. In the campaign, a great deal of effort was expended trying to keep the orientation consistent from one Interferometer to another. To ensure that this was accomplished, long distance TM_0 signals associated with lightning discharges were compared between the antennas on each site. Comparing the sign of the spheric pulses on all similarly oriented antennas ensures that the loops are wound in the same direction. Using this method, one loop flip was discovered and corrected. With these corrections, the loop orientations for each magnetic antenna are known to be consistent among all nine deployed devices.

2.2.4   Sample Data

In this section, a few sample spectrograms are displayed from three Interferometer Units showing data collected during the Interferometer Campaign. The purpose here is to illustrate both the variability in the data received, and to catalog the successes of the Stanford Interferometer Campaign.

In Figure 2.11, 100 s of data are shown from the Interferometer Unit located at SLA on April 9th, 2003 at 0600 UTC. The top panel is the signal recorded on the N/S magnetic antenna, the middle panel is the signal recorded on the E/W magnetic antenna, and the bottom panel is the signal recorded on the vertical electric field antenna. The 1875 and 2500 Hz tones generated by modulating the ionosphere are clearly visible in the spectrogram and the signal-to-noise-ratio (SNR) of the data is very good. SLA was the quietest recording site with the best overall SNR throughout the Interferometer Campaign.

In Figure 2.12, 100 s of data are shown from the Interferometer Unit located at BLK on April 9th, 2003 at 0600 UTC. Because BLK is roughly 70 km further from HAARP than SLA, an overall reduction in received signal strength is expected and this is evident in the spectrogram. This reduction in the received signal strength is most visible in the vertical electric field channel. Both 1875 and 2500 Hz tones are clearly visible and the SNR is still good, but not as good as the SNR of the previously shown SLA data.

In Figure 2.13, 100 s of data are shown from the Interferometer Unit located at TOK on April 9th, 2003 at 0600 UTC. This data is an example of 60 Hz power line noise leaking into the system, clearly evident on the N/S magnetic antenna and the vertical electric field antenna. Despite this 60 Hz noise source, the 1875 and 2500 Hz tones are still visible in the data and can be easily extracted through narrow band integration.
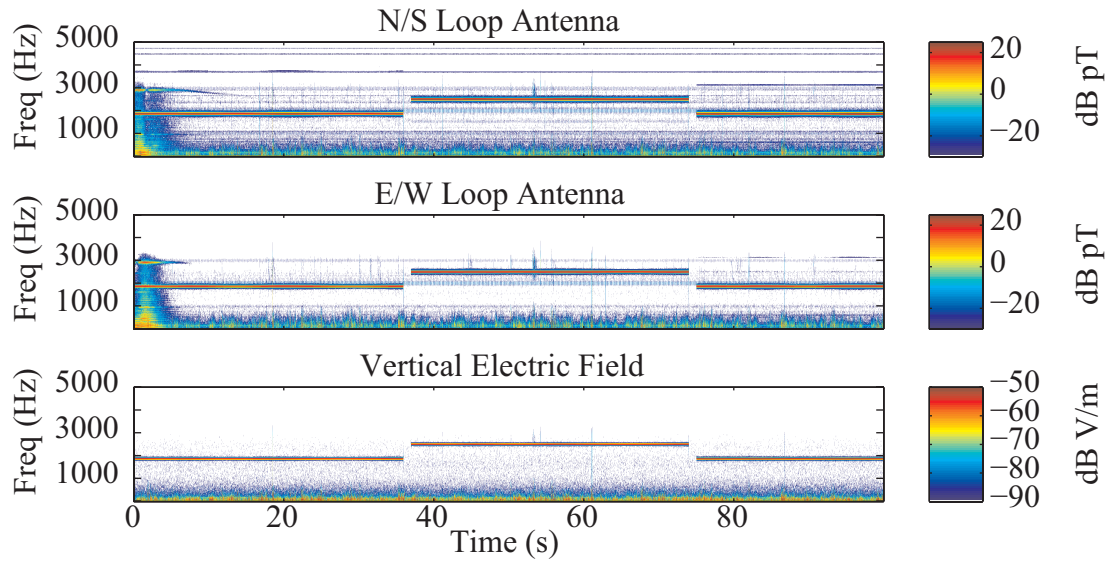
Figure 2.11: Spectrogram taken on April 9th, 2003 at 0600 UTC at SLA. Both the 1875 and 2500 Hz tones are clearly visible on all three channels.
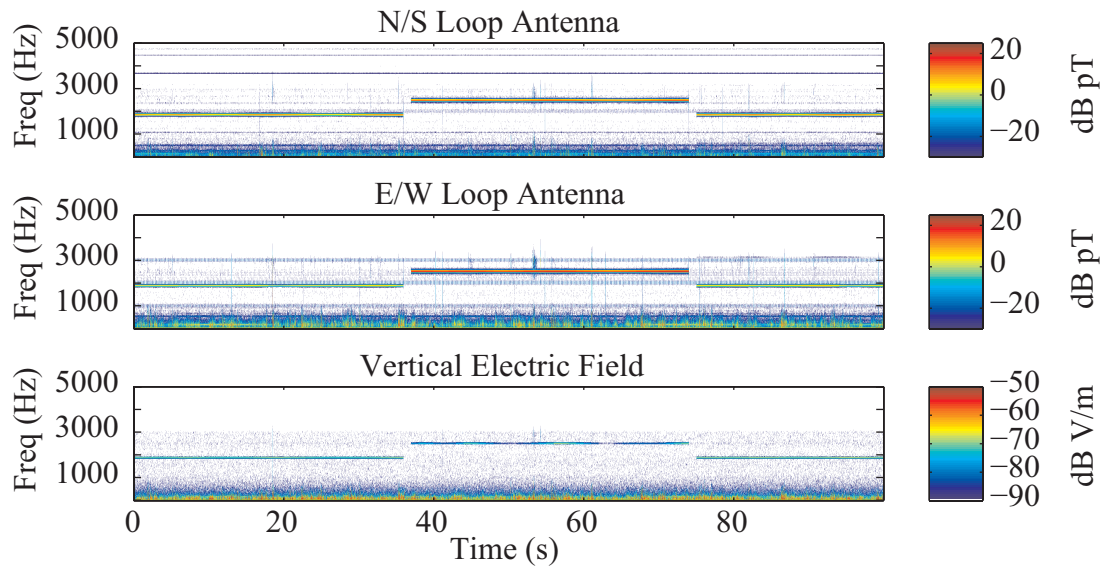
Figure 2.12: Spectrogram taken on April 9th, 2003 at 0600 UTC at BLK. Both the 1875 and 2500 Hz tones are clearly visible on all three channels, although the signal strength is reduced from SLA. This reduction is most notable on the vertical electric field measurement.
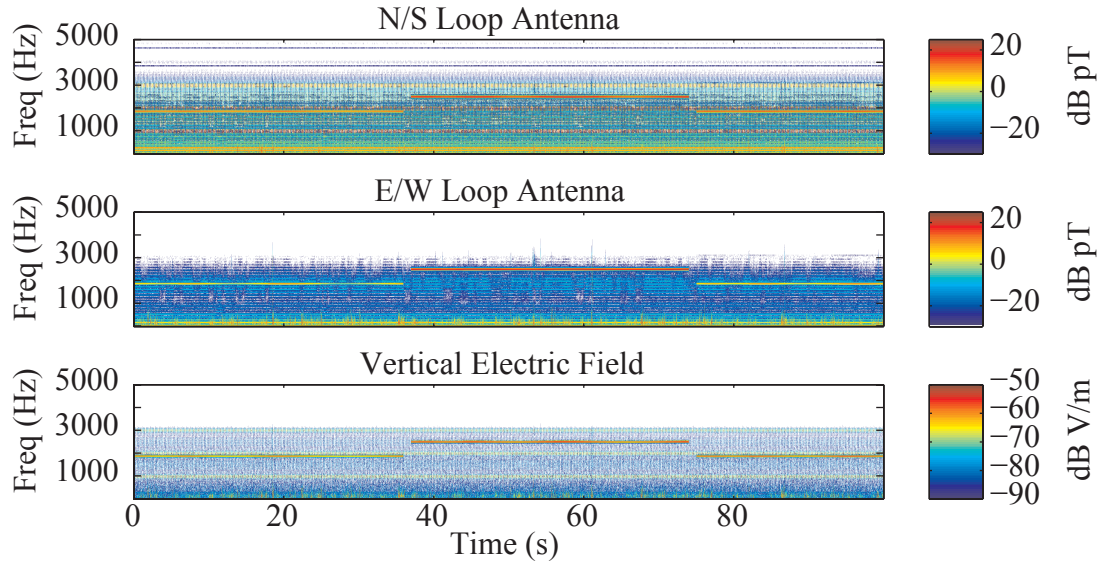
Figure 2.13: Spectrogram taken on April 9th, 2003 at 0600 UTC at TOK. The vertical lines of noise prominent on the N/S channel and the vertical electric field channel are the result of 60 Hz power line noise leaking into the system.

2.3 Instrument Summary

Despite a few setbacks, the instrumentation turned out to be a resounding success. Data was successfully collected from the Interferometer Units, and this data was cataloged and transfered back to Stanford for processing. This post processing revealed a number of defects, which were painstakingly eliminated during the months following the campaign. Finally, this data was calibrated using calibration values derived from each Interferometer Unit.

In the next chapter, the data collected from the Interferometer Campaign are analyzed using advanced linear algebra techniques. While these techniques eventually prove unsuitable for Interferometer data, some interesting theoretical comparisons between inversion techniques are made.

Chapter 3

Direct Inversion

After the Interferometer Campaign and the subsequent data processing, about 30 GB of raw data emerged that was deemed valid. In this section, methods of directly inverting these data sets to determine spatial ionospheric currents are addressed. Our analysis demonstrates that such an inversion is not possible for a number of practical and theoretical reasons. However, some interesting theoretical bounds are obtained and the requirements for the kind of data that would enable such an inversion are determined.

To begin this chapter, a brief discussion of data arrangement and matrix organization is given. Next, a description of the electromagnetic model which underlines the entire inversion process is presented. At this stage, the problem becomes one of numerical matrix inversion and some linear algebra theory and numerical techniques are described. These techniques are then applied and compared to simulated Interferometer data. Simulated data is used instead of actual data because the results are known and can be compared to the output of the inversion code. Finally, some modeling conclusions are presented.

3.1   Data Arrangement

The raw data returned from each Interferometer unit is in the form of 67.5 MB binary data files composed of 16-bit words arranged in the order CH_1, CH_2 and CH_3. Each

file represents recorded output from one instrument for a single 20 minute run of the HAARP heater. CH_1 represents the data from the magnetic loop antenna facing Magnetic North, CH_2 from the magnetic loop antenna facing Magnetic East, and CH_3 that from the vertical electric field antenna.

The first task is to take each file and separate each channel into its own array. This separation is done by taking every third element of the interleaved master file and parsing it into three smaller non-interleaved arrays. Each of these arrays is then separated into sections where the HAARP heater dwells on a constant point in space at a particular frequency. Since the sampling rate is 10 ksps and the HAARP heater dwell time was programmed to be 1 second long, each array contains 10,000 elements. The notation is as follows: $CH_{i,j,k}$ is the 10 k-element-long data vector recorded by instrument j on the ith channel indexed by the kth (θ, ϕ) pair specifying a HAARP beam angle position. For each of these arrays, we take a Discrete Fourier Transform at f and record the complex value.

$$\text{fft}\{CH_{i,j,k}\} \tag{3.1}$$

It is important to note that these Fourier coefficients are just the Fourier coefficients of ADC output values. Before the numbers can have meaning, they must be scaled to represent actual voltages. This scaling is done by noting that the ADC has a ± 10 V input that is divided into 2^{16} possible values. The conversion factor becomes:

$$\text{NumToVolt} = \frac{20}{2^{16} - 1} \tag{3.2}$$

Each of these voltages is the voltage recorded at the ADC input terminals. The calibration results from Appendix B are then used to convert these voltages to magnetic and electric field amplitude values.

It should be noted that all angles programmed into HAARP are given relative to True North, the position where the rotational axis of the Earth intersects the surface of the planet in the northern hemisphere. The receiving antennae are aligned with Magnetic North (plus a measured skew angle), or the direction on the surface of the Earth to which a compass points. To rotate the Magnetic North coordinate system

into the True North coordinate system, the following equations are used:

$$B_x = B'_x \cos(\theta_D + \theta_{skew}) + B'_y \sin(\theta_D + \theta_{skew}) \qquad (3.3)$$

$$B_y = -B'_x \sin(\theta_D + \theta_{skew}) + B'_y \cos(\theta_D + \theta_{skew}) \qquad (3.4)$$

where B'_x is the magnetic field detected on channel 1, B'_y is the magnetic field detected on channel 2, θ_D is the local magnetic declination angle, and θ_{skew} is the measured skew of the antenna. There obviously is no need to rotate the vertical electric field measurement.

Next, the signal-to-noise-ratio (SNR) value of each measurement is examined. During the Interferometer Campaign, intervals existed between transmissions where the background noise could be accessed. These intervals are examined at the frequency of interest and the receiver outputs during times of no transmissions are compared with those during HAARP ELF/VLF modulation. The ratio between these values is interpreted as an SNR measurement and is used to throw away the worst performing measurements.

Finally, the surviving measurements are arranged into a single vector. This arrangement is done by ordering the vector by site first, and then by record time, and finally by channel. The result is the following composite vector $\mathbf{b}$:

$$\mathbf{b} = \begin{bmatrix} B_{x,1,1} \\ B_{y,1,1} \\ c^{-1}E_{z,1,1} \\ \vdots \\ B_{x,j,k} \\ B_{y,j,k} \\ c^{-1}E_{z,j,k} \end{bmatrix} \qquad (3.5)$$

The electric field values are divided by the speed of light to scale the measurements so that the numerical values of the matrix entries are of the same order of magnitude and so that the $\mathbf{E}$ and $\mathbf{B}$ measurements have roughly the same weighting. Without such scaling, the solution of the inversion would depend much more heavily on the

electric field measurements than the magnetic field measurements. It is desirable to have all measurements contribute roughly equally.

3.2 Electromagnetic Model

The basic assumption used in the inversion techniques described in this chapter is the spatial invariance of the HAARP induced currents over the time scale of an entire sweep of all HAARP beam positions, which in practice lasted about 20 minutes. As the HAARP transmitter changes its beam direction, it is assumed that there exists a spatially invariant box of currents that spatially shift location with the HF beam. The currents move and track the beam, but do not change in amplitude or phase.

The electromagnetic model assumes that the oscillating ionospheric currents have a radiation pattern identical to that of a free space current dipole. A perfect ground plane at the surface of the Earth is assumed, a reasonable approximation given the wavelength of VLF waves. The full derivation of the electromagnetic equations is given in Appendix C.

Using the derivations given in Appendix C, a matrix is created which relates each spatial current to a corresponding measurement.

$$a_{ij}x_i = b_j \tag{3.6}$$

In this equation, x_i is a particular current in the model space indexed by i. The subscript i denotes both the position of this current element, and the particular direction that $\mathbf{x}$ flows. For every current in the model space at each HAARP beam dwell angle, the field equations are used to derive a coefficient for each measured field quantity on the ground. The coefficients and equations are then grouped into a single matrix equation:

$$\mathbf{Ax} = \mathbf{b} \tag{3.7}$$

In order to avoid confusion, a simple example can be considered to illustrate the data arrangements used in this inversion. For this example, refer to Figure 3.1. Assume that HAARP broadcasts at beam dwell angles (θ, ϕ): $(0°, 0°)$, $(15°, 0°)$, and
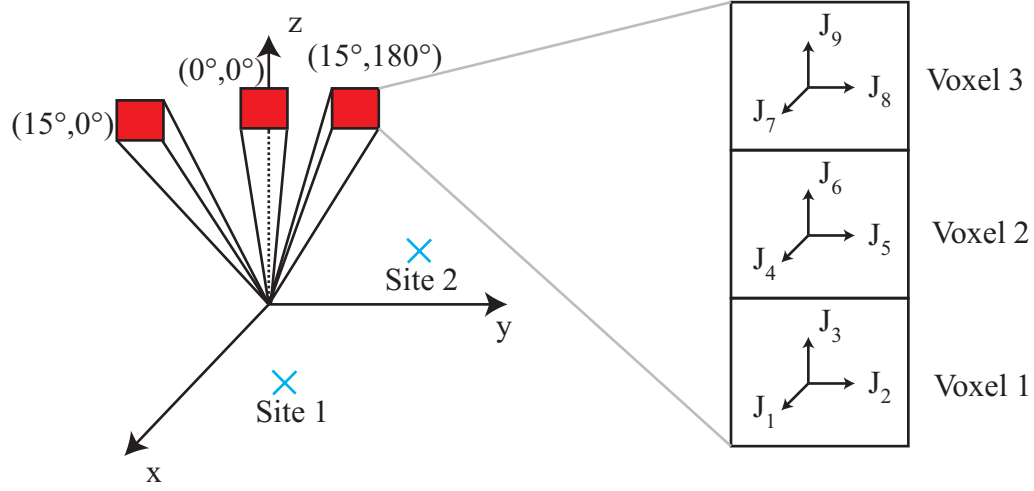
Figure 3.1: Example system containing two receivers, nine currents, and three beam dwell angles. The voxels follow the heated spot such that all nine currents are spatially shifted when the HF beam is pointed in a new direction.

$(15°, 180°)$. Also, assume there are two sites that each measure B_x, B_y, and E_z. Finally, assume that the model space is divided into three voxels containing nine currents.

In the above scenario, there is a current vector containing nine elements: x_i where $i = [1..9]$. Currents $1-3$ represent J_x, J_y, and J_z in the first voxel. Currents $4-6$ represent J_x, J_y, and J_z in the second voxel. Currents $7-9$ represent J_x, J_y, and J_z in the third voxel.

There are 18 total complex measurements: b_j where $j = [1..18]$. Measurements $1-3$ represent B_x, B_y, and $c^{-1}E_z$ at site 1 and $(0°, 0°)$. Measurements $4-6$ represent B_x, B_y, and $c^{-1}E_z$ at site 2 and $(0°, 0°)$. The next measurements represent those taken at site 1, but now for a beam direction of $(0°, 15°)$. The rest of the pattern follows in the same way.

Finally, an 18×9 matrix $\mathbf{A}$ is created which relates $\mathbf{x}$ to $\mathbf{b}$. It is this overdetermined matrix $\mathbf{A}$ and measurement vector $\mathbf{b}$ that contains all the information about the system. All of the electromagnetic theory, antenna parameters, and messy coordinate

systems in the end reduce to the solution of this linear algebra equation.

3.3 Inversion and Optimization Theory

Once the system is described in terms of linear operators, a systematic method must be employed to determine the current vector $\mathbf{x}$ from the measurement vector $\mathbf{b}$. The data used in the Interferometer inversion vectors contains many thousands of measurements related by hundreds of currents. It is impractical, and practically impossible, to do an exhaustive search over all possible input current combinations. Instead, a systematic algorithm must be used which uses the available data to guess at the current arrangements, and systematically refines its guesses to arrive at an approximate solution valid within the measurement constraints.

In this section, a description of a couple of different methods used to invert large overdetermined matrices is presented. These methods are later used to invert model Interferometer data and the performance of each method is explored therein.

3.3.1 Convex Functions and Optimization Problems

A set is convex if the line segment between any two points in the set lies in the set [*Boyd and Vandenberghe*, 2004, p23]. A function f is convex if the domain of the function is convex and if for all $\mathbf{x}$, $\mathbf{y} \in \text{dom } f$, and with $0 \leq \zeta \leq 1$, the following is true [*Boyd and Vandenberghe*, 2004, p67]:

$$f\left[\zeta\mathbf{x} + (1 - \zeta)\mathbf{y}\right] \leq \zeta f(\mathbf{x}) + (1 - \zeta)f(\mathbf{y}) \tag{3.8}$$

A convex optimization problem takes the form

$$\begin{aligned}
\text{minimize} \quad & f_0(\mathbf{x}) \\
\text{subject to} \quad & f_i(\mathbf{x}) \leq b_i, \ i = 1, .., m
\end{aligned} \tag{3.9}$$

where the functions $f_0, ... f_m$ are all convex [*Boyd and Vandenberghe*, 2004, p7].

It is important that optimization problems be convex because there exists powerful

tools to efficiently solve problems of this form. Global optimizers for non-convex problem do not exist. Local optimizers exist for generic non-convex problems, but the output of these optimizers is highly dependent on the initial estimate and on having a good a priori idea of the form of the solution [*Boyd and Vandenberghe*, 2004, p9].

Both the so-called L_1 and the L_2 norm minimization techniques described below are convex problems that are solvable using well developed convex optimization tools.

3.3.2 Singular Value Decomposition

The singular value decomposition (SVD) method is one of the most useful techniques in linear algebra. The SVD reveals a great deal about the structure of a matrix and allows intelligent handling of numerical rank problems [*Golub and Loan*, 1996, p69].

It can be shown that any matrix $\mathbf{A} \in \mathbb{C}^{m \times n}$ where $m \geq n$ can be written as

$$\mathbf{A} = \mathbf{U} \sum \mathbf{V^H} \tag{3.10}$$

where $\mathbf{A} \in \mathbb{C}^{m \times n}$, $\sum \in \mathbb{R}^{m \times n}$ is a diagonal matrix containing the singular values of the matrix $\mathbf{A}$ arranged in descending order, $\mathbf{U} \in \mathbb{C}^{m \times m}$ contains the left singular vectors of $\mathbf{A}$, and $\mathbf{V} \in \mathbb{C}^{n \times n}$ contains the right singular vectors of $\mathbf{A}$. Both $\mathbf{U}$ and $\mathbf{V}$ are orthonormal, meaning that $\mathbf{U}^H \mathbf{U} = \mathbf{I}$ and $\mathbf{V}^H \mathbf{V} = \mathbf{I}$.[1]

The condition number of $\mathbf{A}$ is defined as the ratio of the largest singular value to the smallest.

$$\sum = \begin{bmatrix} \sigma_1 & 0 & \dots & 0 \\ 0 & \sigma_2 & \dots & 0 \\ \vdots & \vdots & \ddots & 0 \\ 0 & 0 & 0 & \sigma_n \end{bmatrix} \tag{3.11}$$

$$\text{Condition Number} = \frac{\sigma_1}{\sigma_n} \tag{3.12}$$

Additionally, the 2-norm norm of matrix $\mathbf{A}$ is equivalent to its largest singular

---

[1]H represents the Hermitian Conjugate. It is equivalent to taking the transpose of the matrix and then conjugating each term.

value σ_1 [*Golub and Loan*, 1996, p71].

3.3.3 L_2 Norm Minimization

L_2 Norm Minimization, better known as *least-squares*, has been the constant ally of engineers and physicists for many decades. Least-squares problems are easy to recognize and can be solved quickly and efficiently using inexpensive desktop computers. Current algorithms are so robust and numerically efficient that problems containing hundreds of free variables and thousands of terms are solvable [*Boyd and Vandenberghe*, 2004].

A least-squares problem is a class of a convex optimization problem with a quadratic objective and no constraints. In optimization terms, it is written as:

$$\text{minimize } f_0(\mathbf{x}) = \|\mathbf{A}\mathbf{x} - \mathbf{b}\|_2^2 = \sum_{i=1}^{m}(\mathbf{a}_i^T\mathbf{x} - b_i)^2 \tag{3.13}$$

In this equation, $\mathbf{A} \in \mathbb{R}^{m \times n}$ and $\mathbf{x}$ is the optimization variable [*Boyd and Vandenberghe*, 2004].

Provided that $\mathbf{A}$ has rank of n, an analytical solution to this problem exists:

$$\mathbf{x} = (\mathbf{A}^T\mathbf{A})^{-1}\mathbf{A}^T\mathbf{b} \tag{3.14}$$

Unfortunately, as is the case with many physical problems, $\mathbf{A}$ turns out not to be full-rank when the numerical accuracy of the measured quantities is considered. The SVD is a tool that is used to determine the degree to which $\mathbf{A}$ is singular by examining the condition number of the matrix.

If the condition number of $\mathbf{A}$ is many orders of magnitude, then the matrix $\mathbf{A}^T\mathbf{A}$ is not of full-rank to within a calculable numerical precision. Thus, $(\mathbf{A}^T\mathbf{A})^{-1}$ is meaningless and the least-squares procedure is bound to fail. More precisely, least-squares returns a perfectly misleading result that should not be confused with the sought for solution.

There are two general categories of physical problems for which a non-invertible

$(\mathbf{A}^T\mathbf{A})^{-1}$ exists. These are *ill-posed* and *rank-deficient* problems. In a classical rank-deficient problem, the singular values of the matrix $\mathbf{A}$ show a discontinuity at the index which corresponds to the rank of $\mathbf{A}$. This discontinuity usually means that several rows of $\mathbf{A}$ are linearly dependent upon each other. In this case, a technique known as *singular value truncation* can be used to generate an approximate solution where the offending eigenvectors are ignored [*Hansen*, 1998, p45].

In the case of an ill-posed problem, the singular values show an exponential decay down to zero. These problems frequently occur in inversions relating to electromagnetic phenomena. The basic question in most ill-posed problems is one of uniqueness; in effect, there are many ways of arranging $\mathbf{x}$ that would accurately approximate $\mathbf{b}$ and it is not clear which of these arrangements is correct. Worse yet, ill-posed problems tend to be numerically unstable; a slight change in input parameters can yield a drastically different solution.

The most popular technique for stabilizing an unstable ill-posed inversion is known as *Tikhonov Regularization* [*Hansen*, 1998, p11]. In this technique, an additional penalty is added to the minimization process

$$\text{minimize } f_0(\mathbf{x}) = \|\mathbf{A}\mathbf{x} - \mathbf{b}\|_2^2 + \lambda \|\mathbf{x}\|_2^2 \tag{3.15}$$

where λ is an empirically derived term that penalizes large numerical values of $\mathbf{x}$. In effect, the regularization process trades accuracy for stability [*Hansen*, 1998, p99].

There is a beautiful mathematical framework that connects L_2 regularization and SVDs. The regularized vector $\mathbf{x}$ can be written in terms of λ, the singular values, and the right and left eigenvectors [*Hansen*, 1998, p72]:

$$\mathbf{x}_{\text{reg}} = \sum_{i=1}^{n} \frac{\sigma_i^2}{\sigma_i^2 + \lambda^2} \frac{\mathbf{u}_i^T\mathbf{b}}{\sigma_i} \mathbf{v}_i \tag{3.16}$$

This framework shows that regularization is a method of filtering out singular values that are smaller than the regularization parameter λ. It also prevents these small singular values, which are usually corrupted by physical and numerical noise, from dominating the solution.

It turns out that L_2 minimization is too sensitive to measurement errors and outlier points, even with regularization, to be effective in reconstructing the ionospheric current system. Thus, a more sophisticated method is required, such as the L_1 norm minimization described next.

3.3.4 L_1 Norm Minimization

The L_1 norm minimization is conceptually very similar to the L_2 norm minimization. In an L_2 minimization, each error penalty, or residual, is the square of the difference between $\mathbf{a}_i^T\mathbf{x}$ and b_i. The total error becomes the sum of these terms over all measured values:

$$\sum_{i=1}^{m} \left|\mathbf{a}_i^T\mathbf{x} - b_i\right|^2 \tag{3.17}$$

In an L_1 minimization, each residual is the absolute value of the difference between $\mathbf{a}_i^T\mathbf{x}$ and $\mathbf{b}_i$. As with the L_2 minimization, the total error becomes the sum of each error term:

$$\sum_{i=1}^{m} \left|\mathbf{a}_i^T\mathbf{x} - b_i\right| \tag{3.18}$$

The small differences between these equations may seem trivial, but they have important implications in both the solution and in the computational complexity of the solution. Qualitatively, least-squares puts an extremely small penalty on small residuals. There is little incentive to further minimize a small error term which gets squared into an even smaller residual term. Additionally, least squares places extremely high penalties for large residuals. The optimizer would rather have many small residuals instead of one large residual. This property tends to make L_2 minimization solutions very susceptible to outlier measurements [*Boyd and Vandenberghe*, 2004, p298].

In contrast, L_1 minimization puts a much higher penalty for small residuals and a much weaker penalty for large residuals. The optimizer would rather have one large residual than many smaller residuals. This property makes L_1 minimization one of the most robust approximation methods with a convex penalty function [*Boyd and Vandenberghe*, 2004, p300].

Unlike L_2 norm minimization, there is no closed form solution to the L_1 minimization problem. Instead, the problem is formulated as a convex conic quadratic problem of the form:

$$\text{minimize} \sum_i t_i \tag{3.19}$$

$$\text{such that } \begin{bmatrix} \mathfrak{Re}(\mathbf{z}) \\ \mathfrak{Im}(\mathbf{z}) \end{bmatrix} = \begin{bmatrix} \mathfrak{Re}(\mathbf{A}) & -\mathfrak{Im}(\mathbf{A}) \\ \mathfrak{Im}(\mathbf{A}) & \mathfrak{Re}(\mathbf{A}) \end{bmatrix} \begin{bmatrix} \mathfrak{Re}(\mathbf{x}) \\ \mathfrak{Im}(\mathbf{x}) \end{bmatrix} - \begin{bmatrix} \mathfrak{Re}(\mathbf{b}) \\ \mathfrak{Im}(\mathbf{b}) \end{bmatrix} \tag{3.20}$$

$$t_i \geq \sqrt{\mathfrak{Re}(z_i)^2 + \mathfrak{Im}(z_i)^2} \tag{3.21}$$

In the above equations, the variables $\mathbf{z} \in \mathbb{C}^m$ and $\mathbf{t} \in \mathbb{R}^m$ are added to the optimization problem. $\mathfrak{Re}(\mathbf{z})$ and $\mathfrak{Im}(\mathbf{z})$ respectively represent the real and the imaginary parts of the residual. The variable t becomes the absolute value of each complex error term. In the context of the above formulation, a complex L_1 minimization problem can be solved using a real valued conic quadratic solver.[2]

A couple of points are worth noting here. Unlike least-squares, there does not exist a framework which connects the SVD to the L_1 minimization solution. The lack of such a framework leads to a problem whose solution time is highly dependent on the problem data. In practice, large L_1 solutions can take 10 seconds, or 10 minutes, just depending on the matrix and measurement values. Such uncertainty of computation time is highly undesirable, because it is extremely difficult to bound program execution time.

L_1 minimization problems also show instability for ill-posed matrices. To stabilize these solutions, Tikhonov Regularization is borrowed from L_2 minimization:

$$\text{minimize } f_0(\mathbf{x}) = \|\mathbf{Ax} - \mathbf{b}\|_1^1 + \lambda \|\mathbf{x}\|_1^1 \tag{3.22}$$

When solving the L_1 norm minimization problem, the matrices and vectors are normalized for better numerical performance. The actual problem that is solved is

$$\text{minimize } f_0(\mathbf{x}') = \left\| \frac{\mathbf{A}}{\|\mathbf{A}\|}\mathbf{x}' - \frac{\mathbf{b}}{\|\mathbf{b}\|} \right\|_1^1 + \lambda \|\mathbf{x}'\|_1^1 \tag{3.23}$$

---

[2]The MOSEK 4.0 conic quadratic solver is used in this dissertation.
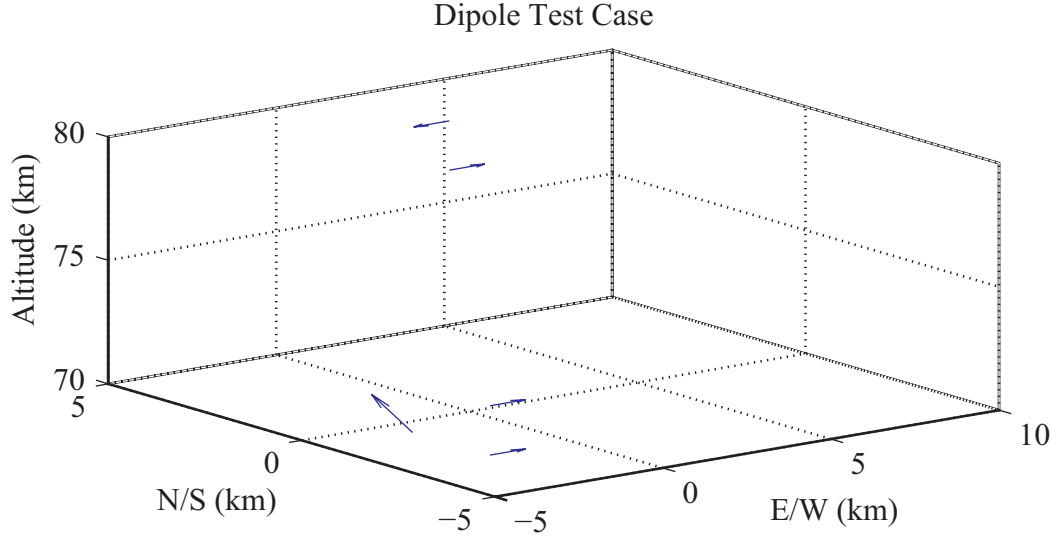
Figure 3.2: 3-D Dipole arrangement used in simulations. Oppositely directed dipole elements in adjacent voxels stress the algorithm.

where $\mathbf{x} = \frac{\|\mathbf{b}\|}{\|\mathbf{A}\|}\mathbf{x}'$. This normalization has the added benefit of decoupling the regularization parameter from the data measurements.

3.4 Model Results

Before showing model results, it is instructive to look at the SVD of the matrix **A** for various resolution decompositions. In Figure 3.3, the ordered singular values are plotted for 12, 10, 8, 6, 4, and 2 km grid spacing. For all grid spacings, the values follow an exponential decay. Additionally, it is seen that the condition number decreases as the grid spacing decreases. The form of these singular values shows that the Interferometer inversion is an ill-posed problem and should be solved with some regularizing solution.

In this section, the L_2 and L_1 minimization with regularization inversion techniques are applied to simulated model data. The purpose of this exercise is to determine whether a direct inversion is feasible, and to quantify the effects of noise and antenna orientation errors on the results.
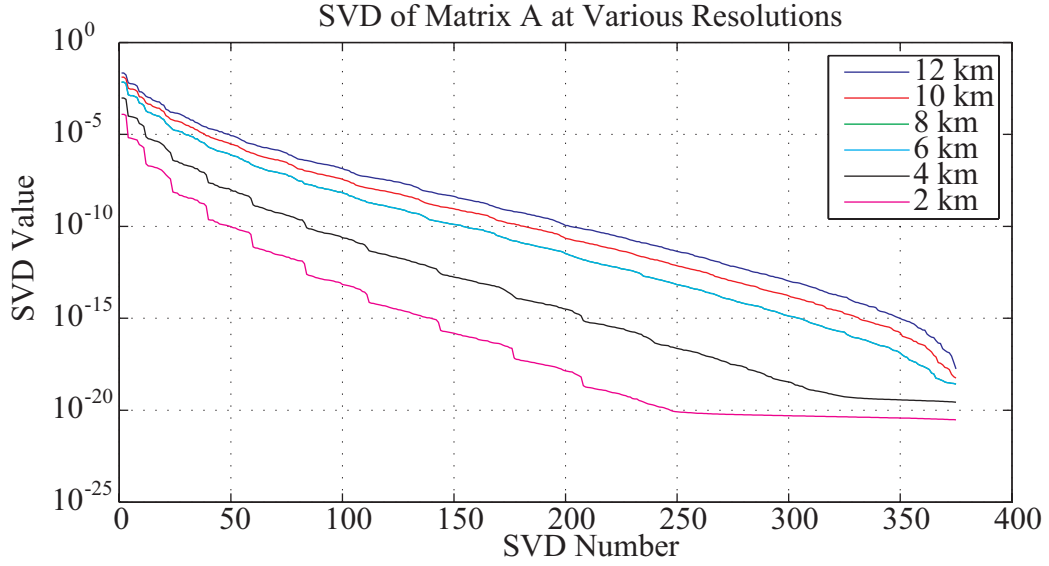
Figure 3.3: Singular values at various grid resolutions. Notice that the condition number increases as the cell spacing decreases.

To generate simulated model data, a standard test case is used which has a known dipole current source arrangement as shown in Figure 3.2. This dipole arrangement includes elements that are contained in adjacent cells but have the opposite phase, elements in adjacent cells that have the same phase, and elements in adjacent cells that are excited by differently directed elements of current. Using this arrangement does not provide an exhaustive test of the ability of the algorithm, but it does provide a rough idea the kind of performance to be expected.

3.4.1 L_2 and L_1 Norm Minimization at Differing Resolutions

In Figures 3.4−3.9, the normalized error of the optimization methods is examined as a function of regularizing parameter and cell spacing. For these cases, the bottom cell of the model space is always set to 70 km, and the cell arrangement is always 5 by 5 by 5. The test vector $\mathbf{x}$ used to generate the measurements $\mathbf{b}$ remains constant during all of the runs. The best guess solution which comes out of the inversion algorithm

is $\mathbf{x}_{\mathrm{reg}}$. The normalized error is defined as

$$\text{Normalized Error} = \frac{|\mathbf{x} - \mathbf{x}_{\mathrm{reg}}|_2}{|\mathbf{x}|_2} \tag{3.24}$$

The purple line on each figure shows the unity error line. Once the normalized error exceeds unity, the error in $\mathbf{x}_{\mathrm{reg}}$ is greater than the magnitude of the exact solution. Above unity error the solution is too corrupted to be interpreted as a legitimate inversion. Any really meaningful result should have a normalized error well below unity.

Using Figure 3.4 as an example, the L_2 norm minimization solution has a minimum error of about 70% at a regularization parameter of $\lambda_{\mathrm{opt}} = 10^{-7}$. Thus, using a least-squares regularizing procedure can, at best, yield a solution that is heavily corrupted by error. The L_1 norm minimization solution has a minimum error of 5% at a regularizing parameter of $\lambda_{\mathrm{opt}} = 10^{-5}$. At 5% error, the reconstructed solution is very close to the original set of input dipoles.

Examining Figure 3.4$-$3.9 closely reveals that the normalized error in the L_2 norm minimization solution never drops significantly below unity. From this observation, it is concluded that the L_2 norm minimization technique is not suitable for solving the Interferometer inversion problem, even at very low resolutions. Using the L_1 norm minimization algorithm, at 12, 10, and 8 km resolutions, the optimum regularizing parameter ($\lambda_{\mathrm{opt}} = 10^{-5}$) yields an error term which is much smaller than unity. Using the optimum regularizing parameter at 6 and 4 km resolution, the minimum error is suppressed below unity, although the error terms are still large. At 2 km, the normalized error never appreciable dips below unity.

Based on the numerical experiments carried out with simulated model data, it is concluded that the L_2 norm minimization algorithm does not have the ability to solve the Interferometer inversion problem. While the L_1 minimization algorithm does show great promise, its susceptibility to measurement errors needs to be explored.

Figure 3.4: Normalized error as a function of regularizing parameter for a resolution of 12 km.

Figure 3.5: Normalized error as a function of regularizing parameter for a resolution of 10 km.

Figure 3.6: Normalized error as a function of regularizing parameter for a resolution of 8 km.

Figure 3.7: Normalized error as a function of regularizing parameter for a resolution of 6 km.
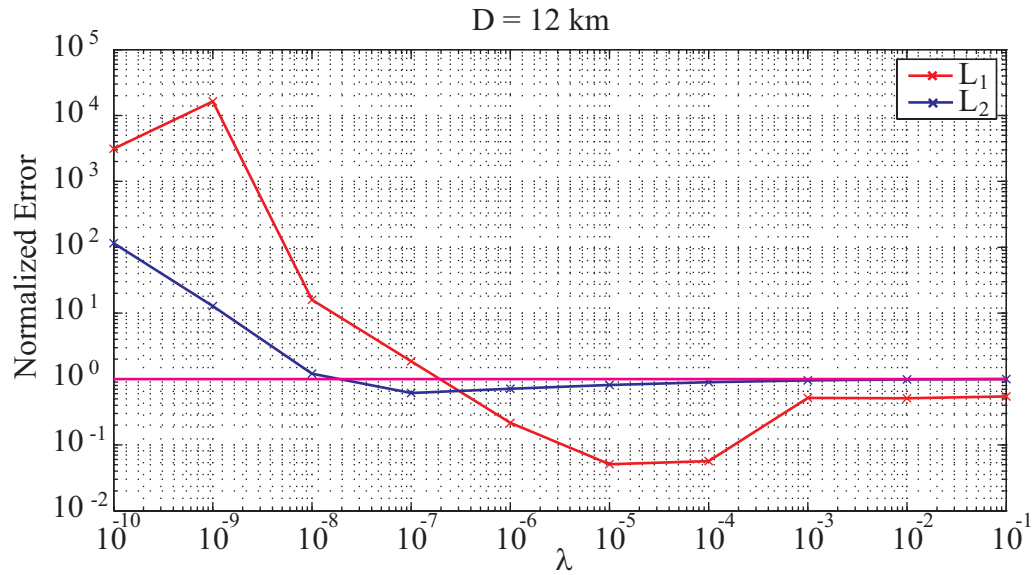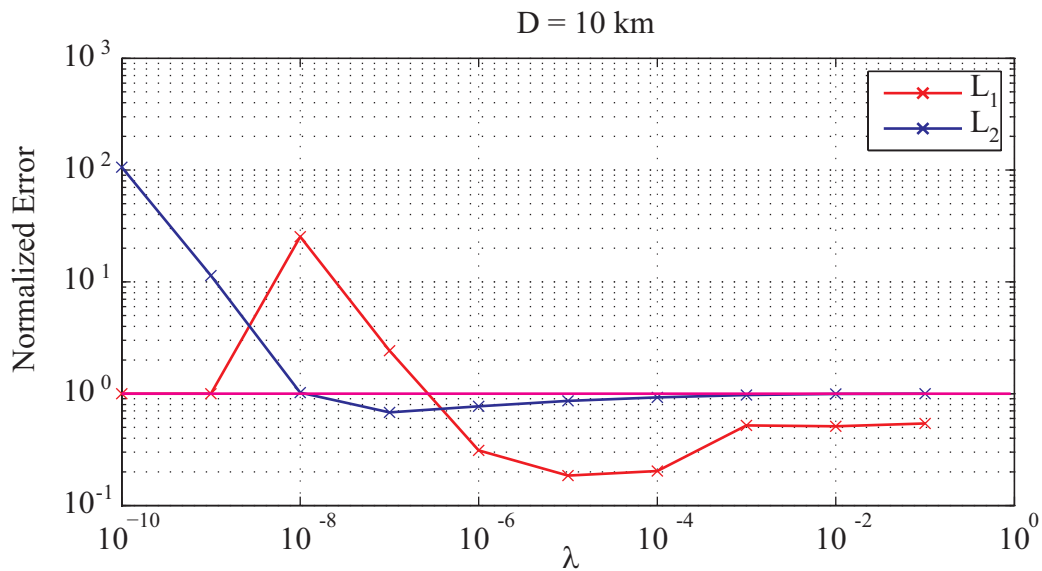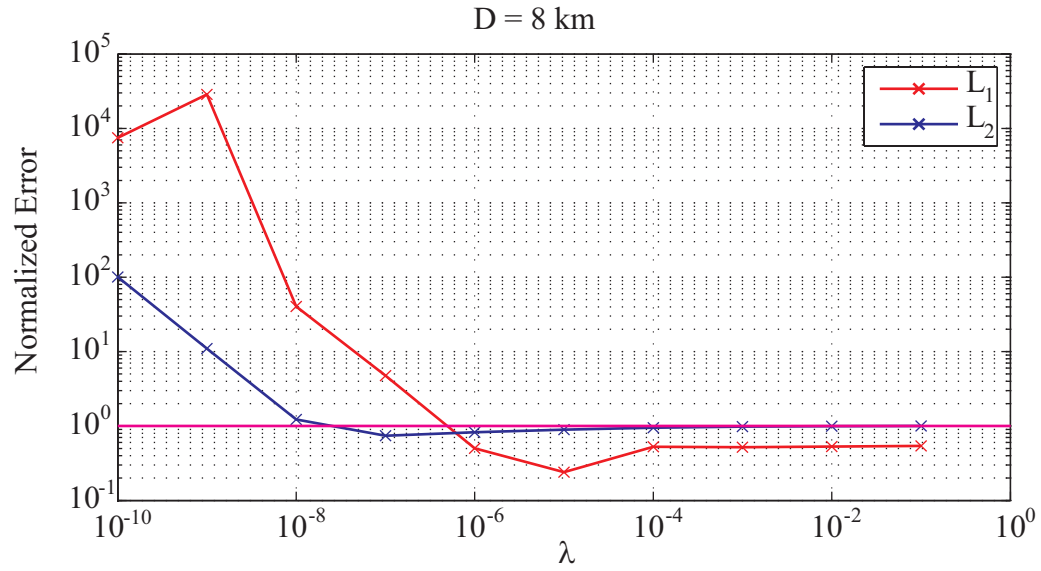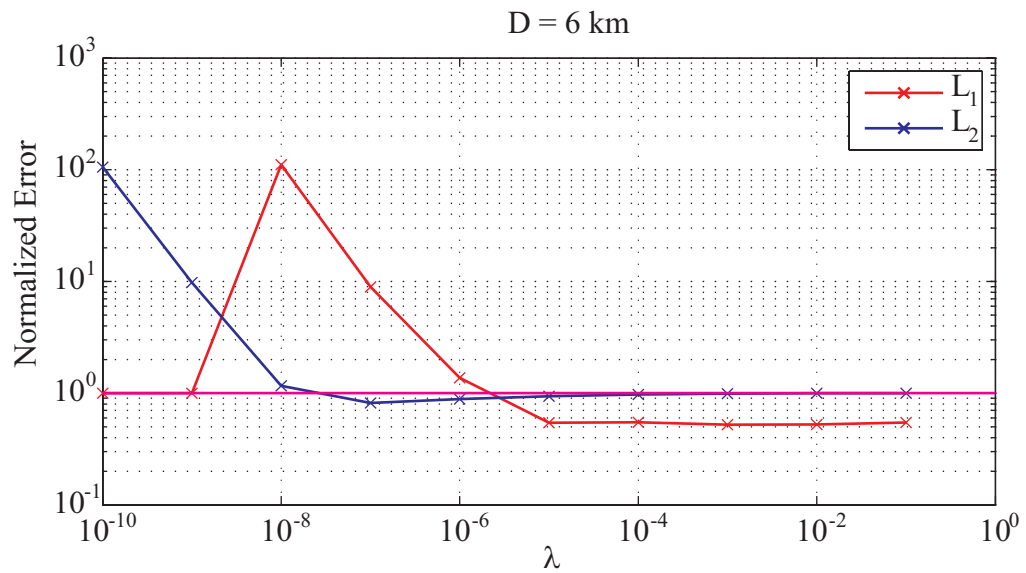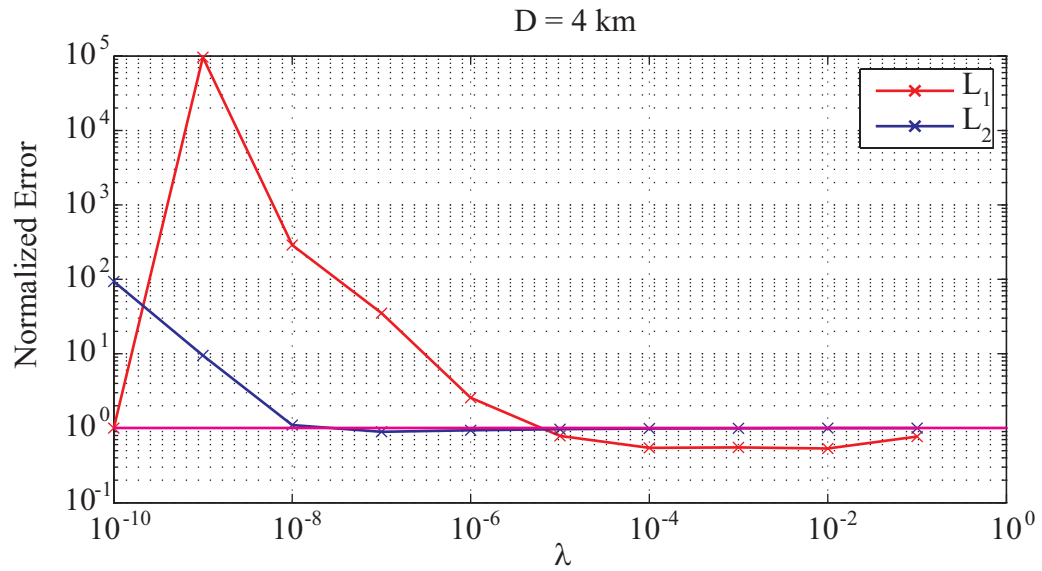
Figure 3.8: Normalized error as a function of regularizing parameter for a resolution of 4 km.
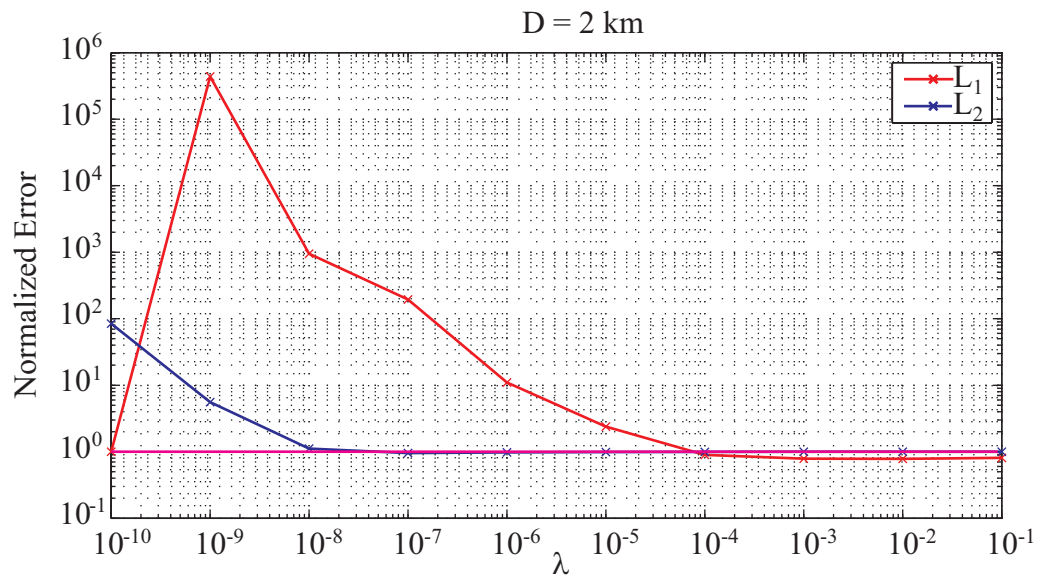
Figure 3.9: Normalized error as a function of regularizing parameter for a resolution of 2 km.

3.4.2 L_1 Norm Minimization with Random Antenna Offset and Calibration

In the previous section, the inversions algorithms were run with simulated noise-free measurement data, the only noise being the numerical precision of the 16-bit word used to store results. Unfortunately, real data is not collected to this precision. Atmospheric noise, circuit noise, power line hum, random antenna offsets, and slight uncertainty in receiver calibration all work to corrupt the actual data.

To test the sensitivity of the system to measurement errors, both the antenna offset problem and the calibration error problem are modeled and their effect on the inversion is calculated. To model antenna offset errors, perfect data is constructed and then skewed by assuming that the actual antenna orientations are not precisely known. Each antenna angle is skewed by a random angle that is Gaussian distributed with zero mean and a standard deviation of 1°. This standard deviation value is much smaller than can reasonably be expected when loop antennas are aligned using a magnetic compass. The calibration errors are modeled in a similar fashion. The calibration factor of each channel is multiplied by a Gaussian distributed random number with mean 1 and standard deviation of 0.01. This operation implies that the calibration values are known to within a percent standard deviation. The result of both Monte Carlo simulations is shown in Figure 3.10.

Even using the optimized regularization parameter, the normalized error is nearly always above unity, even when it is assumed that the calibrations are known to within 1% and the antenna orienations are known to within a standard deviation of 1°. Essentially, this result shows that the system is enormously sensitive to small skews in antenna position and calibration values, even with a very coarse cell resolution. Since it is practically impossible to know the calibration values and the antenna orientations better than 1% and 1°, the inversion problem as stated appears to be impossible to solve.
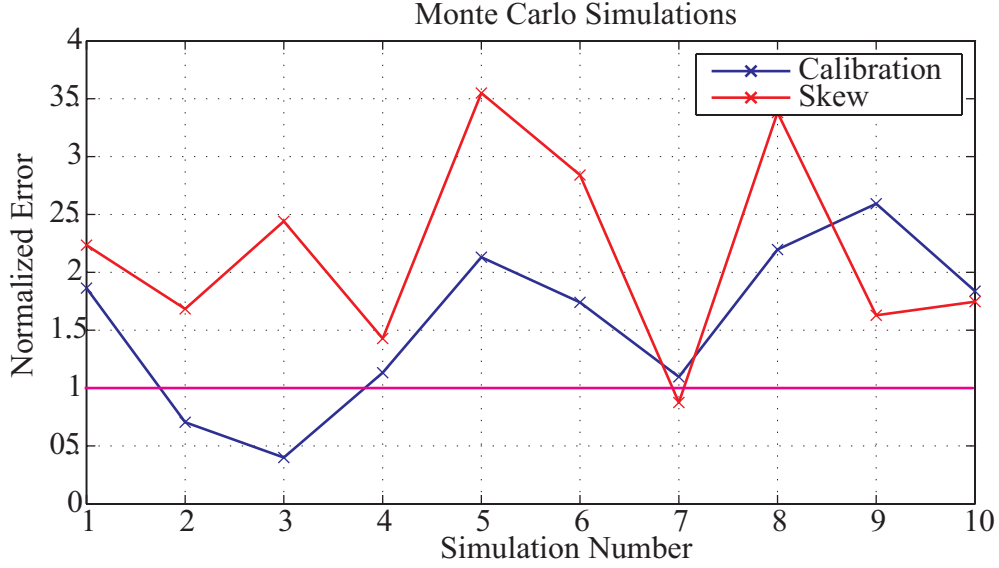
Figure 3.10: Normalized error squared for Monte Carlo runs including systematic antenna skew (red) and calibration errors (blue).

3.5   Direct Inversion Conclusions

This chapter explored the use of L_1 and L_2 norm minimization with regularization on model data to determine whether a direct electromagnetic inversion of the type conceived in the original Interferometer experiment is possible. It is seen that under realistic conditions L_2 norm minimization cannot meet the inversion requirements. Initial success with L_1 norm minimization gives way to practical constraints when noise and systematic offsets are included in the measurements.

The L_1 norm minimization procedure shows great promise for other applications. With simulated model data, the L_1 minimization method shows an improvement in accuracy of $10-15$ times over the standard regularization techniques. However, L_1 norm minimization takes much longer to execute and the execution time is extremely dependent on the form of the data.

In the final analysis, the inversion matrices involved in this experiment are highly singular and it is unlikely that any direct inversion algorithm would be successful when realistic noise and difficult-to-measure systematic offsets are included.

If it is impossible to know the current structure from the received data alone, maybe it is possible to use a combination of physical heating models and electromagnetic data to solve the problem. In the next chapter, a basic HF heating model based on atmospheric physics is described and used to describe ionospheric current formation during HF heating.

Chapter 4

Forward Modeling of Ionospheric Currents

In order to determine the ELF/VLF currents that flow due to modulated HF heating, the electron temperature and conductivity changes that are induced by the HF heater must be accurately modeled. The code that was used for this work is based on the earlier works of *Tomko* [1981], *Rodriguez* [1994] and *Moore* [2007]. In the HF heating model described in this chapter, some simplifying assumptions were added that reduce program execution time so that it is feasible to construct three-dimensional maps of the conductivity change. The program that is described in the first section of this chapter is programmed mostly in C++ and is called 'HModel'. The second section of this chapter examines the results that HModel predicts for HF heating of the ionosphere for three sample ambient ionospheric profiles given in Chapter 1.

   The output of HModel is a 3-D map of the modulated conductivities at the fundamental modulation frequency. These modulated conductivities give rise to primary source currents, which in turn, give rise to secondary conduction, induction, and displacement currents. Calculating these secondary currents is a numerically difficult problem and must be done using a fully coupled wave-plasma Finite Difference Time Domain (FDTD) code. For this thesis, the FDTD code developed by Timothy Chevalier is used [*Chevalier et al.*, 2007]. In section three of this chapter, the equations underlying the FDTD code are introduced and briefly explained. In section

four, the results of these FDTD runs are presented.

4.1 HF Heating Model

In this section, an in-depth look at the HF heating model is presented. The heating model takes as an input an ambient density profile[1], an initial HF ray path defined in 3-D and wave power flux density value, and propagates the given ray through the ionosphere, solving a self-consistent system of differential equations that relate electron temperature to the power flux in the ray. This electron temperature is then transformed into plasma conductivity values, which are linearly related to the primary conduction currents that drive ELF/VLF wave generation in the lower ionosphere.

4.1.1 Precomputation

In HModel, it is assumed that the ionosphere is composed of horizontal thinly stratified layers of plasma. In each horizontal layer, the plasma parameters and the index of refraction remain constant. Additionally, it is assumed that the ray paths do not bend by an additional amount as a result of HF heating. This assumption is justified, since for the heating runs presented here the additional deflection angle due to HF heating amounts to a few tenths of a degree at most. By not having to recalculate the position of the ray due to the heating, a huge computational savings is netted. In this context, it should be noted that the bending of the HF ray due to the ambient plasma gradients is accounted for. Finally, it is assumed that the k-vector is parallel to the ray vector.

HModel begins by determining the thickness of each stratified layer. This determination is done by setting a tolerance that allows a maximum deviation of plasma parameters over the full thickness of each layer. When plasma parameters change fast with altitude, the layers are kept very thin. When the plasma parameters change slowly, the layers are made thicker. This technique allows a high degree of accuracy to be maintained without incurring needless computational cycles.

---

[1]The electron, molecular nitrogen, and molecular oxygen profiles are input as a function of altitude. Additionally, the neutral temperature is input as a function of altitude.

Using the stratified layer approximation, the wavenormal of each ray through the ionosphere is calculated using Snell's Law

$$\mathfrak{Re}(n_i) \sin \Theta_i = \mathfrak{Re}(n_r) \sin \Theta_r \tag{4.1}$$

where n_i is the incident index of refraction, n_r is the refracted angle of refraction, Θ_i is the incident angle and Θ_r is the refracted angle. Equation 4.1 holds so long as the imaginary parts of the index of refraction remain small compared to the real part [*Budden*, 1985, p142]. Examining the calculated indices of refraction in the D-region plasma, the imaginary part is found to be generally 3 to 4 orders of magnitude smaller than the real part. Thus, it is reasonable to use Snell's Law only in terms of the real quantities, as stated in Equation 4.1.

Within each slab the index of refraction is computed using the Appleton-Hartree equation which is a function of the angle between the k-vector of the wave and the magnetic field **B**. An iterative algorithm ensures that the angle dependent index of refraction in the magnetized plasma is consistent with the refraction angle. Once the direction of each k-vector is determined, it remains constant for the remainder of the program execution.

4.1.2   Temperature Modulation

The fundamental energy equation used to determine the electron temperature in the ionosphere models the exchange of energy between the EM wave and the electrons in the plasma. This equation is:

$$\frac{dT}{dt} = \frac{2}{3N_e k_{\mathrm{b}}}(Q - L) \tag{4.2}$$

where T is the electron temperature, L represents the loss terms due to the plasma, and Q is the energy being added by the EM wave, N_e is the ambient electron concentration, and k_{b} is Boltzmann's constant [*Tomko et al.*, 1980].

The energy lost by the wave is calculated from the imaginary part of the index of

refraction

$$Q = 2\frac{\omega}{c}\chi S \tag{4.3}$$

where S is the HF wave power density and χ is the imaginary part of the index of refraction [*Tomko et al.*, 1980].

At a given stratified layer, the energy exchange equations must be combined in a self-consistent way with the formula for the index of refraction. The following form of the Appleton-Hartree Equation is used:

$$n^2 = \frac{\epsilon_1\epsilon_2\sin^2\Theta + \frac{1}{2}\epsilon_3(\epsilon_1 + \epsilon_2)(1 + \cos^2\Theta) + S}{(\epsilon_1 + \epsilon_2)\sin^2\Theta + 2\epsilon_3\cos^2\Theta} \tag{4.4}$$

where

$$S = \pm\left\{\left[\epsilon_1\epsilon_2 - \frac{1}{2}(\epsilon_1 + \epsilon_2)\epsilon_3\right]^2\sin^4\Theta + \epsilon_3^2(\epsilon_1 - \epsilon_2)^2\cos^2\Theta\right\}^{\frac{1}{2}} \tag{4.5}$$

and

$$\epsilon_1 = 1 - \frac{X}{1 + Y - iZ} \tag{4.6}$$

$$\epsilon_2 = 1 - \frac{X}{1 - Y - iZ} \tag{4.7}$$

$$\epsilon_3 = 1 - \frac{X}{1 - iZ} \tag{4.8}$$

and

$$X = \frac{\omega_{pe}^2}{\omega^2} \tag{4.9}$$

$$Y = \frac{\omega_{ce}}{\omega} \tag{4.10}$$

$$Z = \frac{\nu_{eff}}{\omega} \tag{4.11}$$

and

$$\omega_{pe} = \sqrt{\frac{N_e q_e^2}{\epsilon_0 m_e}} \qquad (4.12)$$

$$\omega_{ce} = \frac{q_e B_0}{m_e} \qquad (4.13)$$

Note that the "−" sign associated with S is appropriate for the extraordinary mode (X-mode) and the "+" sign is appropriate for the ordinary mode (O-mode). For the Interferometer Campaign, X-mode heating was used, and such is assumed to be the case in all of the model calculations.

A time difference method is used to solve Equation 4.2, combined with the loss rates and the Appleton-Hartree equation. The time step is selected such that the solution for the temperature converges during a run. Experimentally, it was determined that a time step of 1 μs provides a reasonable trade-off between execution speed and temperature convergence.

Once Equation 4.2 is solved, the power loss in the ray both due to spreading and absorption is calculated. The altitude dependence of wave power density is given by:

$$S(h) = S_0 \left(\frac{h_0}{h}\right)^2 exp\left[-2k\int_{h_0}^{h} \chi(h')dh'\right] \qquad (4.14)$$

$$S_0 = \frac{P_T G}{4\pi h_0^2} \qquad (4.15)$$

where P_T is the transmitter power, G is the antenna gain, k_0 is the free space propagation constant, and χ is the absorption index at height h' [Tomko et al., 1980]. Because reflections at each interface are ignored, the propagation problem is decoupled at each stratified layer and can be solved sequentially at each slab.

The input to each plasma layer is the power in the ray as a function of time over several modulation cycles. The output of the algorithm is the power as a function of time in the ray as it leaves the stratified layer, and the electron temperature of the plasma in the slab over a few modulation cycles. The power in the ray as it leaves the slab becomes the input to the next layer. In this way, the modulated

temperature is systematically solved along the propagation path of the ray. The modulated temperature is used to compute the conductivity change.

4.1.3 Propagation Delay

It is worth noting that the modulated HF wave propagates at the group velocity through the ionosphere [*Budden*, 1985, p128-129]. It is important for the model to keep track of propagation delay, so that individual conductivity elements have the proper phase relationship relative to each other within each modulation cycle. This phasing becomes important when the currents are derived from the conductivities, and the radiation from these currents is propagated to the ground.

To calculate the group velocity along the direction of the ray, the following formula is used [*Budden*, 1985, p131]

$$n' = n + \omega\frac{\partial n}{\partial \omega} = \frac{n^4\left(A - \frac{1}{4}\omega\frac{\partial A}{\partial \omega}\right) - n^2\left(B - \frac{1}{2}\omega\frac{\partial B}{\partial \omega}\right) - \frac{1}{4}\omega\frac{\partial C}{\partial \omega}}{n(n^2A - B)} \tag{4.16}$$

$$A - \frac{1}{4}\omega\frac{\partial A}{\partial \omega} = \left[\begin{array}{c} 1 - \frac{3}{2}X - Y^2\left(\frac{3}{2} - 2X\right) - 2XY^2\sin^2\Theta + \frac{1}{2}Z^2\left(4X - 9\right) \\ +\frac{1}{4}iZ\left(14X + 7Y^2 + 7Z^2 - 15\right) \end{array}\right] \tag{4.17}$$

$$B - \frac{1}{2}\omega\frac{\partial B}{\partial \omega} = \left[\begin{array}{c} (1 - X)(1 - 3X - 6Z^2) - Y^2(2 - 3X) - \frac{3}{2}XY^2\sin^2\Theta \\ +\frac{1}{2}iZ\left(20X - 7X^2 + 5Y^2 + 5Z^2 - 9\right) \end{array}\right] \tag{4.18}$$

$$-\frac{1}{4}\omega\frac{\partial C}{\partial \omega} = \left[\begin{array}{c} -\frac{3}{2}X(1 - X)^2 - Y^2\left(\frac{1}{2} - X\right) - \frac{3}{2}Z^2 + 3XZ^2 \\ +\frac{3}{4}iZ\left(6X - 5X^2 + Y^2 + Z^2 - 1\right) \end{array}\right] \tag{4.19}$$

where X, Y, and Z are given in 4.9, 4.10, 4.11, Θ is the angle between $\widehat{\mathbf{k}}$ and $\mathbf{B}$, and A and B are given below.

$$A = U^2(U - X) - Y^2(U - X) - XY^2\sin^2\Theta \tag{4.20}$$

$$B = U(U - X)^2 - Y^2(U - X) - \frac{1}{2}XY^2\sin^2\Theta \tag{4.21}$$

and

$$U = 1 - iZ \tag{4.22}$$

n' is known as the group refractive index and gives the ratio of the speed of light to the group velocity [*Budden*, 1985, p44, 78].

4.1.4 Conductivity Modulation

Once the temperature is known at a given point in space, the DC conductivity is computed at the same location. The starting point is the Maxwell-Boltzmann Equation for the electron velocity distribution

$$f_{e,0} = N_e \left(\frac{m_e}{2\pi k_b T_e} \right)^{3/2} \exp\left(\frac{-m_e v_e^2}{2k_b T_e} \right) \tag{4.23}$$

where N_e is the electron density, m_e is the mass of an electron, k_b is Boltzmann's Constant, T_e is the electron temperature, and v_e is the velocity of the electron [*Tomko*, 1981, p26].

The derivative of this function with respect to velocity is needed to compute the conductivity tensor.

$$\frac{\partial f_{e,0}}{\partial v_e} = -N_e \left(\frac{m_e}{2\pi k_b T_e} \right)^{3/2} \left(\frac{m_e v_e}{k_b T_e} \right) \exp\left(\frac{-m_e v_e^2}{2k_b T_e} \right) \tag{4.24}$$

The Pedersen conductivity for a wave with frequency ω is [*Tomko*, 1981, p32]

$$\sigma_P = \frac{4\pi}{3} i \frac{q_e^2}{m_e \omega} \int_0^\infty \frac{U}{U^2 - Y^2} v_e^3 \frac{\partial f_{e,0}}{\partial v_e} dv_e \tag{4.25}$$

The Hall conductivity for a wave with frequency ω is [*Tomko*, 1981, p32]

$$\sigma_H = \frac{4\pi}{3} \frac{q_e^2}{m_e \omega} \int_0^\infty \frac{Y}{U^2 - Y^2} v_e^3 \frac{\partial f_{e,0}}{\partial v_e} dv_e \tag{4.26}$$

The Parallel conductivity for a wave with frequency ω is [*Tomko*, 1981, p32]

$$\sigma_{||} = \frac{4\pi}{3} i \frac{q_e^2}{m_e \omega} \int_0^\infty \frac{1}{U} v_e^3 \frac{\partial f_{e,0}}{\partial v_e} dv_e \qquad (4.27)$$

Each of these quantities is evaluated using a numerical method based on Simpson's Rule, creating a time series waveform at each spatial point. In the above equations, the limit is taken as $\omega \to 0$.

4.1.5   Fourier Extraction

Because of the limited bandwidth of the Interferometer, it is not possible to look at the higher order harmonics produced during modulation. Thus, it makes sense to reduce each time series of conductivity into a single Fourier coefficient.

$$\sigma_\omega(\mathbf{r}) = \text{fft} \left[\sigma(t, \mathbf{r}) \right] \qquad (4.28)$$

For the remainder of this dissertation, when discussing conductivity, $\sigma_\omega(\mathbf{r})$ is the quantity being discussed.

4.1.6   Beam Fitting

The HAARP beam is approximated with a 2-D function of the azimuth and elevation angles. This representation is based on matching the Gaussian beam shape to the half-power angles given by the HAARP website:[2]

$$S(\theta, \phi) = S(0, 0) \exp \left[\frac{\theta^2}{2\sigma_{\text{std}}^2(\phi)} \right] \qquad (4.29)$$

where $S(0, 0)$ is the power at the center of the beam, and σ_{std} is the standard deviation which is itself a function of ϕ. The quantity $\sigma_{\text{std}}(\phi)$ is solved for the half-power angles, and then linearly interpolated between to complete the function. The resulting beam shape for a vertical beam profile are shown in Figure 4.1.

---

[2]The URL is http://www.haarp.alaska.edu/haarp/calciri.html
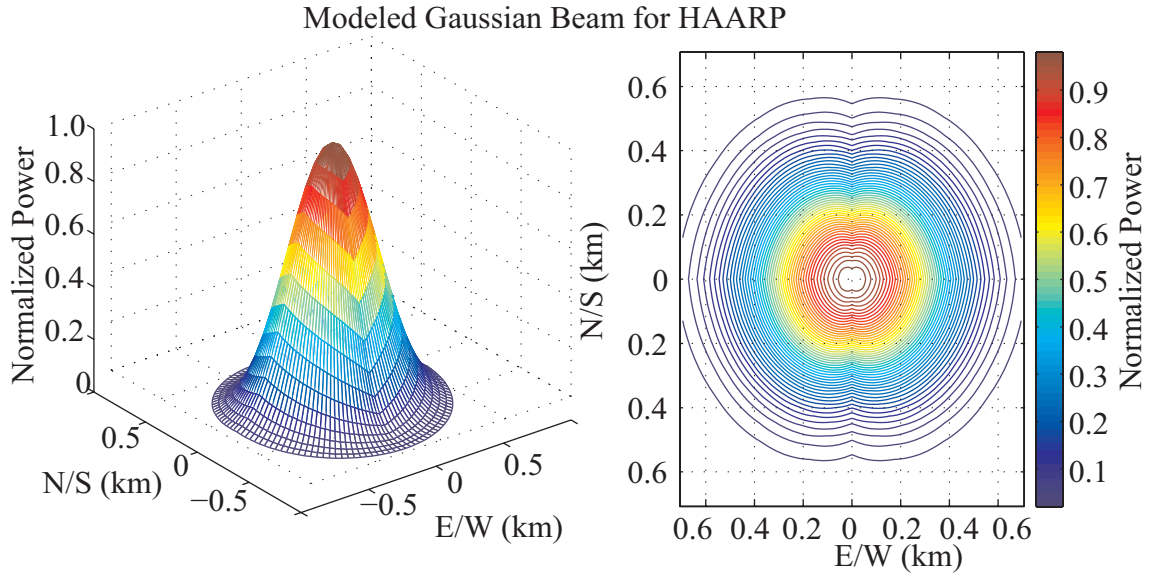
Figure 4.1: Angular Gaussian fit to HAARP antenna pattern. The intensity is taken at a plane 1 km above the HAARP HF heating array.

The numerical space is sampled with many rays uniformly separated in terms of angle. These rays are individually fed into HModel and the output is combined using an interpolation method as described below. The ray paths for a vertically directed beam are shown in the left panel of Figure 4.2.

4.1.7   3-D Interpolation

All of the Fourier coefficients are arranged onto a 3-D grid and then interpolated. Ideally, the best way to interpolate data from a non-uniformly spaced grid[3] is to fit all of the data to a 3-D hypersurface and then use the resultant hypersurface function to find the interpolated grid points. However, because of the amount of data generated, the hypersurface fitting functions available were not able to determine the hypersurface function even after several days of computational time. Thus, a two stage interpolation method is used where a 2-D hypersurface is fit to all data at a given altitude. The vertical dimension is then interpolated using a 1-D cubic interpolation function. This combined two-step operation can be completed in several

---

[3]The rays are evenly spaced in angle, not in Cartesian coordinates.
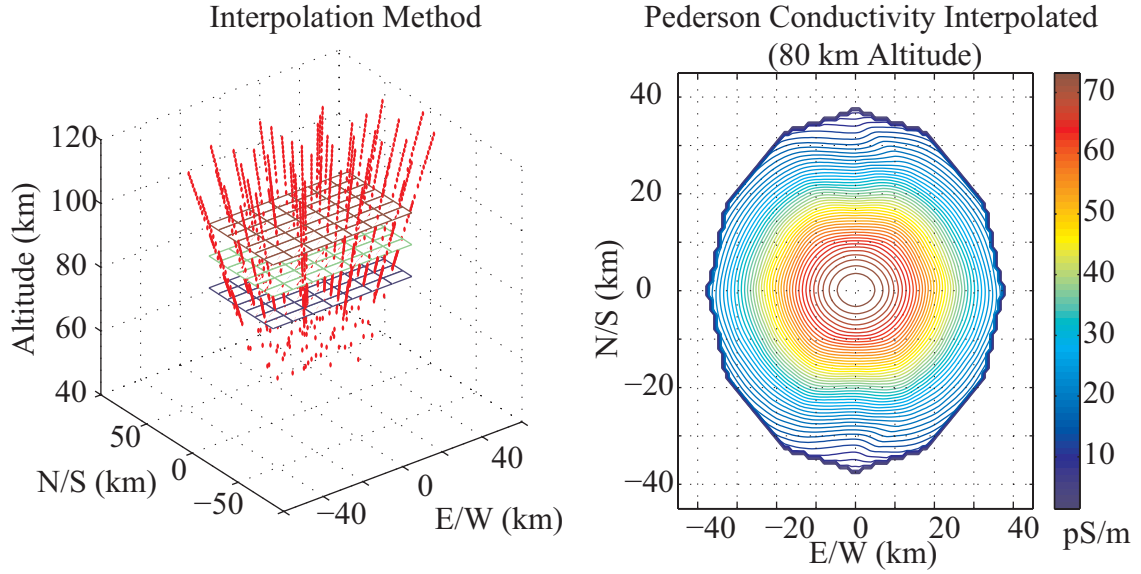
Figure 4.2: Two-step method of interpolating 3-D data. The modulated conductivity values are known on the 2-D planes that coincide with the stratified layers of the ionospheric plasma as shown in the left panel. The values on each plane are interpolated onto a regular grid as shown in the contour plot displayed in the right panel.

minutes of computational time.

The two step interpolation works because the data is sampled at much greater resolution in the vertical compared with the horizontal dimension. Thus, a simple interpolation method is needed vertically and a more complicated method is needed in the horizontal dimension. Figure 4.2 shows a set of rays propagated through the ionosphere in this manner. The modulated conductivity values are known at each stratified plasma layer, displayed as planes in the left panel of Figure 4.2. Each stratified plasma layer is a 2-D horizontal plane parallel to the ground. A regular grid is superimposed onto this plane, and the modulated conductivity values are interpolated onto this regular grid. To determine points on a plane that is above or below the known planes, the two nearest planes are interpolated.

4.1.8 Primary Modulated Currents

Because the conductivity is modulated in a region of the ionosphere where an ambient electric field is present, a primary source current arises that tracks the modulation of the conductivity values. In the anisotropic magnetoplasma medium, the current is represented as a phasor using the following relationship:

$$\mathcal{J}_{\mathrm{p}}(\omega) = \bar{\sigma}_{\omega}(\mathbf{r})\mathbf{E}_{\mathrm{a}} \tag{4.30}$$

where the conductivity phasor is defined as:

$$\bar{\sigma}_{\omega}(\mathbf{r}) = \begin{bmatrix} \sigma_{\mathrm{P}}(\mathbf{r}) & \sigma_{\mathrm{H}}(\mathbf{r}) & 0 \\ -\sigma_{\mathrm{H}}(\mathbf{r}) & \sigma_{\mathrm{P}}(\mathbf{r}) & 0 \\ 0 & 0 & \sigma_{\parallel}(\mathbf{r}) \end{bmatrix} \tag{4.31}$$

At first thought, it might appear that these currents can be straightforwardly used as the source currents for the ELF/VLF radiation. However, these primary conduction currents give rise to charge accumulation at the boundaries of the heated region and a resulting perturbing electric potential. Because the charge accumulation is small compared to the ambient electric field, the extra potential does not appreciably change the electric field in the horizontal plane, but the resultant enhancements of the vertical electric field can cause currents to flow because of the comparatively large parallel conductivity. Additionally, there are induction currents and displacements currents to consider. To correctly treat all the currents in detail requires a full electromagnetic plasma interaction model. Thankfully, a fully coupled wave plasma FDTD code has already been developed at Stanford University by another PhD student in the VLF research group and was available for use in this dissertation. The predictions of this FDTD code are explored later in this chapter.

4.2   HF Modeling Results

In this section, HF heating model results are presented using the profiles shown in Chapter 1. All of these models are run using sinusoidal modulation at 1875 kHz, at full HAARP power, with an HF beam at 3.2 MHz transmitting in X-mode. Results of sample electron temperature runs are shown, which lead to the various conductivity predictions, which finally leads to the determination of the primary ELF/VLF current structure.

4.2.1   Electron Temperature Modulation

In Figure 4.3, the electron temperature is plotted as a function of altitude for each ambient profile. Since each point in space has an associated time domain waveform, the data set is reduced by only plotting the maximum, the average, and the minimum temperature for each altitude slice. At each altitude, the electron temperature is modulated between the minimum and the maximum at the modulation frequency. The modulation depth is defined as the difference between the maximum and the minimum electron temperature at each altitude.

Figure 4.3 clearly shows that the HF energy is absorbed between 60 and 90 km for all three profiles. Profile I has a maximum modulation depth of 431 K occurring at 77 km. For Profile II, the electron density is greater than in Profile I, and this shows as the energy is absorbed in a slightly thinner region of the ionospheric plasma. However, the maximum modulation depth still occurs at 77 km with a value of 427 K. Finally, for Profile III, the electron density is even higher than for Profile II. The energy is absorbed in an even thinner region of the ionosphere, and the altitude of maximum modulation depth is 75.4 km with a value of 395 K.

Both the maximum modulation depth, and the altitude where this maximum occurs are very similar when comparing the output of Profiles I, II, and III. Essentially, this result implies that the peak altitude and depth of modulation in HF heating is rather insensitive to the ambient ionospheric density profiles.
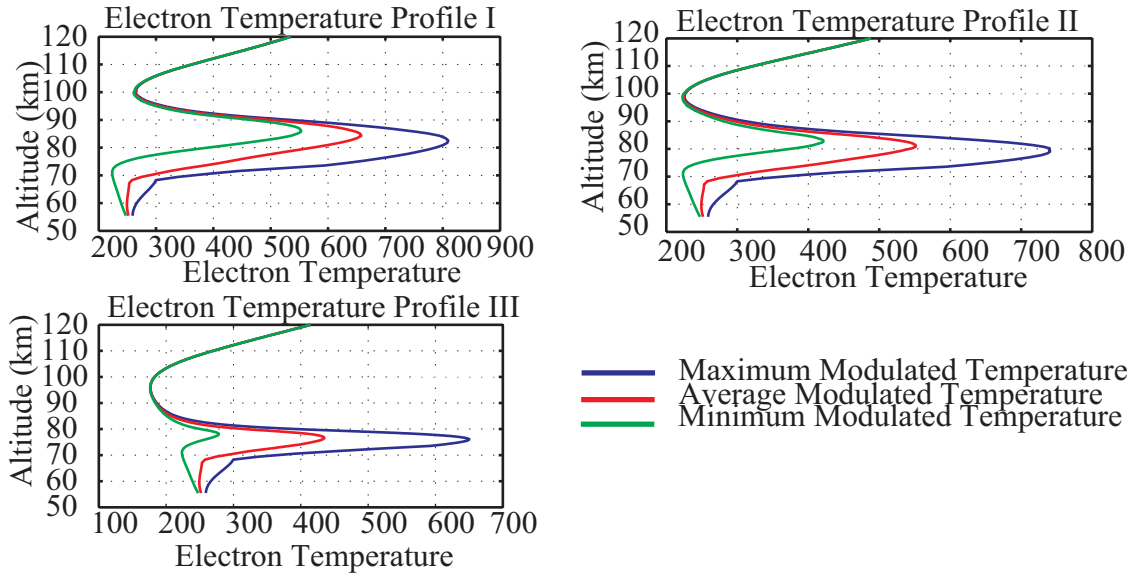
Figure 4.3: Maximum, minimum, and average T_e using Profile I, II, and III.

4.2.2 Conductivity

In Figure 4.4, N-S slices of the modulated Pedersen and Hall conductivities above the HAARP HF array are shown. The E-W slices look very similar and are not worth displaying.

The Hall conductivity modulation is both stronger and at a slightly lower altitude when compared with the Pedersen modulation for all three ambient profiles. The previous modeling work of *Carroll and Ferraro* [1990] shows that ground VLF measurement of radiating ionospheric currents is a strong function of source altitude. The higher in altitude the current exists, the worse is the coupling of its radiated fields into the Earth-ionosphere waveguide. This result is consistent with previous work that indicates the Hall currents statistically dominate ground based VLF radiation.

Both the Hall and the Pedersen conductivities decrease in altitude and increase in strength, from Profile I to Profile II, and then from Profile II to Profile III. For Profile I, the maximum Pedersen height is 92 km, the maximum Hall height is 88 km, and the maximum Parallel height is at 99 km. For Profile II, the maximum Pedersen height is 84 km, the maximum Hall height is 82 km, and the maximum Parallel height is at 95 km. For Profile III, the maximum Pedersen height is 80 km, the maximum
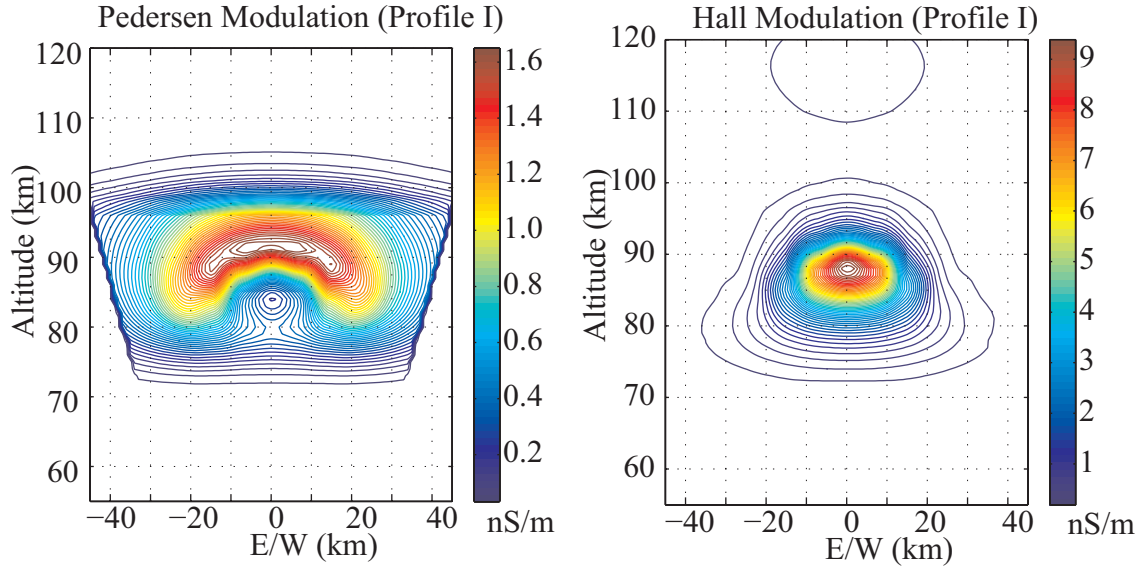
Figure 4.4: Modulated Pedersen and Hall conductivities for Profile I.

Hall height is 78 km, and the maximum Parallel height is at 85 km.

While the Hall and Pedersen conductivity modulations track each other within a factor of two, the Parallel conductivity is about three orders of magnitude larger. However, because the ambient Parallel conductivity is so much higher than the ambient Hall or Pedersen conductivities, charges can quickly (compared to the modulation cycle time) redistribute themselves in the ionosphere to counteract any vertical component of the ambient electric field.

4.2.3 Primary Modulated Currents

In Figures 4.7 through 4.9, the primary modulated currents are integrated at each altitude slice and displayed as a function of height. At the altitude of maximum integrated total current, a horizontal slice is shown with the directional flow of the currents. The integrated currents are calculated for an assumed horizontal electric field of 15 mV/m. However, the only effect that electric field magnitude has is to scale each trace in exactly the same proportion as the other traces.

For Profile I (Figure 4.7), the integrated Hall current is slightly larger than the
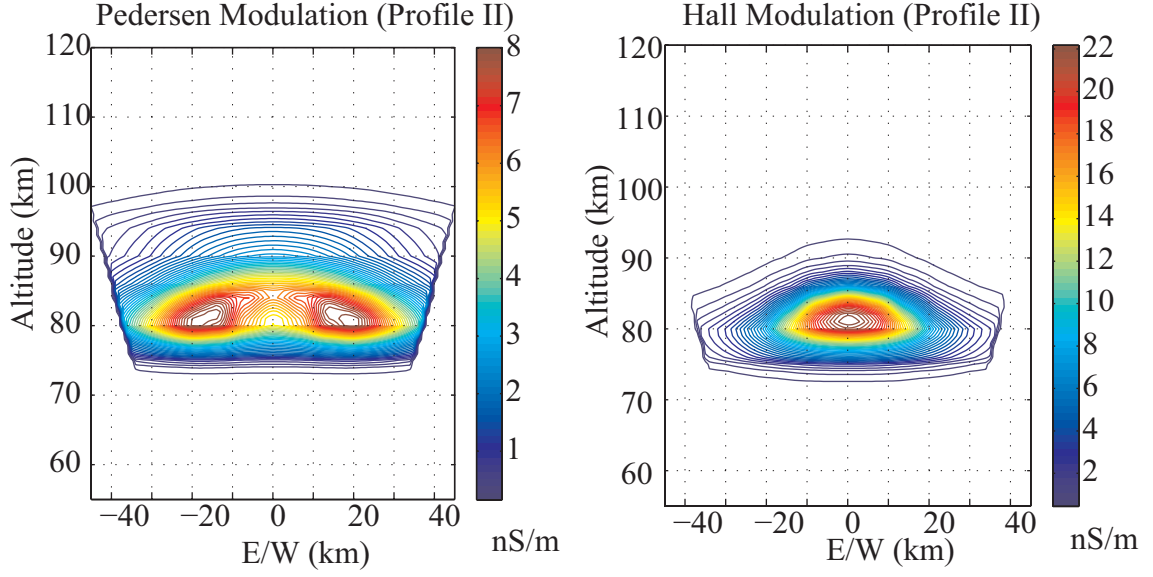
Figure 4.5: Modulated Pedersen and Hall conductivities for Profile II.
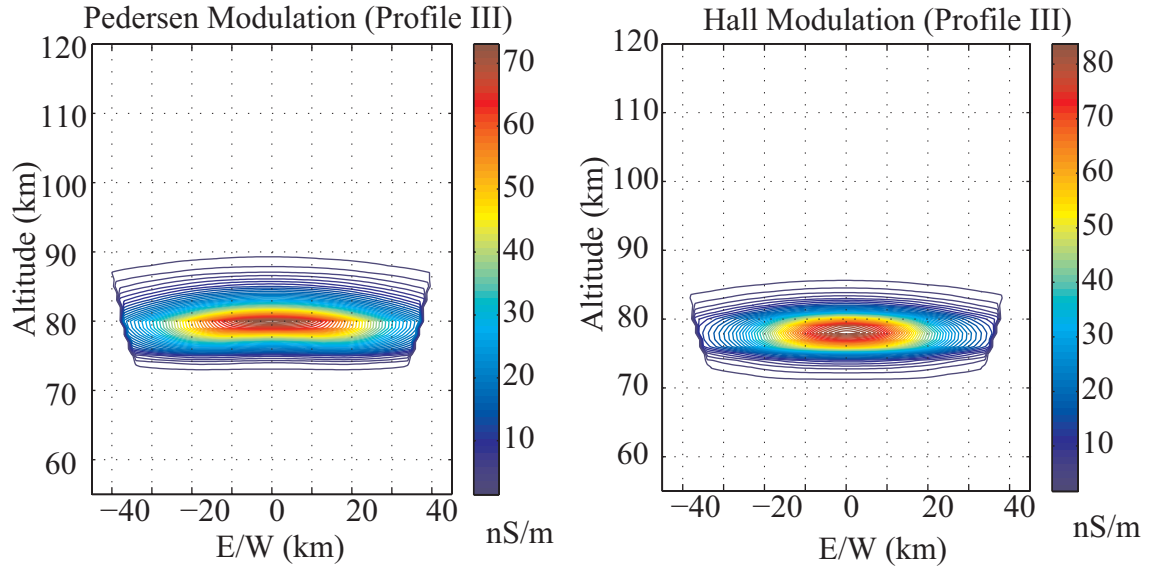
Figure 4.6: Modulated Pedersen and Hall conductivities for Profile III.
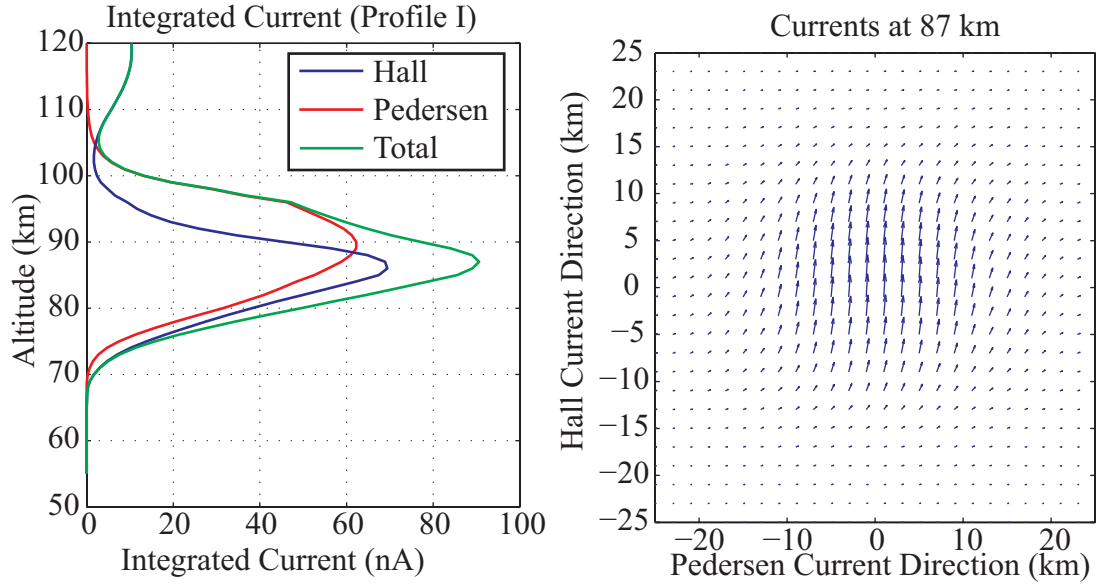
Figure 4.7: Primary currents for Profile I. The left plane shows the current integrated at each altitude slice. The right pane shows the horizontal current structure at the maximum integrated height.
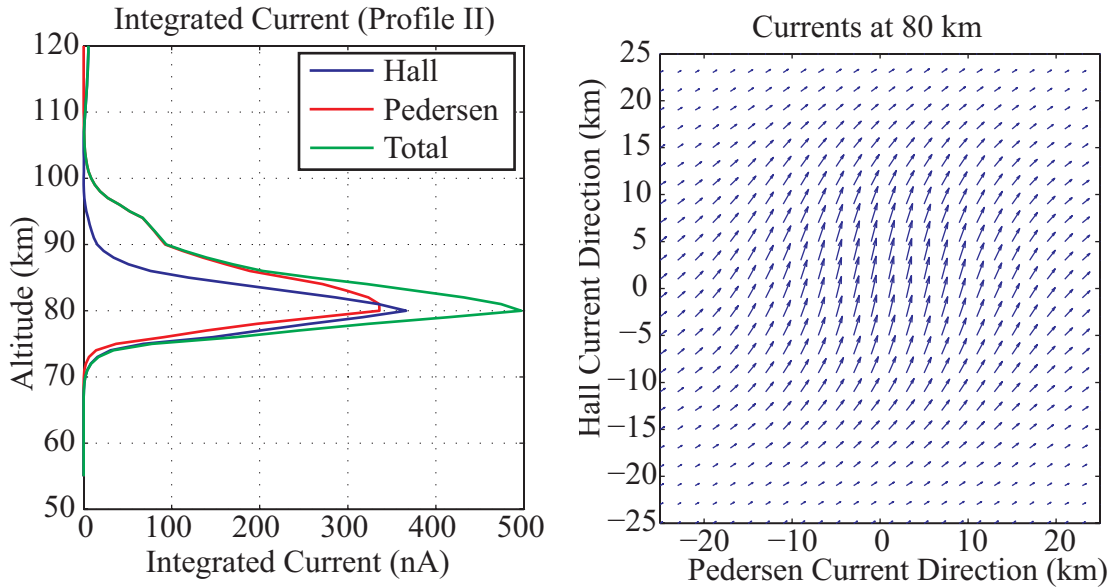
Figure 4.8: Primary currents for Profile II. The left plane shows the current integrated at each altitude slice. The right pane shows the horizontal current structure at the maximum integrated height.
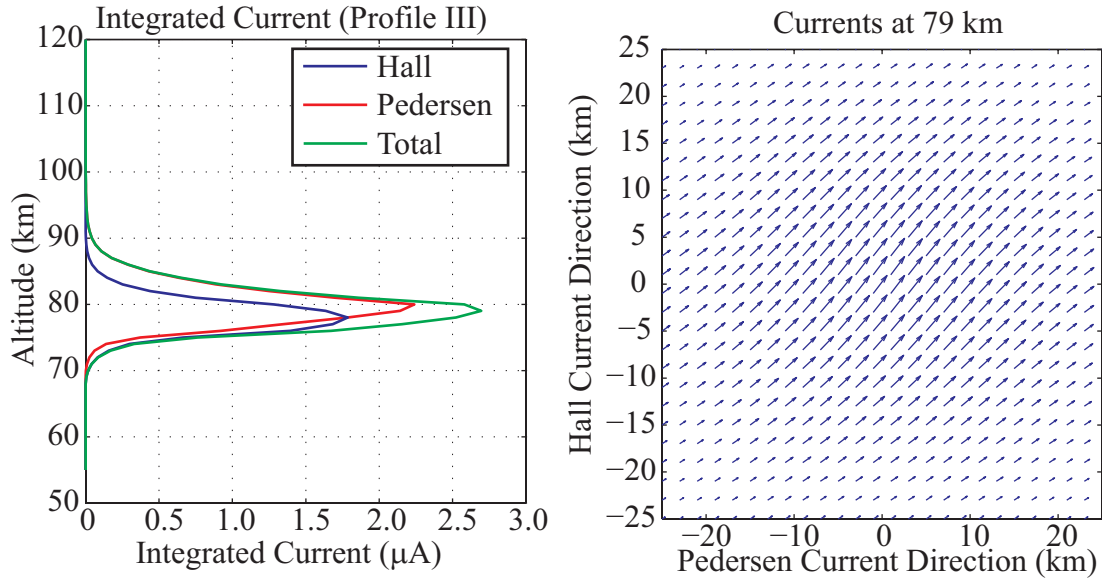
Figure 4.9: Primary currents for Profile III. The left plane shows the current integrated at each altitude slice. The right pane shows the horizontal current structure at the maximum integrated height.

integrated Pedersen current. However, the Pedersen current peaks at a higher altitude and is also present over a much broader altitude range when compared to the Hall current. From the current slice on the right of the figure, it can be seen that the center is dominated by the Hall current while the edges are dominated by the Pedersen current. This result is consistent with the conductivity modulation map (Figure 4.4) where it is apparent that the Hall spot size is smaller than the Pedersen spot size.

For Profile II (Figure 4.8), the denser electron density profile causes the modulated currents to form at a lower altitude. The integrated Hall and Pedersen currents are nearly identical up to the maximum altitude of interest, but the Pedersen currents fall off less quickly with altitude. From the current slice (right panel), the Hall currents in the center dominate, with the Pedersen currents dominate around the edge.

For Profile III (Figure 4.9), both integrated current peaks have increased over the Profile II run. The peak of the integrated Hall current is a few kilometers below the peak shown using Profile II, with the peak of the integrated Pedersen current remaining roughly constant in altitude. The total integrated current peak altitude

is somewhat lower as a result. Additionally, the current slice reveals that the Hall current and the Pedersen currents are of nearly the same size and neither dominates the current structure.

4.3 FDTD Modeling

In the previous sections, a method to determine the primary source currents generated by HF modulation of the D-region of the ionosphere is explained. In this section, these primary source currents are used as inputs into a full wave coupled electromagnetic plasma FDTD code which computes both the secondary ionospheric conduction currents and the electromagnetic fields received on the ground. The FDTD code used in this dissertation was developed by Timothy Chevalier and is based on the methods presented by *Lee and Kalluri* [1999].

FDTD is nothing more than a method used to solve a system of partial differential equations where time and space are discretized and the number of variables is too large to use standard matrix inversion techniques. Instead, an assumed initial condition is imposed and update equations are used to determine the spatial solution at the next time step. The process is repeated until the solution is known to the desired length of time.

In this section, a brief description of the equations that the FDTD code solves is given. For more general information relating to FDTD, see the excellent reference *Taflove and Hagness* [2000].

4.3.1 Coupled Equations

The electromagnetic equations that the FDTD code solves are given as

$$\nabla \times \mathbf{H} = \mathbf{J} + \epsilon_0 \frac{d\mathbf{E}}{dt} \tag{4.32}$$

$$\nabla \times \mathbf{E} = -\mu_0 \frac{d\mathbf{H}}{dt} \tag{4.33}$$

$$\frac{d\mathbf{J}}{dt} + \nu \mathbf{J} = \frac{q_e}{m_e} \left(q_e N_e \mathbf{E} + \mathbf{J} \times \mathbf{B} \right) \tag{4.34}$$

where $\mathbf{H}$ is the magnetic field, $\mathbf{E}$ is the electric field, $\mathbf{J}$ represents the total current that flows in the plasma, ν is the collision rate, q_e is the charge on an electron, m_e is the mass of an electron, $\mathbf{B}$ is the magnetic flux, ϵ_0 is the permittivity of free space, and μ_0 is the permeability of free space [*Lee and Kalluri*, 1999].

Equation 4.32 is Ampere's Law, and Equation 4.33 is Faraday's Law. Equation 4.34 is the first two linearized moments of Vlasov's equation, which is a valid truncation under a cold plasma model [*Bittencourt*, 2003, p211]. The equations are solved on a 3-D staggered Lee and Kalluri mesh [*Lee and Kalluri*, 1999].

4.3.2 Perfectly Matched Layers

In solving large FDTD grids, it is important that absorbing boundary conditions are properly employed. These conditions prevent reflections from the artificial boundary conditions imposed by the sudden termination of the solution space from corrupting the eventual solution. One type of absorbing boundary condition is known as a Perfectly Matched Layer (PML) and is a standard tool in numerical electromagnetic work [*Taflove and Hagness*, 2000, p285-286].

The basic idea in a PML implementation is to replace the ∇ operator in Maxwell's equations with

$$\tilde{\nabla} = \hat{\mathbf{x}} \frac{1}{s_x} \frac{\partial}{\partial x} + \hat{\mathbf{y}} \frac{1}{s_y} \frac{\partial}{\partial y} + \hat{\mathbf{z}} \frac{1}{s_z} \frac{\partial}{\partial z} \tag{4.35}$$

where s_x, s_y, and s_z represent stretching variables that attenuate the wave as it propagates in a cardinal direction. The form of the PML operator changes based on

the properties of the propagation material and the frequency of interest. In a weakly ionized plasma, creating a PML that does not become unstable is a complicated task that is too involved to describe in this thesis. For a very good explanation regarding PML operators see *Chevalier* [2006] and *Taflove and Hagness* [2000].

4.4 FDTD Results

Because of the computational challenges in running FDTD code with a large solution space, the San Diego Supercomputer Center's computing resources were utilized. Unfortunately, the amount of computational time dedicated to this process was not sufficient to run simulations using all three ionospheric profiles. Thus, the most dense profile (Profile III) was used to explore the case where the ionospheric plasma has the greatest effect on secondary current formation and on Earth-ionosphere waveguide effects.

Each of the simulations was performed using a 160 by 160 by 172 size grid where each element is a 1 km square box. A 30 cell thick PML layer composes the outermost cells on all faces of the solution space except the ground, which is modeled as a perfect conductor. The reflection coefficient provided by the PML is rather modest at roughly -30 dB, but is sufficient for this application.

4.4.1 Secondary Currents

In this section, the response of the plasma to the initial perturbing set of primary currents is explored. Both the Hall and Pedersen primary currents are input into the FDTD code. The primary currents summed with the secondary currents are displayed in Figure 4.10.

Figure 4.10 shows that the plasma responds to the initial stimulation by developing a set of current sheets that are perpendicular to the magnetic field. These current sheets enforce the continuity equation, preventing charge from accumulating in the plasma while supporting a slowly propagating electromagnetic mode with a k-vector parallel to the Earth's magnetic field.

Figure 4.10: The left panel shows the **x** directed current in a vertical slice through the numerical solution space. The right panel shows the **y** directed current in the orthogonal vertical slice. In this case, East runs along the **x** direction while North runs along the **y** direction.

Figure 4.11 shows the horizontal electric fields that develop in the plasma. The strength of the upwardly directed electromagnetic mode is much greater than the strength of the fields that couple into the Earth-ionosphere waveguide. The mode clearly progresses upward, following the Earth's magnetic field without undergoing much lateral spreading.

In Figure 4.12, the polarization of the electric field is plotted as the upwardly propagating mode reaches higher altitudes. Near the heated region, the electromagnetic mode is nearly linearly polarized. A few kilometers above the heated region, the mode is much more elliptically polarized. Finally, at 117 km, the mode has become a right-hand circularly polarized (RHCP) mode. A RHCP electromagnetic mode with self-supporting perpendicular current sheets traveling along a magnetic field is also known as a whistler wave [*Bittencourt*, 2003, p439-442].
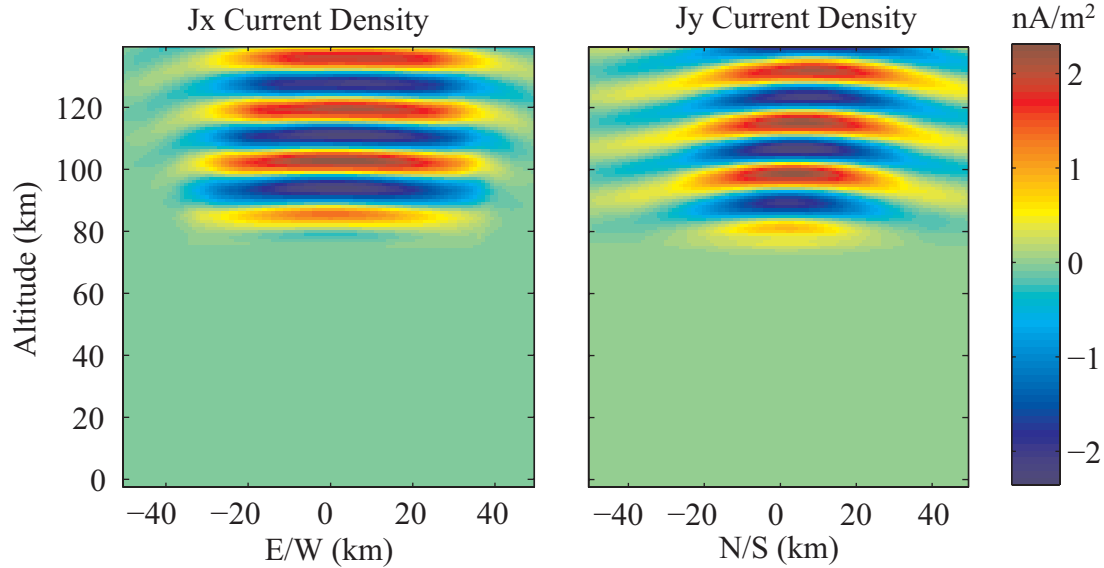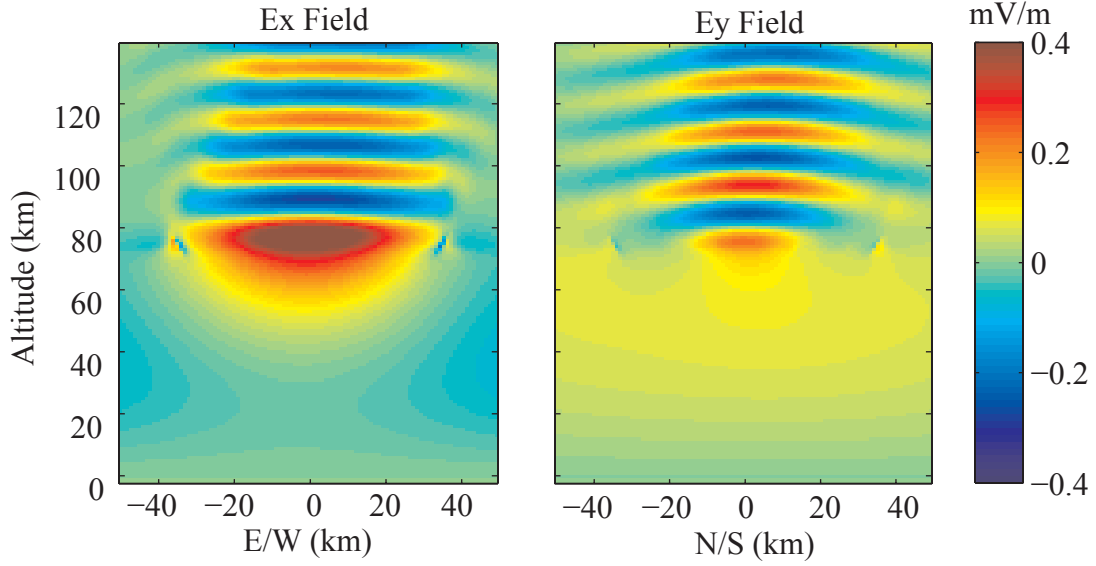
Figure 4.11: The left panel shows the **x** directed electric field in a vertical slice through the numerical solution space. The right panel shows the **y** directed electric field in the orthogonal vertical slice. In this case, East runs along the **x** direction while North runs along the **y** direction.
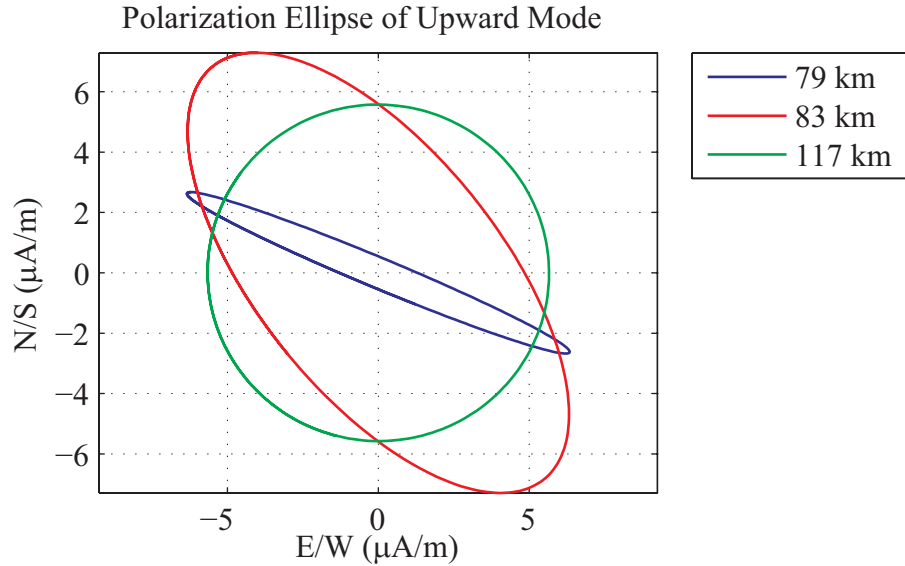
Figure 4.12: Shows the polarization of the electric field of the upward propagating mode at three different altitudes. Near the source height at 79 km, the mode is nearly linearly polarized. At 83 km, the mode has become elliptically polarized. Finally, at 117 km, the mode is nearly circularly polarized.

4.4.2   Wave Propagation

In this section, the ground-based electromagnetic fields are explored. Figure 4.13 shows the amplitude of the two horizontal magnetic components and the vertical electric field on the ground beneath the heated region. The right side of the figure displays the predicted field patterns from the FDTD simulation. The left side of the figure displays the predicted field patterns from a radiating Disk of Current (DOC) propagated to the ground using free space propagation equations (see Appendix C). The DOC is set to roughly match the size of the heated region above the HF heater and is placed at 78 km in altitude, near the altitude of maximum current density (both Pedersen and Hall) for Profile III.

Comparing the FDTD solution to a DOC model may seem odd. However, the FDTD solution cannot map the fields on the ground for more than about 50 km on either side of the heated region. The reason for this is computational; the limited numerical solution space currently implemented requires many hours of supercomputer time and the use of a larger numerical space is impractical. Because the Interferometer elements are spaced by 70 km, a method to compare the model to the data at distant sites is required.

The match between the amplitude of the fields predicted from the FDTD simulation and the DOC is remarkable. The magnetic fields are slightly distorted and asymmetrical in the FDTD solution, but the vertical electric fields are nearly an identical match. Figure 4.13 argues strongly that a DOC approximates the amplitude of the ground based field pattern beneath a ELF/VLF modulated heated region. The model should remain valid until waveguide effects begin to invalidate the free space propagation model.

Figure 4.14 shows the phases of the ground based electromagnetic fields underneath a VLF modulated ionosphere. The left side of the figure is the fields predicted from a DOC, the right side is the FDTD simulation predictions. The two simulations are in good agreement for the B_y and E_z components of phase, but the B_x phase is significantly distorted in the FDTD simulation. This distortion occurs in the direction perpendicular to the radiating current elements and is probably caused by waveguide effects.
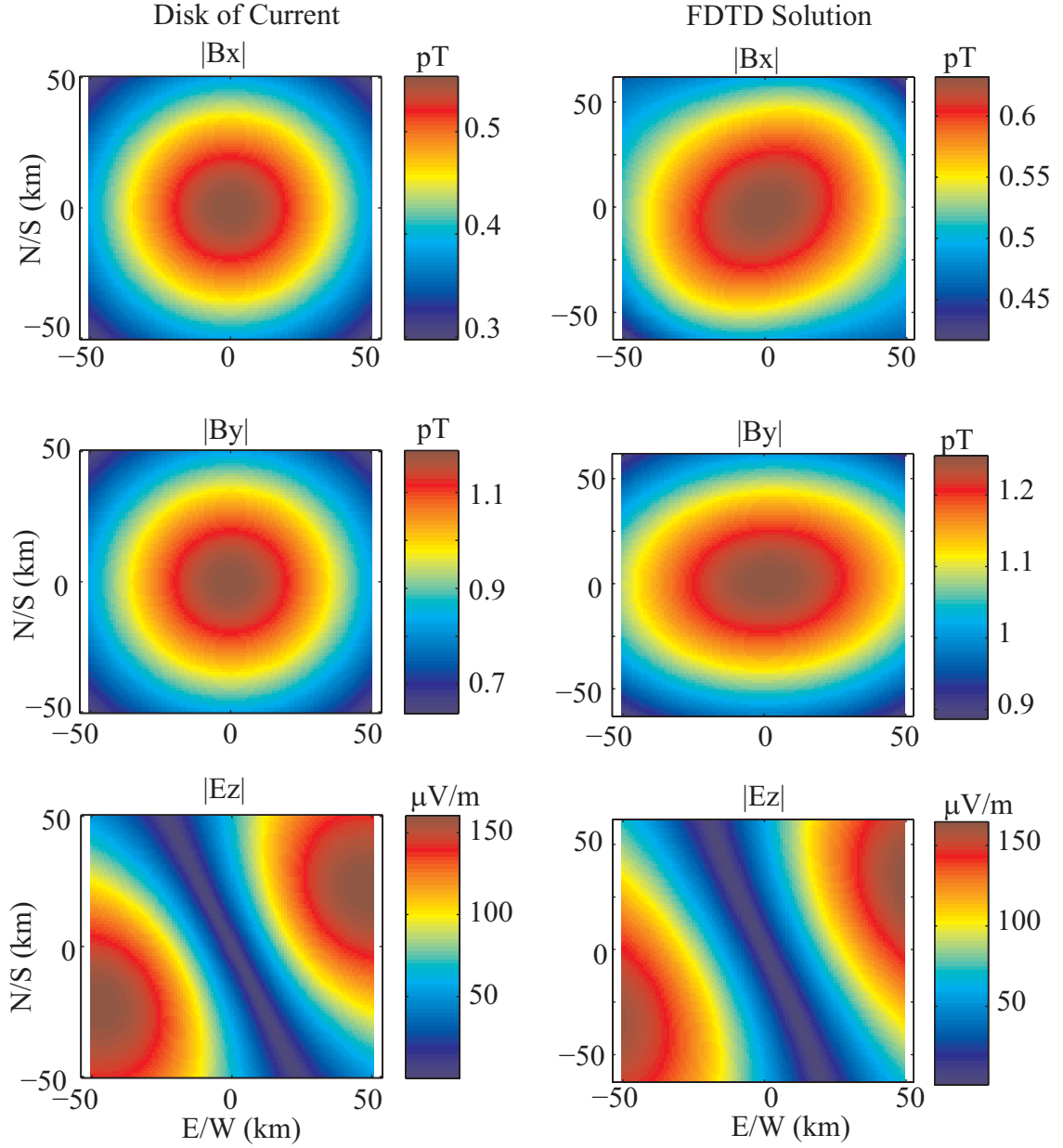
Figure 4.13: Shows the amplitude of the ground electromagnetic fields for the two horizontal magnetic components, and the vertical electric component. The left figures show the predictions from a DOC model, the right figures show the predictions of the FDTD simulation. The match is very close. East is aligned along **x** while North is aligned along **y**.
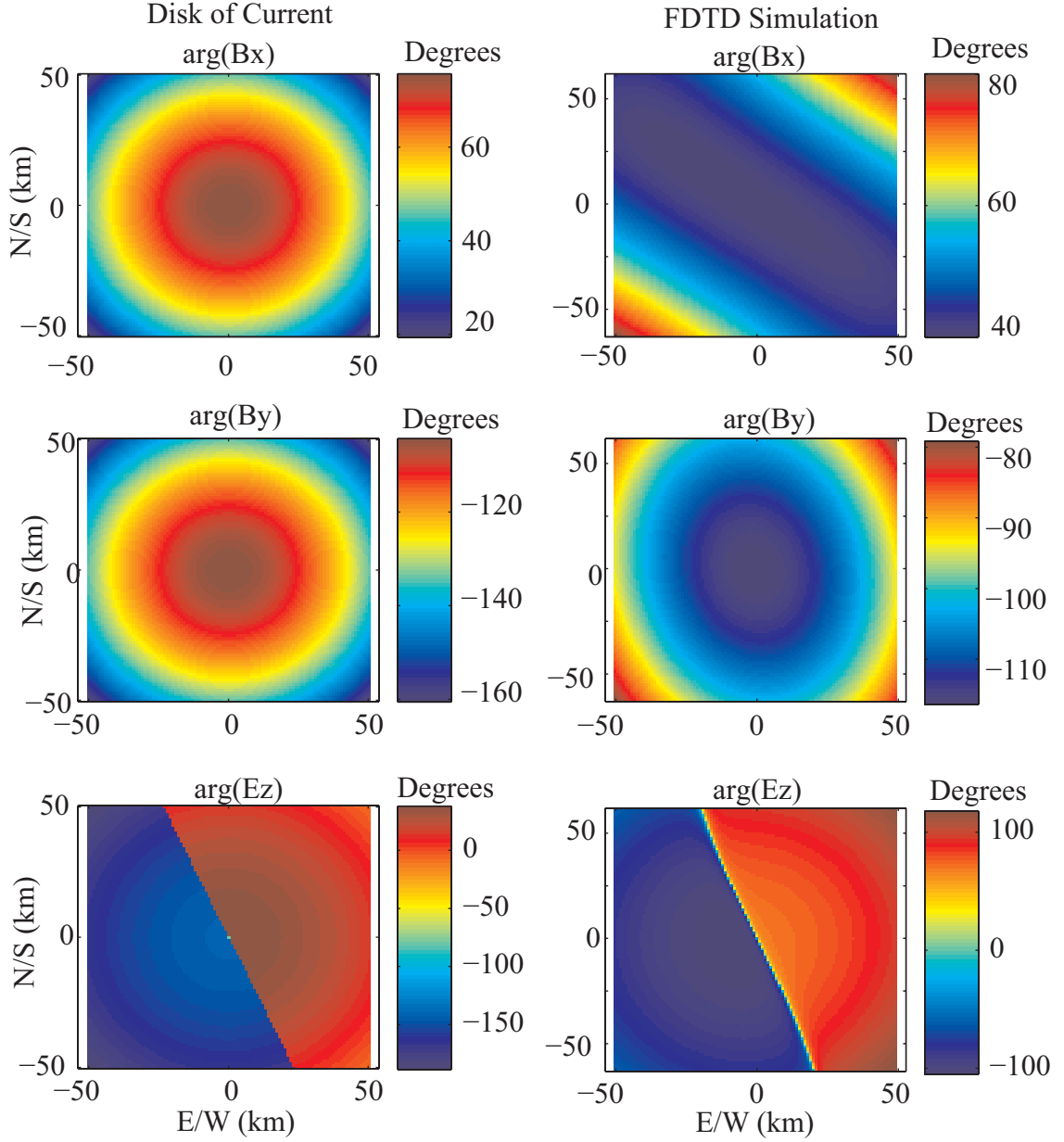
Figure 4.14: Shows the phase of the ground electromagnetic fields for the two horizontal magnetic components, and the vertical electric component. The left figures show the predictions from a DOC model, the right figures show the predictions of the FDTD simulation. East is aligned along **x** while North is aligned along **y**.

4.5   Forward Modeling Summary

In this chapter, it is shown that for a given ambient density profile it is a time consuming, but straightforward, process to model the modulation of the conductivity tensor in the ionosphere. The modulation of this conductivity tensor results in a set of modulated currents. These modulated currents give rise to complicated field formations in the plasma medium, including the formation of an upwardly directed whistler wave. However, these complicated effects are not seen on the ground and the ground based fields are largely indistinguishable from those generated from a small disk of radiating current.

In the next chapter, a simple propagation model is used to compare the predicted ground based field patterns to the data recorded during the Interferometer Campaign.

Chapter 5

Comparing Model Results to Data

In the previous chapter, it is shown that a simple disk of current model predicts similar ground based electromagnetic fields when compared with the predictions from a full wave plasma interaction FDTD code. In this chapter, the DOC model is put to the test and is compared with data collected at the Interferometer sites during the Interferometer Campaign. This chapter begins by describing a method of aligning the disk of current model to the data by estimating the current moment direction of modulated ionospheric currents using ground based measurements. Finally, the predictions of the model are compared against recorded data.

5.1 Aligning the Current Moment

In the process of examining the available data and comparing it to model results, it became necessary to develop a method to determine the direction of the current moment[1]. In this section, two consistent method are presented. The first method uses the vertical component of the electric field. Most past modulated HF heating experiments have concentrated on recording the magnetic fields and have ignored the electric components, which is the probable reason why this technique has not been explored earlier. The second technique is a method of using the magnetic components to determine the current moment direction. It is similar to the method presented in

---

[1]To within a 180° ambiguity
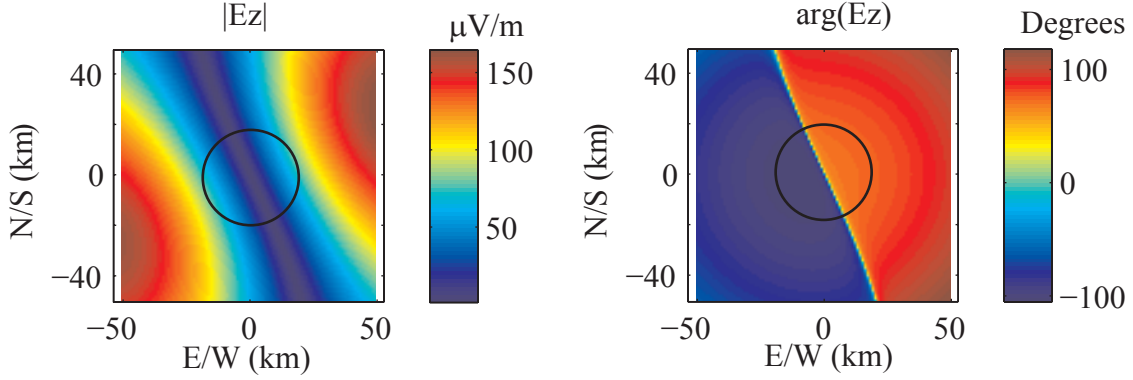
Figure 5.1: Vertical electric field pattern predicted using FDTD simulation. The left plot shows the magnitude of the field pattern, the right plot shows the angle of the field pattern. Note the 180° change in phase along the minimum line. The circle shows the path that a receiver makes through this pattern if the HAARP beam is held at constant elevation and rotated in azimuth.

Rietveld et al. [1983] which was used to compare STARE results to VLF measurements. It should be noted that these methods only work when the electrojet remains approximately constant over the 20 minute duration of each experimental run.

5.1.1   Electric Field Minimum

In Figure 5.1, the FDTD simulation predicted amplitude and phase of the vertical electric field pattern is displayed at ground level. This pattern exhibits a distinct minimum that coincides with a 180° change in phase. Both the minimum and the 180° change in phase are exploited to orient the model to the data.

Using this knowledge of the ground based vertical electric field pattern, an experiment is devised to align the pattern and the data. For this experiment, the HAARP beam is held constant in elevation while rotated 360° in azimuth. The receiver collocated with the HAARP transmitter records the data as the beam rotates. The effect of the rotation is to allow the single centrally located receiver to map the vertical electric field pattern along a circle as shown in Figure 5.1. When looking at the data, the minimum vertical electric field and associated 180° phase change are readily apparent. The model can then be rotated to match the orientation of the data.
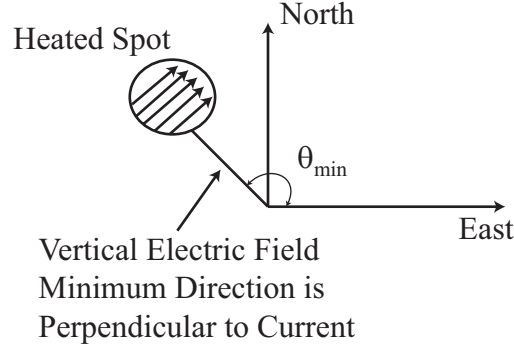
Figure 5.2: Shows the heated spot being rotated around the vertical axis. When the HAARP collocated receiver detects a minimum in the electric field measurement, the currents are oscillating perpendicular to the receiver.

In Chapter 4, it was shown that the magnitude of the vertical electric field pattern matches that of a DOC placed at the height of HF heating. The direction of the current elements in this model are perpendicular to the minimum in the electric field pattern. By marking the minimum of the vertical electric field, the approximate direction of the oscillating currents can be deduced as shown in Figure 5.2.

The beauty of this technique is that the oscillating current direction, to within a 180° ambiguity, can be determined from a completely uncalibrated electric field measurement! All that is needed is millisecond level timing accuracy between the transmitter and the receiver, something that is easily achievable using well known circuit techniques.

5.1.2 Magnetic Field Integration

Using the magnetic field components from the receiver collocated with HAARP, the current direction can be determined using a second method. Examining the ground based magnetic field components due to a dipole source in Appendix C, and noting that the vertical currents are very small, the following approximation can be made:

$$\frac{J_y}{J_x} \simeq \frac{\int B_x d\phi}{\int B_y d\phi} \tag{5.1}$$

This approximation works at the HAARP collocated receiver because all of the R terms in the radiation equations cancel out when using a data set that only includes constant elevation beam angles. The orientations given by the magnetic field method are consistent to those generated by the electric field method.

Because this alignment method is sensitive to antenna orientation and calibration, it is not used to orient data with the models. However, it is reassuring that both methods give consistent results.

5.2   Comparing Model Predictions to Data

In this section, two experimental data sets are presented and compared against the DOC model. The majority of the data is in close agreement to the model and where large differences are present, an attempt is made to reconcile the model results with the data.

It should be noted that many of the idealized assumptions used in the model do not hold for real data. The ionosphere is a complex, time varying system that can grossly change properties over the course of a few minutes. Additionally, the ambient density profiles and the direction and strength of the electrojet are only approximately known. In short, exact agreement cannot be attained using even sophisticated methods modeling single receiver locations. Thus, it should come as no surprise that the simple model presented here does not exhibit perfect agreement when comparing many independent receiver locations.

5.2.1   Comparison Set One

In Figure 5.3, data is compared with the predictions of the DOC model. The elevation of the HF beam is held constant at 20° off vertical. The horizontal axis shows the azimuth that the HAARP HF beam makes with True East being 0°, and True North being 90°. The vertical axis of the top plot shows the field strength of the three recorded components, with E_z being scaled by $1/c$ to bring it into the same numerical value range as the magnetic components. The model values are all scaled by a single

Figure 5.3: Comparison between data recorded at HRP and the DOC model predictions. Solid lines represent data, dashed lines are the model predictions. Red is B_x, blue is B_y, and green is E_z/c. Data taken on April 9, 2003 at 0600 UTC.

value to account for the uncertainty in the electrojet strength. The bottom plot shows the phase of the three components, after a single phase shift has been applied to all three components. The relative strength and phase of the model predictions are all preserved.

The model is aligned to the data using the E_z minimum point, which occurs at $114°$ in this dataset. Comparing this minimum to the E_z ground pattern from the DOC model implies that the current moment is aligned along a line that is approximately $24°$ North of East.

The shape of the E_z pattern in both amplitude and phase shows very good agreement between model and data. Similarly, the phase and amplitudes of the magnetic components exhibit a very good match. Now that the model is aligned to the data and shows good agreement, the model is ready to be compared with distant sites.

In Figure 5.4, the DOC model is compared against the four other sites that were operating at the same time that the data in Figure 5.3 was collected. The model predictions are scaled by an additional amount to better compare the shape of the

data and the model. The additional scale values are listed in the figures.

The top left plots of Figure 5.4 show a comparison between the data and the model at Black Lake (BLK), at a ground distance of 142 km from HAARP. There is very good agreement between the amplitude and phase of the predicted B_x component and the data. The relative magnitude of E_z shows good agreement, but the model predicts several phase changes that are not represented in the data. Also, there is a null in the B_y data that is not seen in the model predictions. There are two possible explanations for these discrepancies. First, BLK is about 140 km from the HAARP heater and waveguide effects are beginning to dominate the propagation path. In this context, it should be restated that the DOC calculations assume free space propagation and do not account for waveguide effects. Second, BLK is located perpendicular to the direction of the predicted current oscillations. Recalling the ground based FDTD solution presented in Chapter 4, in the direction orthogonal to the oscillating currents there is a great deal of difference between the phase predicted by FDTD and the phase predicted for the current disk model.

The top right plots of Figure 5.4 compare the data and the model at Paxon (PAX), at a ground distance of 73 km from HAARP . Both the amplitude and phase of B_x and B_y show strong agreement between model and data. The model predicts the relative strength of E_z fairly accurately, but predicts a 180° phase change both earlier and sharper than the one shown in data.

The bottom left plots compare the data and the model at Slana (SLA), at a ground distance of 71 km from HAARP. All three components match for both amplitude and phase.

The bottom right plots compare the data and the model at Tok (TOK), at a ground distance of 140 km from HAARP. All three amplitude components match reasonably well, and the B_x and E_z phases match very well. The B_y phase is a bit of a mismatch, most likely caused by the fact that TOK is also 140 km from HAARP and waveguide effects are starting to effect the propagation.

Figure 5.4: Comparison between data recorded at various sites and the disk of current model predictions. Solid lines represent data, dashed lines are the model predictions. Red is B_x, blue is B_y, and green is E_z/c. Data taken on April 9, 2003 at 0600 UTC.
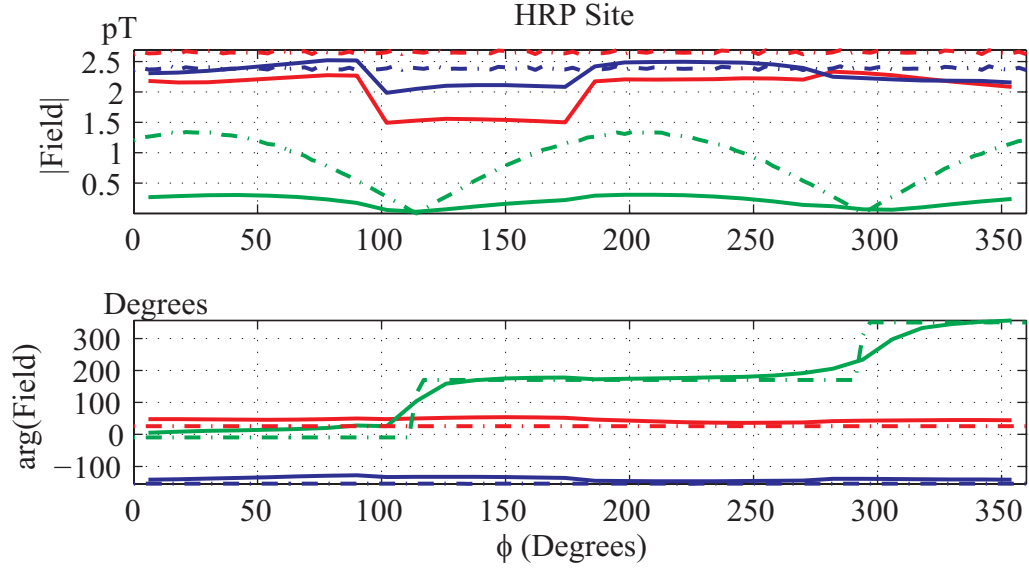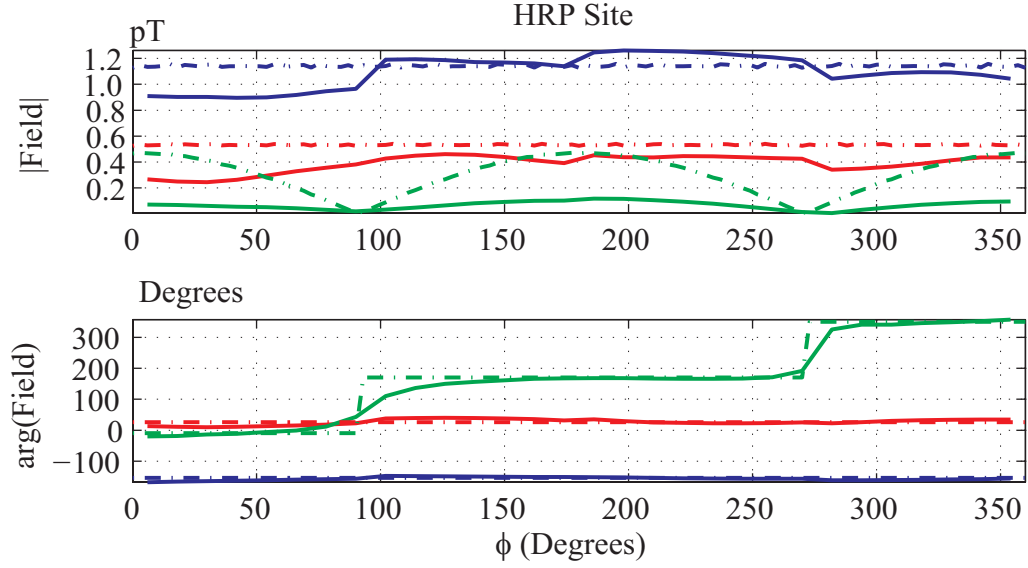
Figure 5.5: Comparison between data recorded at HRP and the disk of current model predictions. Solid lines represent data, dashed lines are the model predictions. Red is B_x, blue is B_y, and green is E_z/c. Data taken on April 9, 2003 at 0800 UTC.

5.2.2 Comparison Set Two

In Figure 5.5, data collected at HRP at a different time is again compared with the DOC model after alignment. In this case, the E_z minimum occurs at $1°$ which corresponds to currents that oscillate $1°$ North of East. As in the previous section, the agreement in both amplitude and phase at HRP is very good.

In Figure 5.6, the DOC model is compared against the four other sites that were operating at the same time that the data in Figure 5.5 was collected.

The top left plots show a comparison between the model and data at BLK. Again, it is found that the amplitude and phase of the predicted B_x is a good match to data. The relative strength of the predicted E_z is a fair match to data, and the phase of the predicted E_z matches the shape of the data. The model overestimates the B_y amplitude, but does a reasonable job matching the phase.

The top right plots compare the data and the model at PAX. Both the amplitude and phase of B_x and B_y show strong agreement between model and data. The amplitude of E_z shows good agreement, but the phase of E_z exhibits changes that are

not seen in the data.

The bottom left plots compare the data and the model at SLA. The model and the data show strong agreement in amplitude, with the model predicting a slightly larger field strength for E_z. The phases of all components are a strong match between the model and data.

The bottom right plots compare the data and the model at TOK. The model and the data show strong agreement in amplitude, with the model predicting a slightly larger field strength for E_z. The phases of B_x and E_z show good agreement between model and data, with B_y phase once again not matching well, probably due to the large propagation path.

5.3   Summary of Model and Data Comparisons

In this chapter, two methods of determination of the net current moment direction from radiating ionospheric dipoles are presented. Because the E_z field pattern is not sensitive to antenna orientation errors or calibration mismatch, it is used to orient the recorded data to the DOC model.

Using two sets of data, the DOC model is compared against recorded data and is shown to be in substantial agreement. The disagreement between model and data usually occurs when the recording station is at a significant distance from the HAARP HF array, or when the recording site is located in a direction perpendicular to the predicted current direction. Both of these effects are expected because the Earth-ionosphere waveguide is not taken into account in the DOC model, and the FDTD code predicts some asymmetry in the magnetic field patterns perpendicular to the direction of the current oscillation.

In the next chapter, a summary of the various contributions of this thesis are given and suggestions for future work are offered. Finally, some reflections are on how this experiment could have been improved are given.
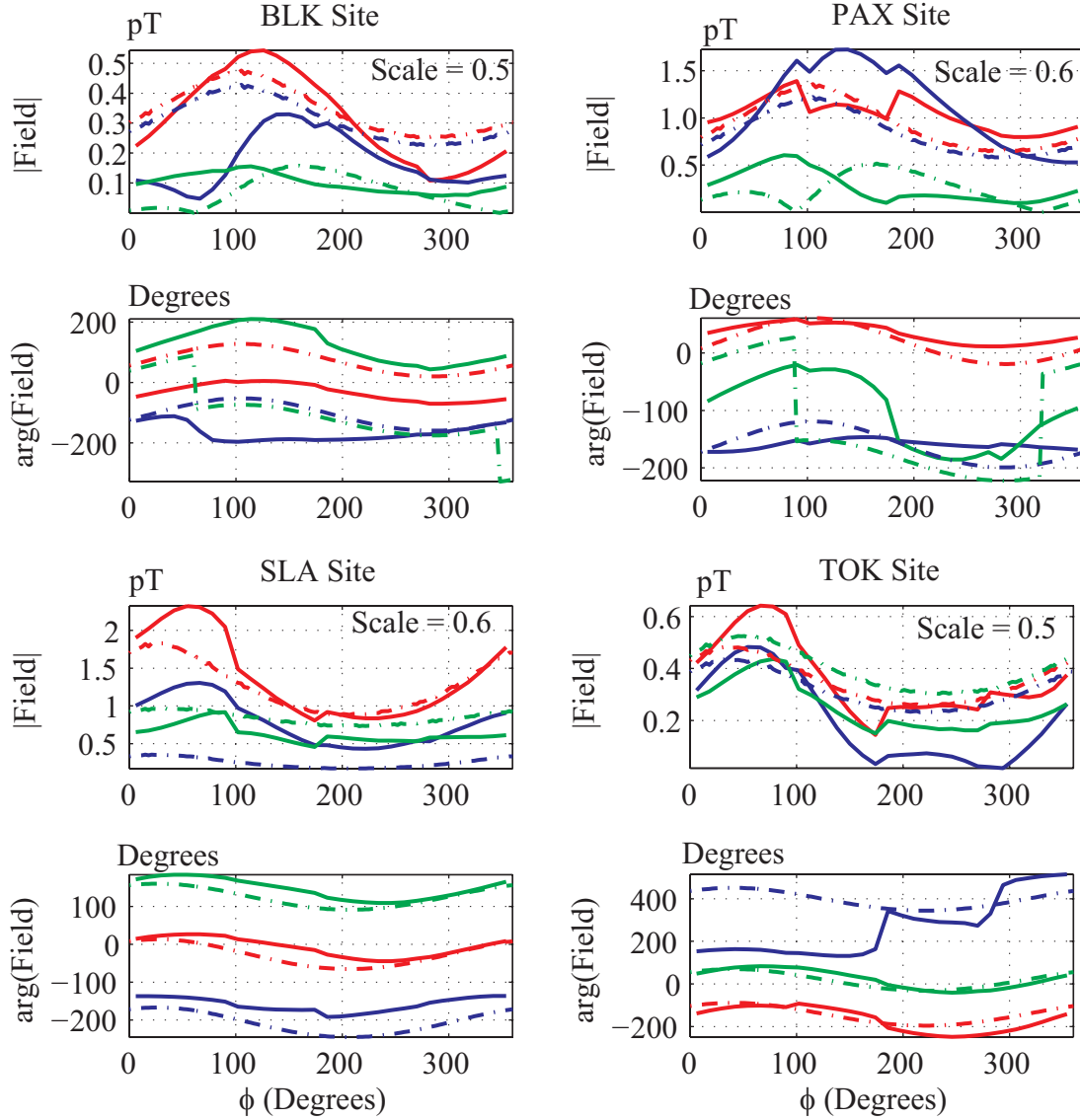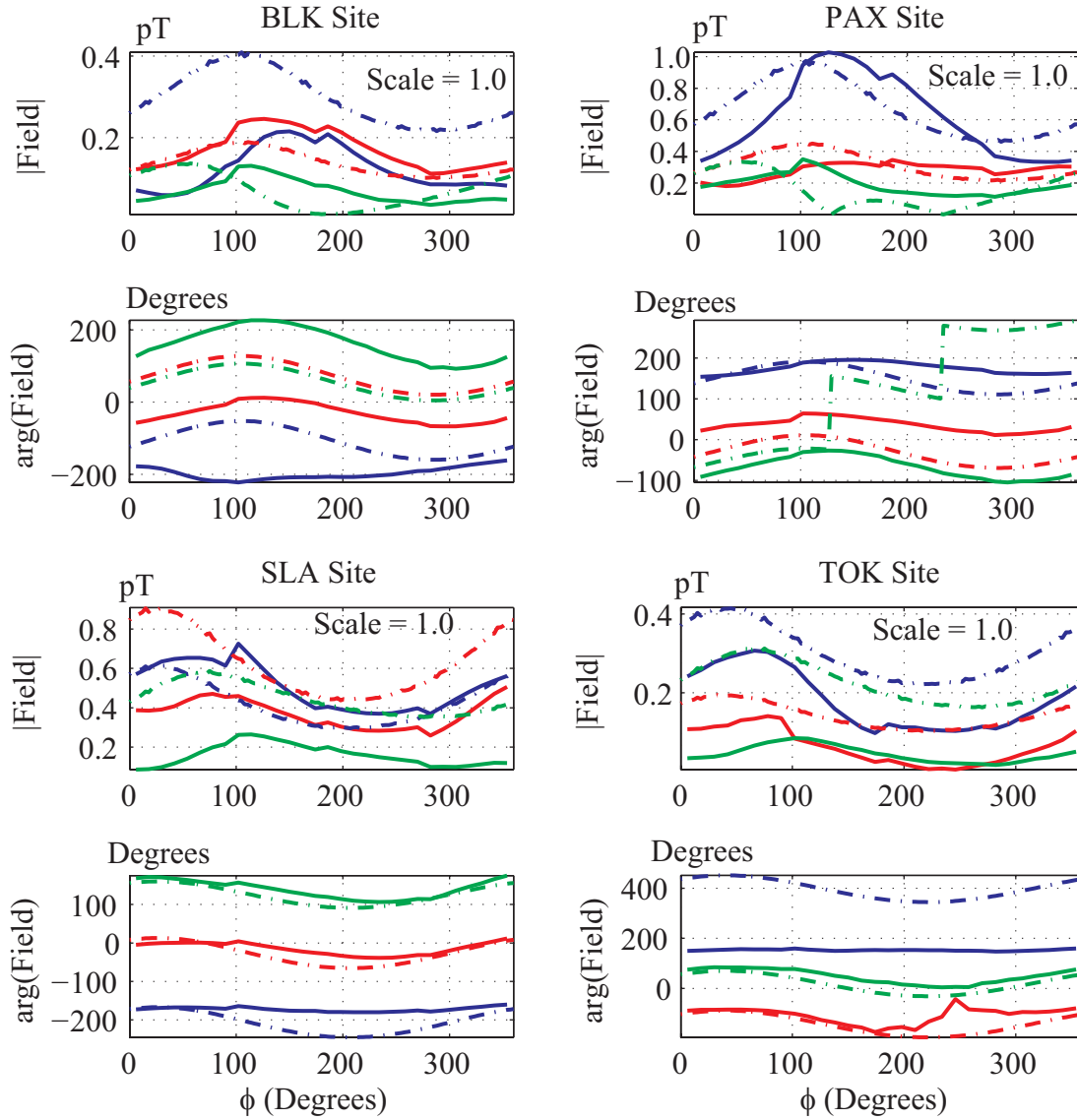
Figure 5.6: Comparison between data recorded at various sites and the DOC model predictions. Solid lines represent data, dashed lines are the model predictions. Red is B_x, blue is B_y, and green is E_z/c. Data taken on April 9, 2003 at 0800 UTC.

Chapter 6

Summary and Future Work

In the previous chapters, the Interferometer Unit and the associated Interferometer Campaign are introduced and thoroughly discussed. Methods of directly inverting the collected VLF data quickly give way to using forward modeling techniques to estimate the spatial structure of the currents above a modulating HF transmitter. These models are compared against VLF data and show substantial agreement.

The purpose of this chapter is to summarize the prior results and highlight the most pertinent contributions. A few additional experiments are proposed that could further refine the understanding of the HF to VLF conversion process. Finally, some reflections about the Interferometer experiment are offered.

6.1   Summary of Results and Contributions

In this dissertation, a new battery powered, time-synchronized device for measuring VLF radiation is presented. Nine of these devices were successfully deployed into the Alaskan wilderness on a campaign in 2003 designed to image the spatial structure of ionospheric currents produced during HF modulation. This campaign produced a vast quantity of data, which was organized, cataloged, and analyzed during the last few years at Stanford University.

In the process of trying to invert VLF data to infer ionospheric currents, a method of using L_1 Norm Minimization while borrowing regularization techniques from least

squares was developed. This method produces an inversion technique that greatly reduces the errors in inverting some electromagnetic matrices when compared to traditional techniques. While powerful, it is shown that this technique is still unsuitable to invert the ionospheric current system when noise and systematic errors are included in the analysis. However, this technique may prove useful in other systems where the condition number of the matrices involved is not as large as is the case in the ionospheric current inversion.

Once direct inversion methods were abandoned, forward modeling techniques were borrowed and developed. These modeling techniques start with a modulated HF heating model, which outputs the variation in conductivity given a beam pattern and an ionospheric profile. Assuming an ambient electric field strength, this conductivity variation is transformed into primary modulated currents. FDTD results are used to determine how these source currents effect the flow of charge in the plasma and how the radiation pattern differers from the radiation pattern of a similar set of current located in frees pace.

The FDTD codes justifies the use of a simple DOC model to represent the currents, and the use of a free space propagation model that ignores the propagation effects of the plasma and the Earth-ionosphere waveguide on the ground located electromagnetic fields. This basic DOC model is compared to recorded VLF data and shows good agreement.

Finally, two methods of determining the dipole moment direction of VLF radiating ionospheric currents are introduced and explained. These methods facilitate accurate comparison between the radiation models and the recorded VLF data.

6.2 Suggestions for Future Research

In this section, some suggestions for future modeling and experiments are presented. Since running the Interferometer Campaign in 2003, the HAARP facility has been upgraded from 960 kW to 3.6 MW of output power. Additionally, the enhanced HF beam is now able to point in multiple directions simultaneously. These two factors allow a number of new and exciting experiment to be conducted and should enhance

the understanding of the HF to VLF conversion process in the next few years.

An important gap in the experimental toolbox is a simple and accurate method to determine the electron density as a function of altitude in the D-region of the ionosphere at nighttime, when the density values are very low. As it stands, HF heating models are imprecise methods of predicting the response of the ionosphere, largely because the ambient density profiles are not known. Estimated profiles are generally used, but to model specific experiments, an accurate determination of the specific profiles is necessary.

6.2.1 Ambient Electric Field and VLF Measurements

In *Rietveld et al.* [1983], the ambient electric field in the ionosphere is inferred using the STARE radar system while simultaneous VLF measurements are made during HF modulation of the ionosphere. This experiment should be repeated using the more powerful HAARP array to modulate the ionosphere, rotating the beam and holding azimuth constant. A set of radars able to track the ion drifts in the ionosphere would be a necessary addition for this experiment to be feasible.

The techniques presented in Chapter 5 can be used to determine the dipole moment direction, and the angle this makes with respect to the deduced electric field should be the ratio of the Hall to Pedersen currents. The purpose of this experiment is to determine if the ratio of the Hall to Pedersen currents suggests optimal ionospheric conditions to produce VLF radiation by modulating an HF beam.

6.2.2 Two-Hop and Dipole Moment Direction

In a variation of the above experiment, the dipole moment direction can be measured and compared to the ambient electric field direction between attempts to induced two-hop magnetospheric reflections [*Inan et al.*, 2004]. The magnetospheric reflections can be measured both at HAARP and the conjugate point using the Stanford developed Buoy. The purpose of this experiment would be to see if there is any correlation between the ratio of the Hall to Pedersen currents and the ability of HAARP to generate VLF radiation that magnetospherically reflects. This experiment could
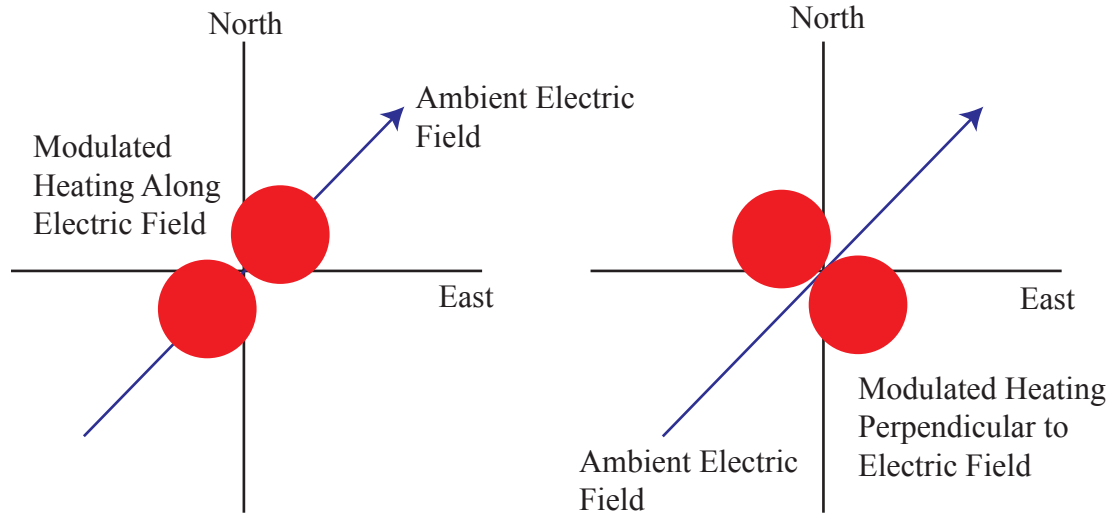
Figure 6.1: Suggested multi-beam experiment. The left panel shows modulated heating along the ambient electric field direction. The right panel shows modulated heating perpendicular to the ambient electric field.

help determine what ionospheric conditions are optimal to perform radiation belt remediation.

6.2.3   Multi-beam Experiment

As a prerequisite to this experiment, the direction of the ambient electric field should be deduced. The HAARP beam should be broken into multiple beams which are first aligned along the deduced ambient electric field, then perpendicular to the ambient electric field (see Figure 6.1). Each beam should be modulated at a frequency close to 2 kHz. The purpose of this experiment is to see if an elongation of the antenna pattern can increase the HF to VLF conversion efficiency.

6.3   Campaign Reflections

In retrospect, the Stanford Interferometer Campaign was an attempt to get too much information at once from the ionosphere. Instead of approaching the problem with

an intent to solve the entire system, a better approach would include many small experiments designed to each tease a small piece of information from the radiating system.

The fact that the receivers used for the Interferometer Campaign were only assembled for the duration of the campaign posed a significant problem. Once the sites were dismantled, it became impossible to reconstruct exact antenna orientations and system configurations. For experiments that require very sensitive measurements, the recordings sites need to be semi-permanent with plenty of time to work through various issues before and after campaign operation.

Finally, the computer simulations largely showed that interesting plasma effects are not seen on the ground, but instead generate waves that propagate into the magnetosphere. This result shows that even with perfect receivers, the full spatial distribution of currents may not be directly measurable with ground located receivers.

Appendix A

Interferometer Schematics

This appendix is to catalog the schematic files for the Interferometer Unit. All the schematic work was performed in Orcad Capture version 10.5. All of the layout work was performed in Orcad Layout version 10.5. The layout files are not presented as they are multi layered and difficult to interpret outside of the development tool. A photograph of each board is presented.
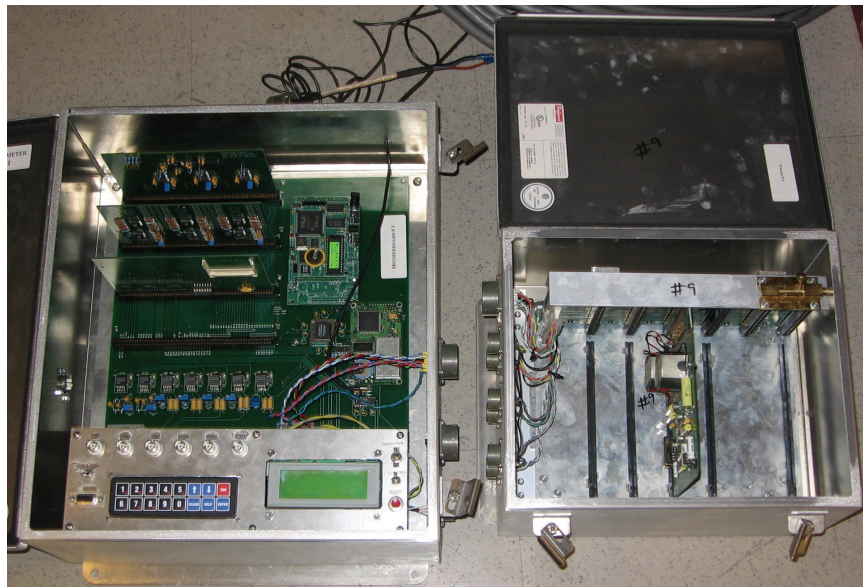
Figure A.1: Receiver and Preamplifier
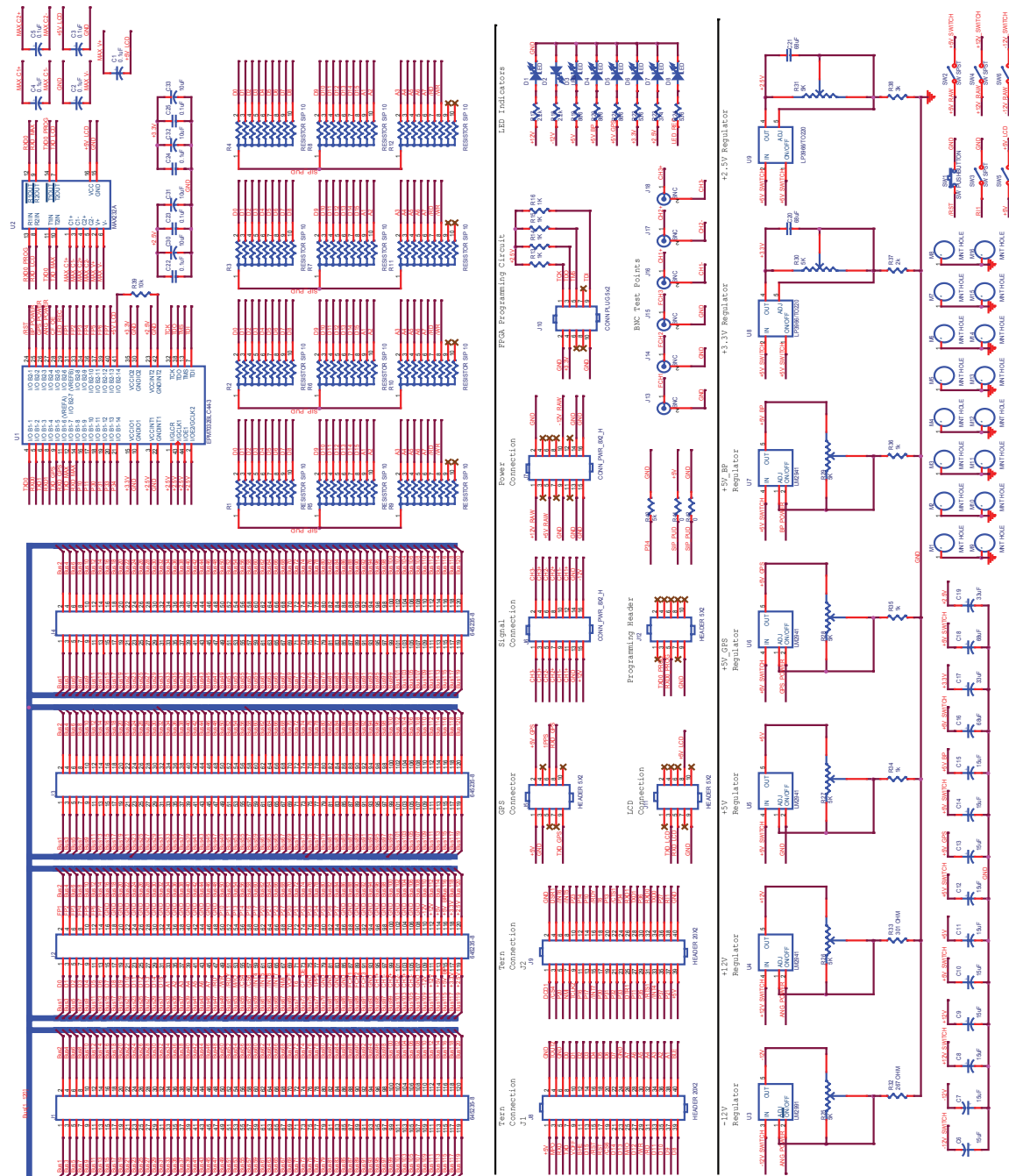
Figure A.2: Receiver Motherboard Schematic
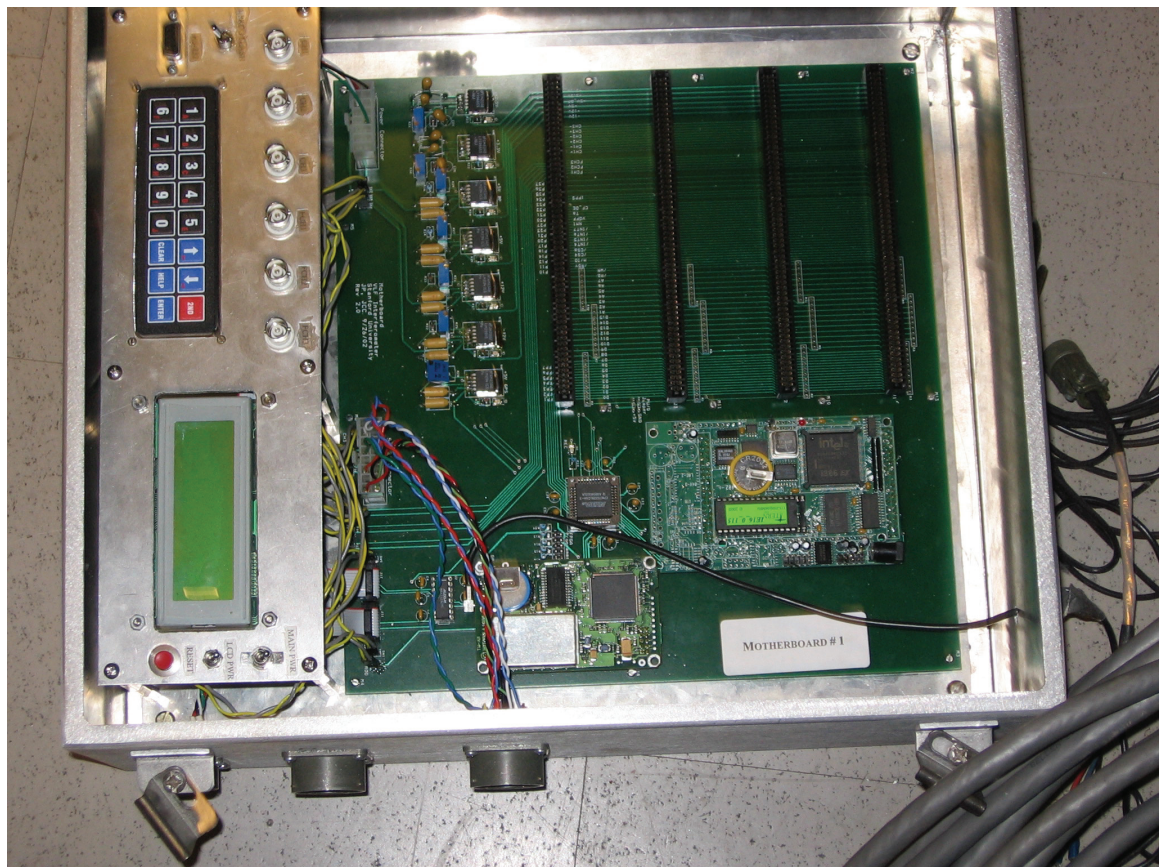
Figure A.3: Motherboard Photograph
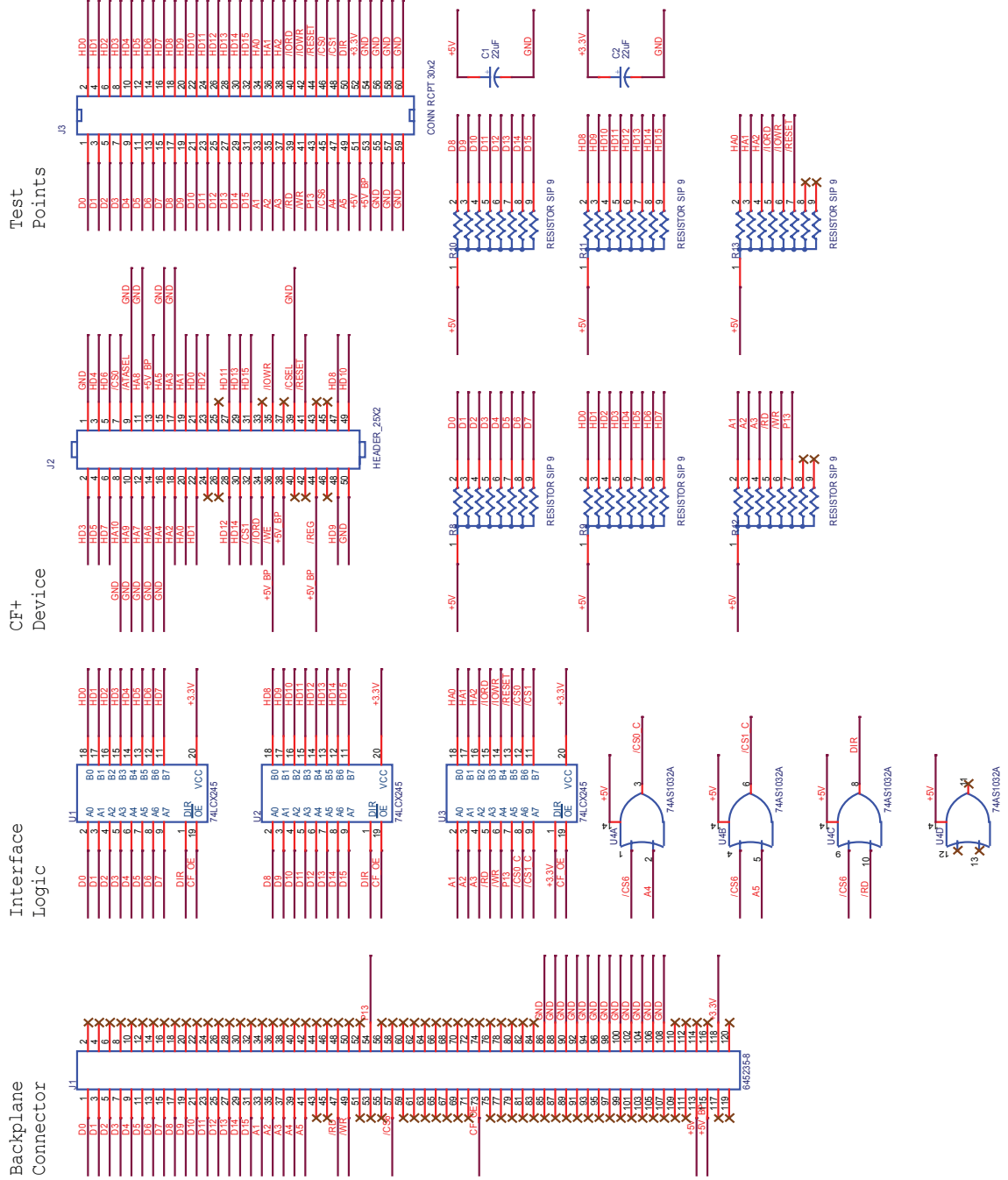
Figure A.4: CompactFlash Card Schematic
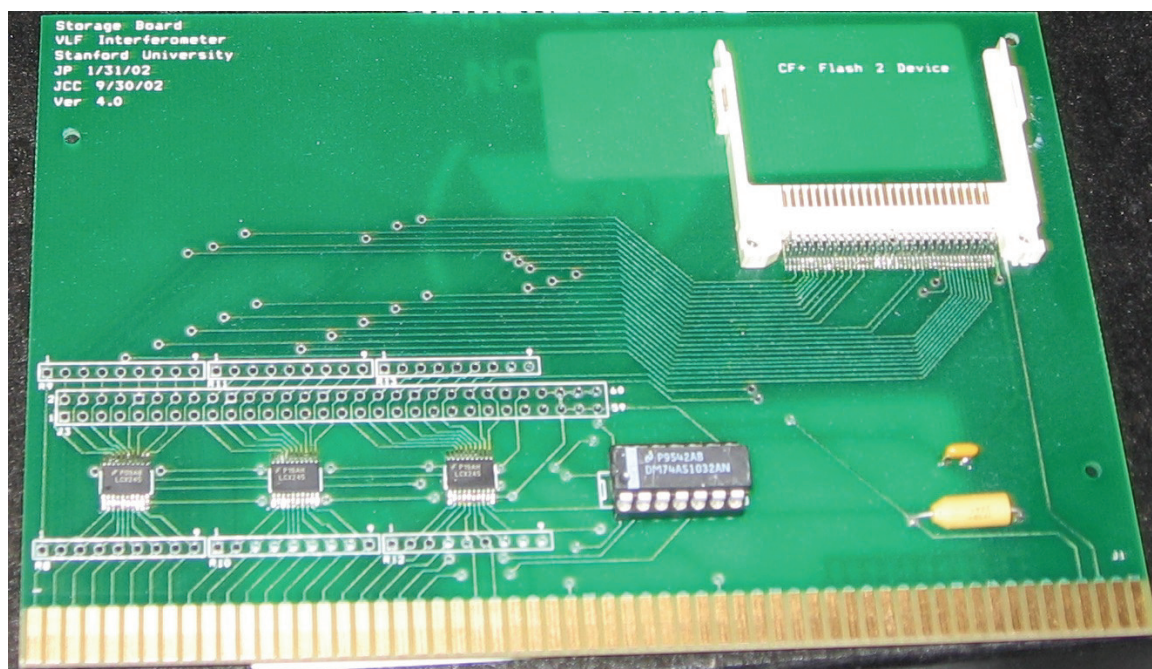
Figure A.5: CompactFlash Card Photograph
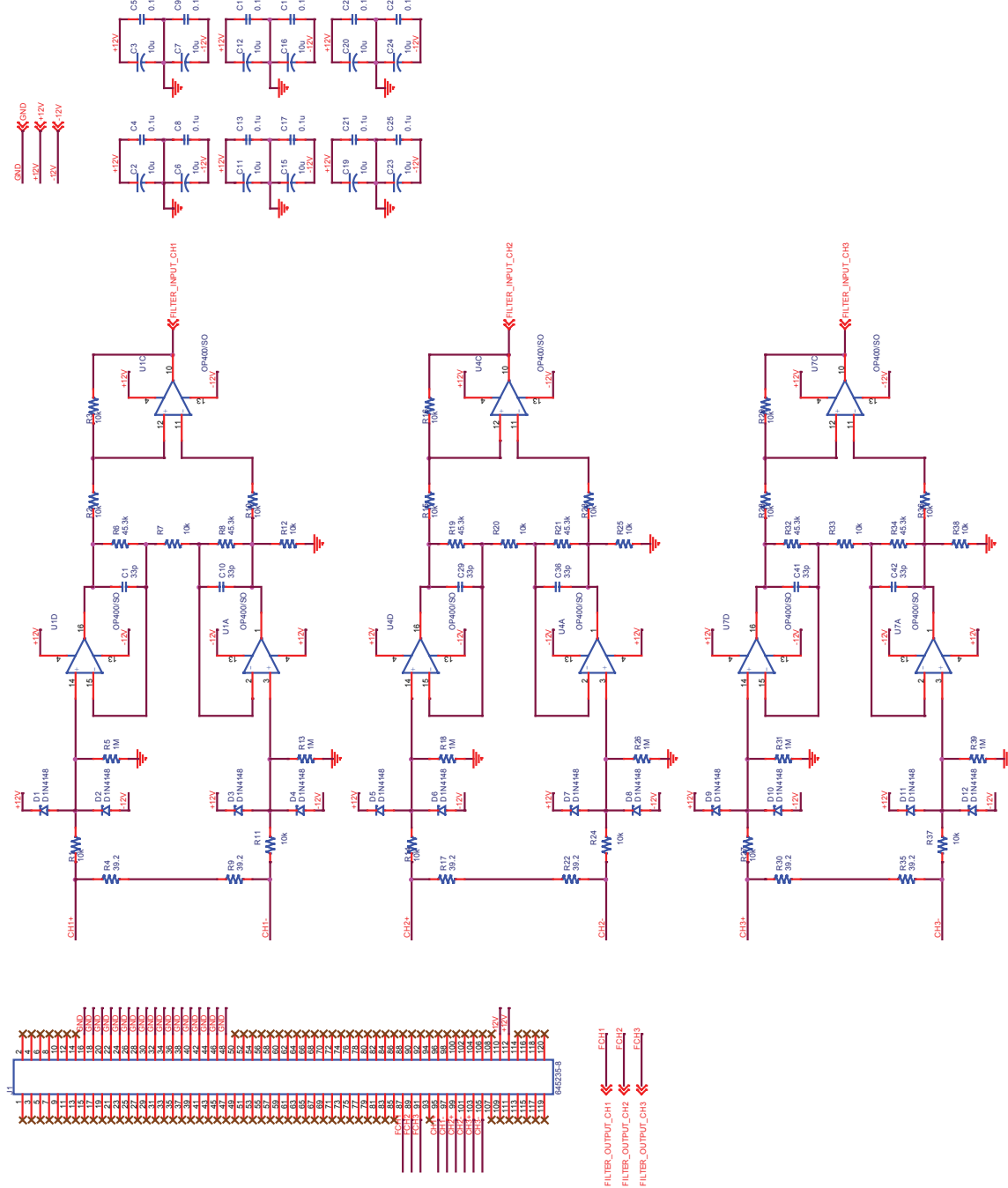
Figure A.6: Filter Card Schematic 1 of 4
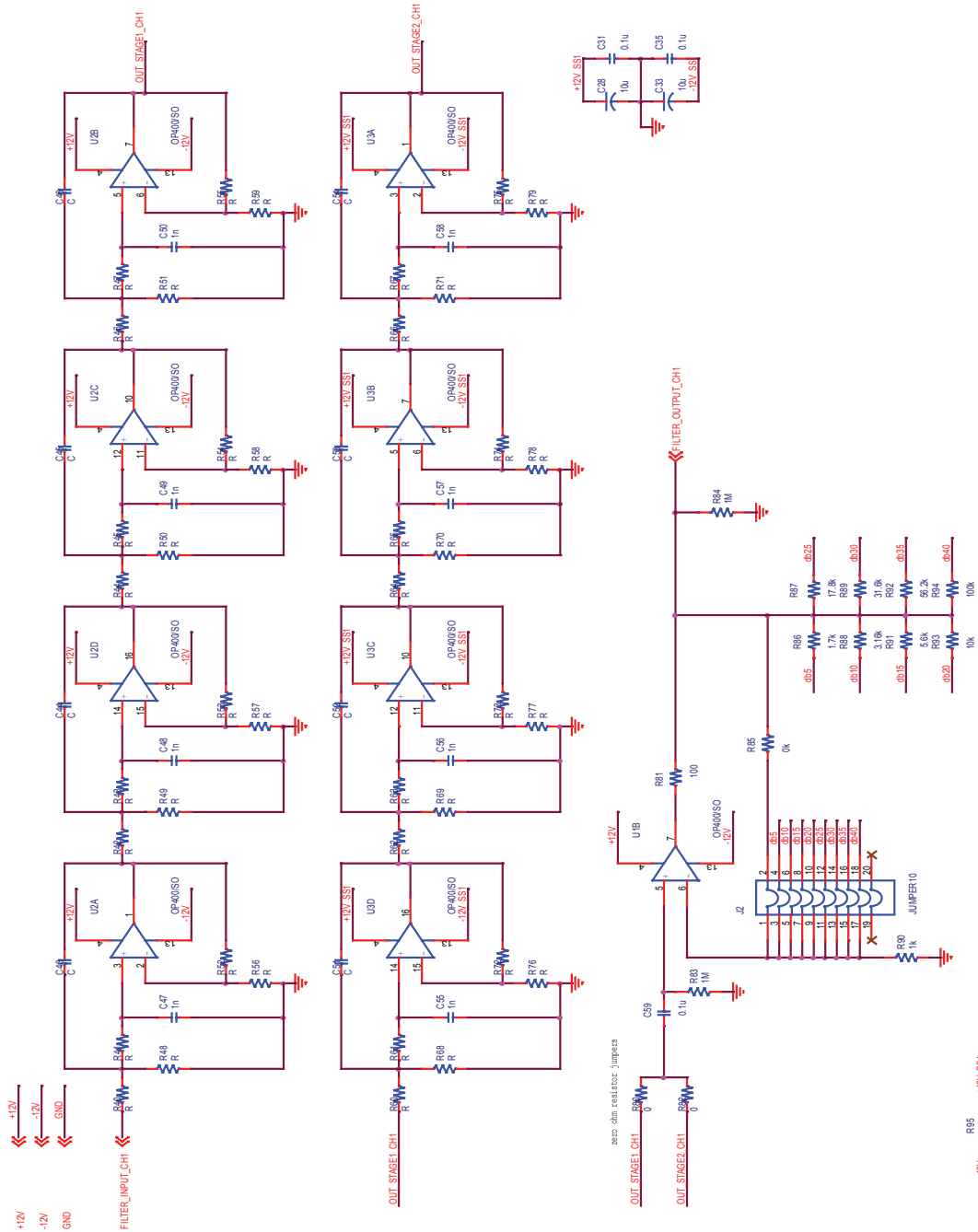
Figure A.7: Filter Card Schematic 2 of 4
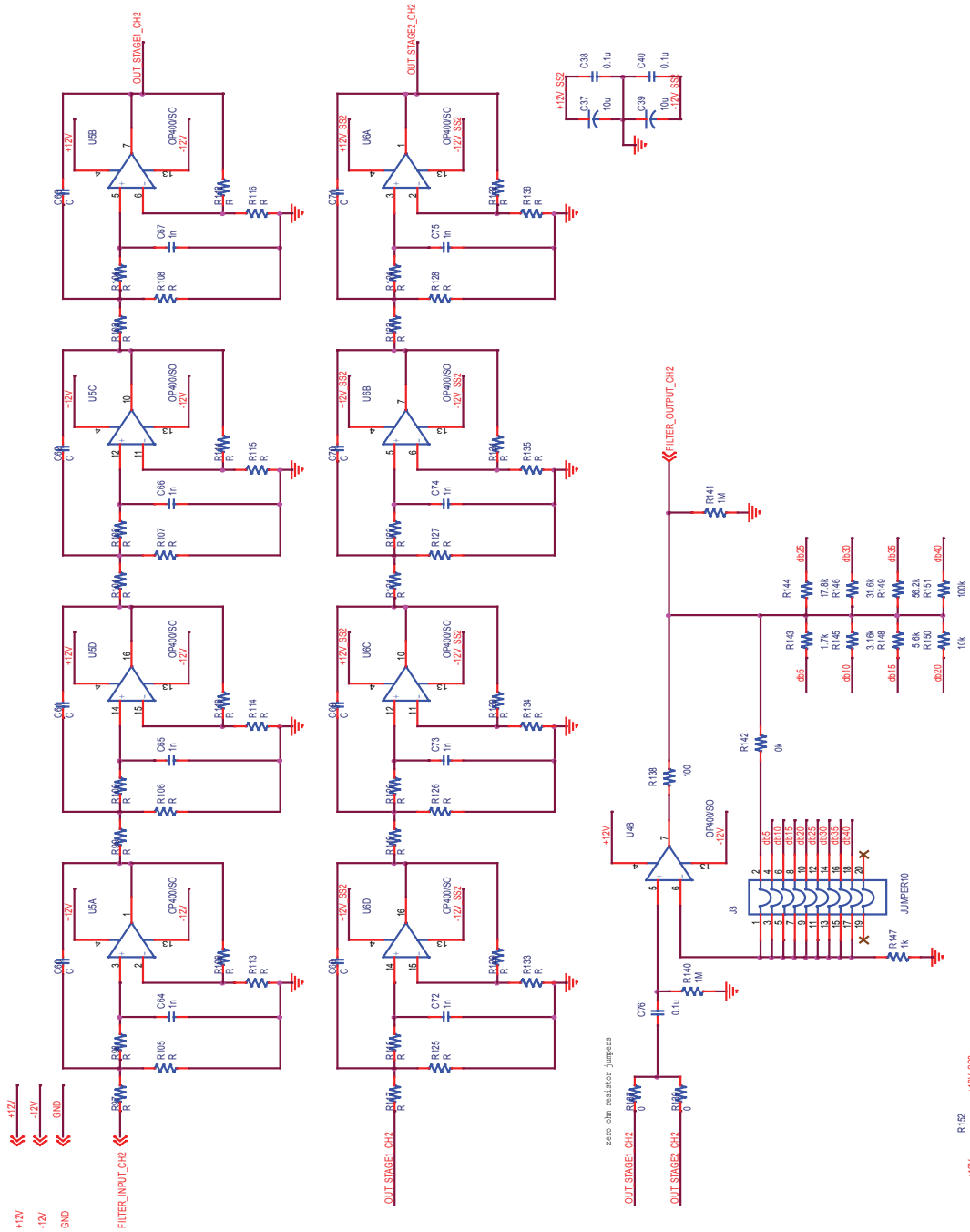
Figure A.8: Filter Card Schematic 3 of 4

Figure A.9: Filter Card Schematic 4 of 4
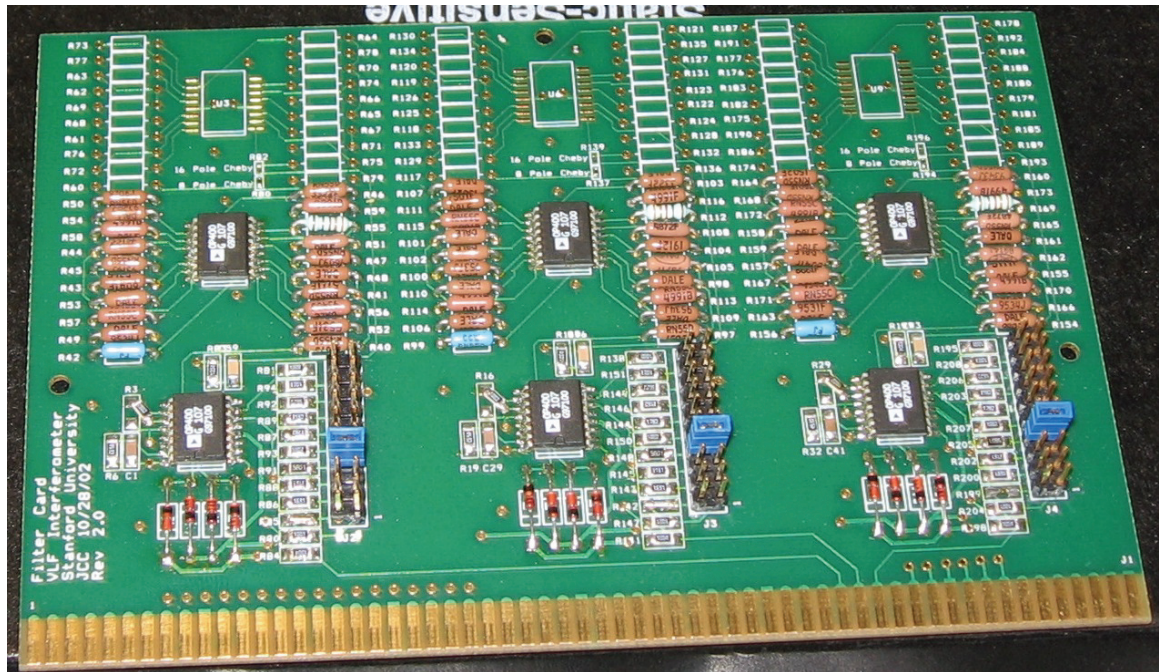
Figure A.10: Filter Card Photograph
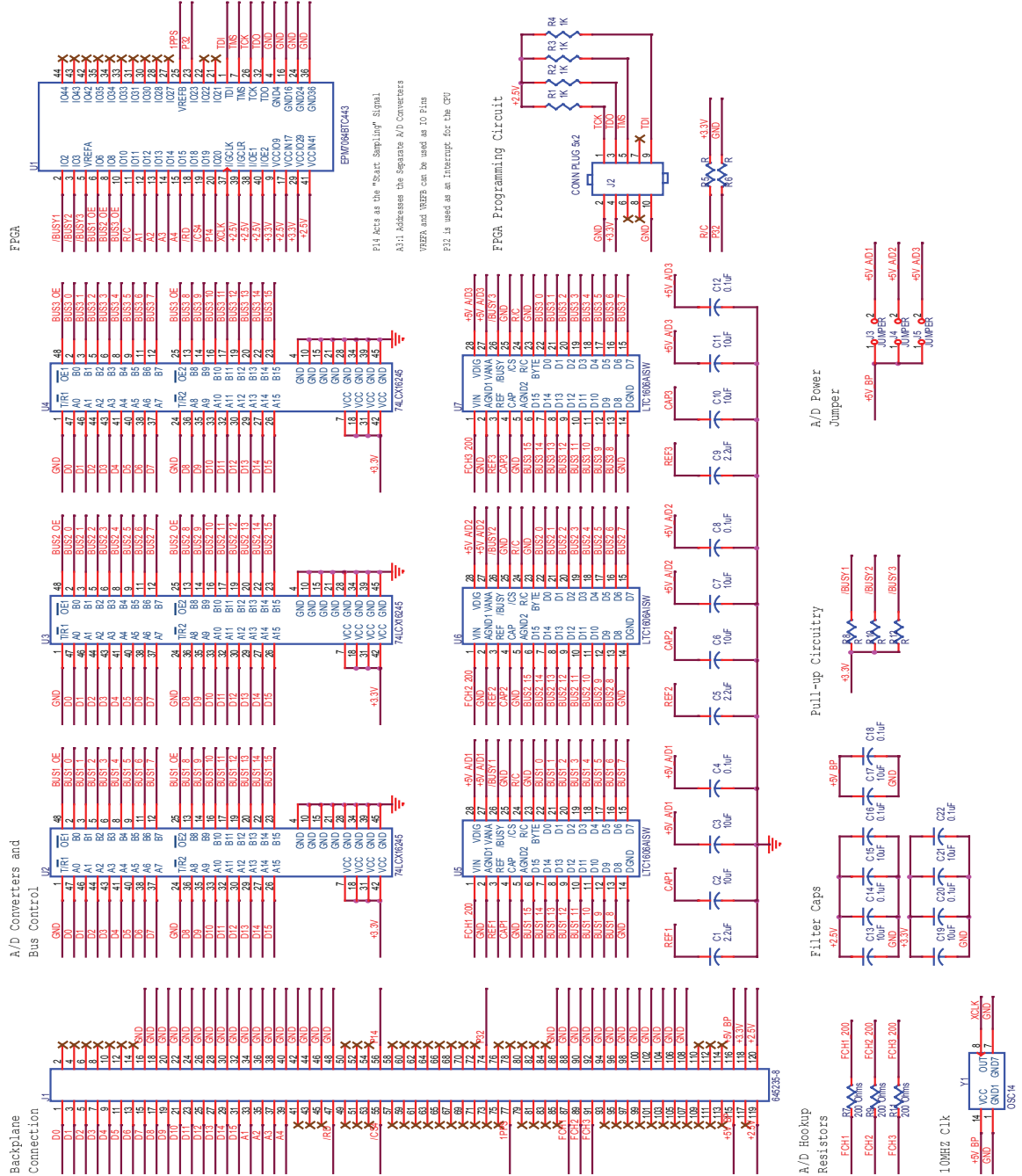
Figure A.11: Sampling Card Schematic
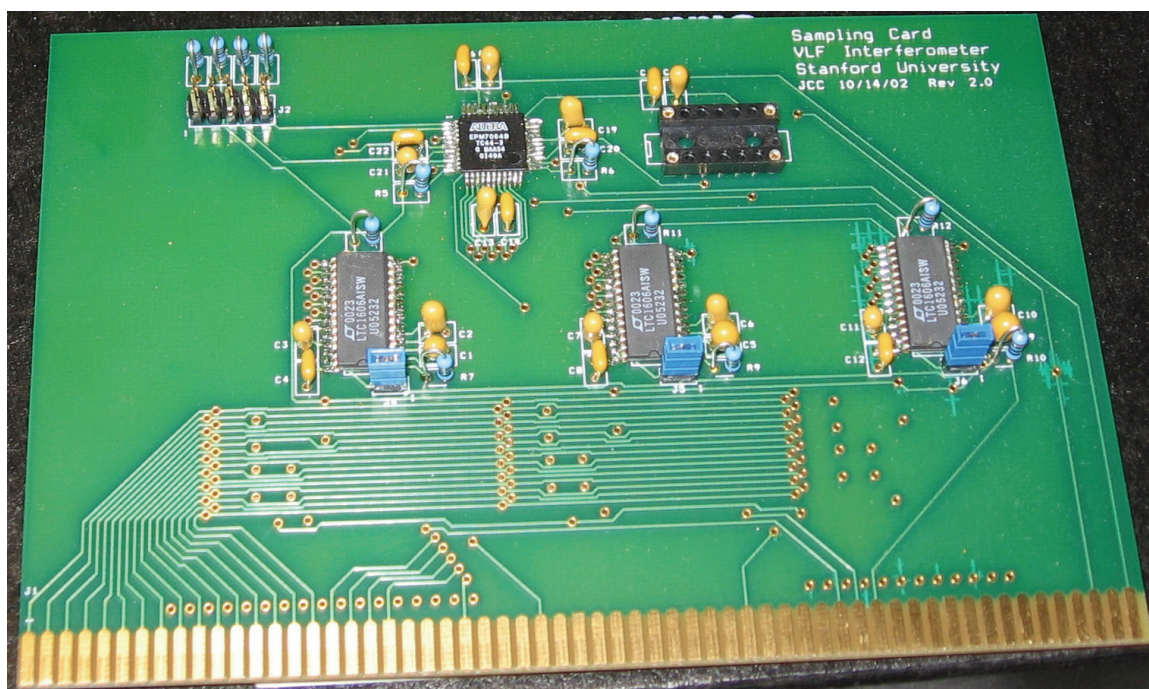
Figure A.12: Sampling Card Photograph
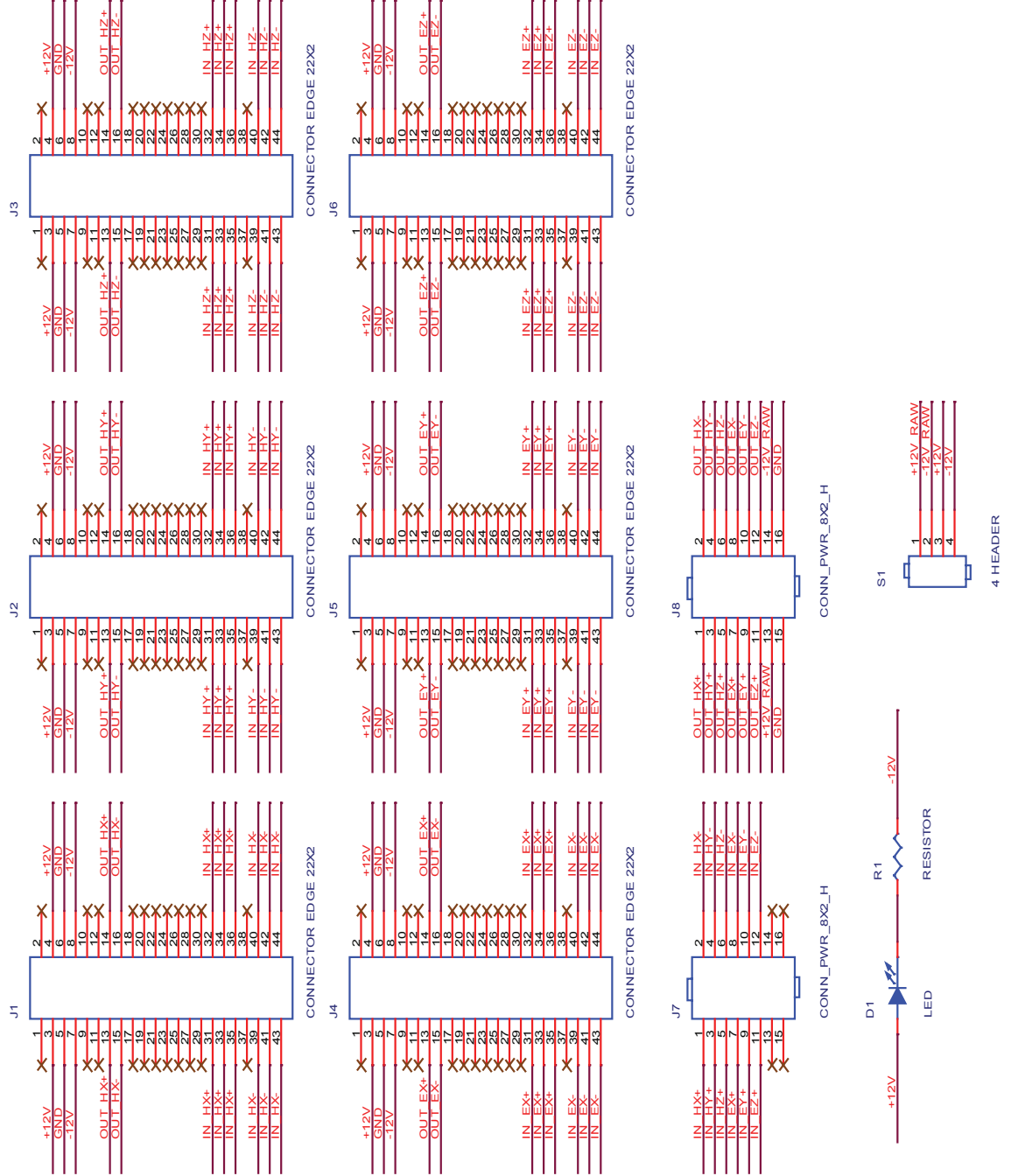
Figure A.13: Preamp Backplane Schematic
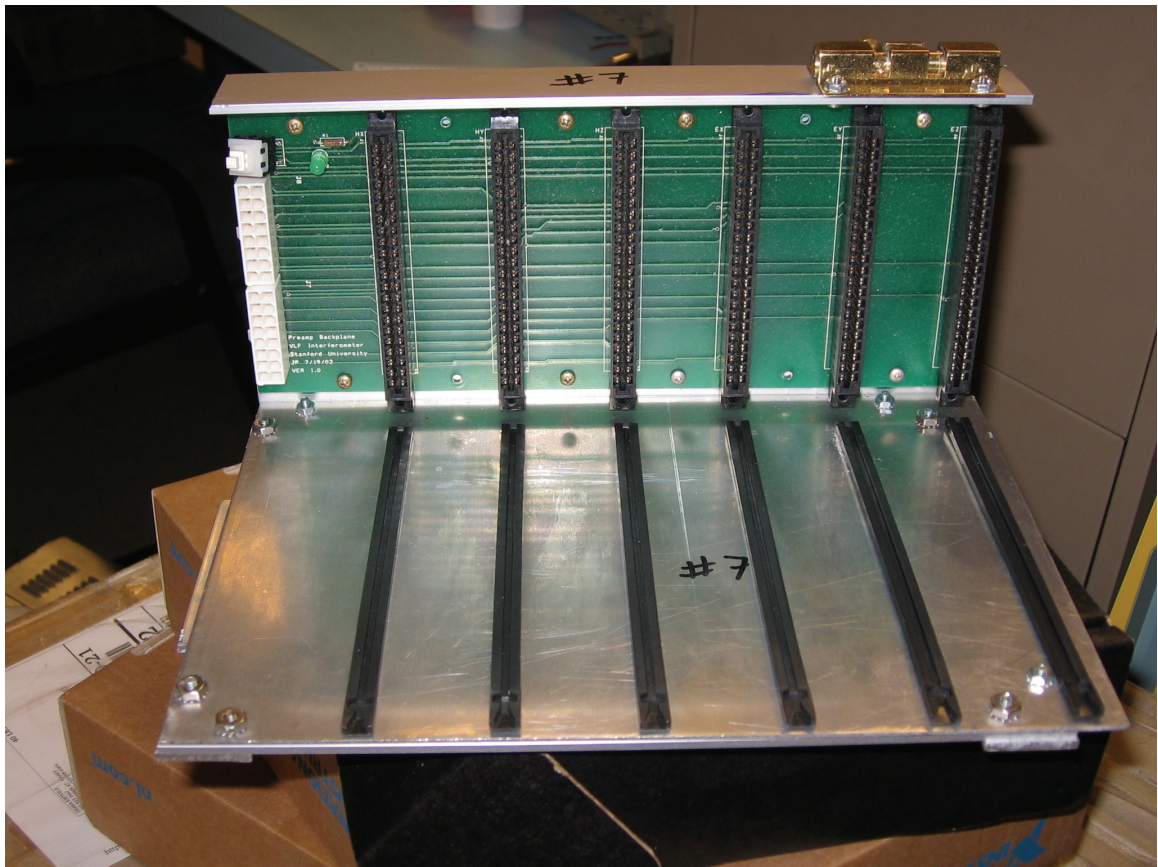
Figure A.14: Preamp Backplane Photograph
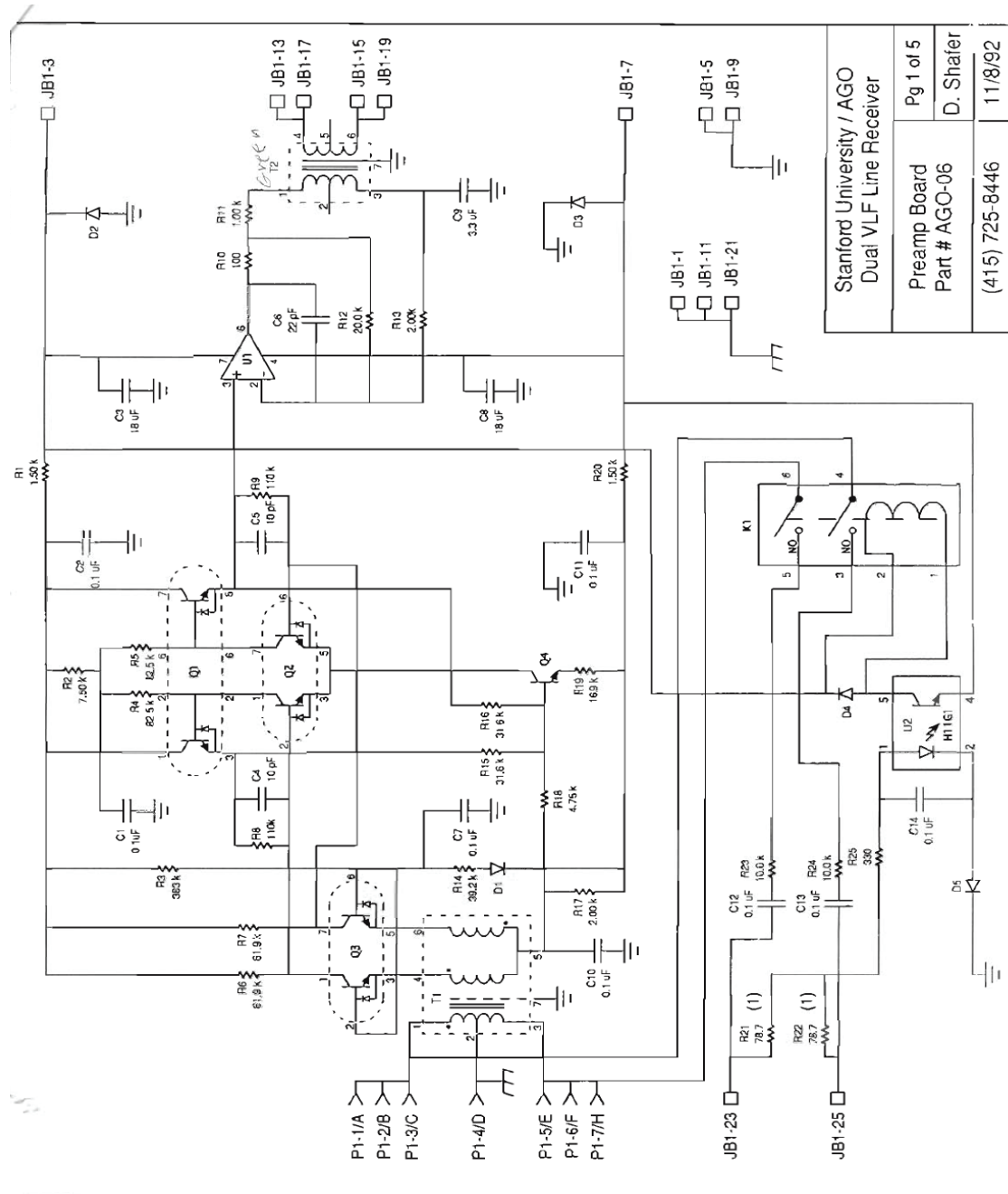
Figure A.15: BField Preamp Card Schematic
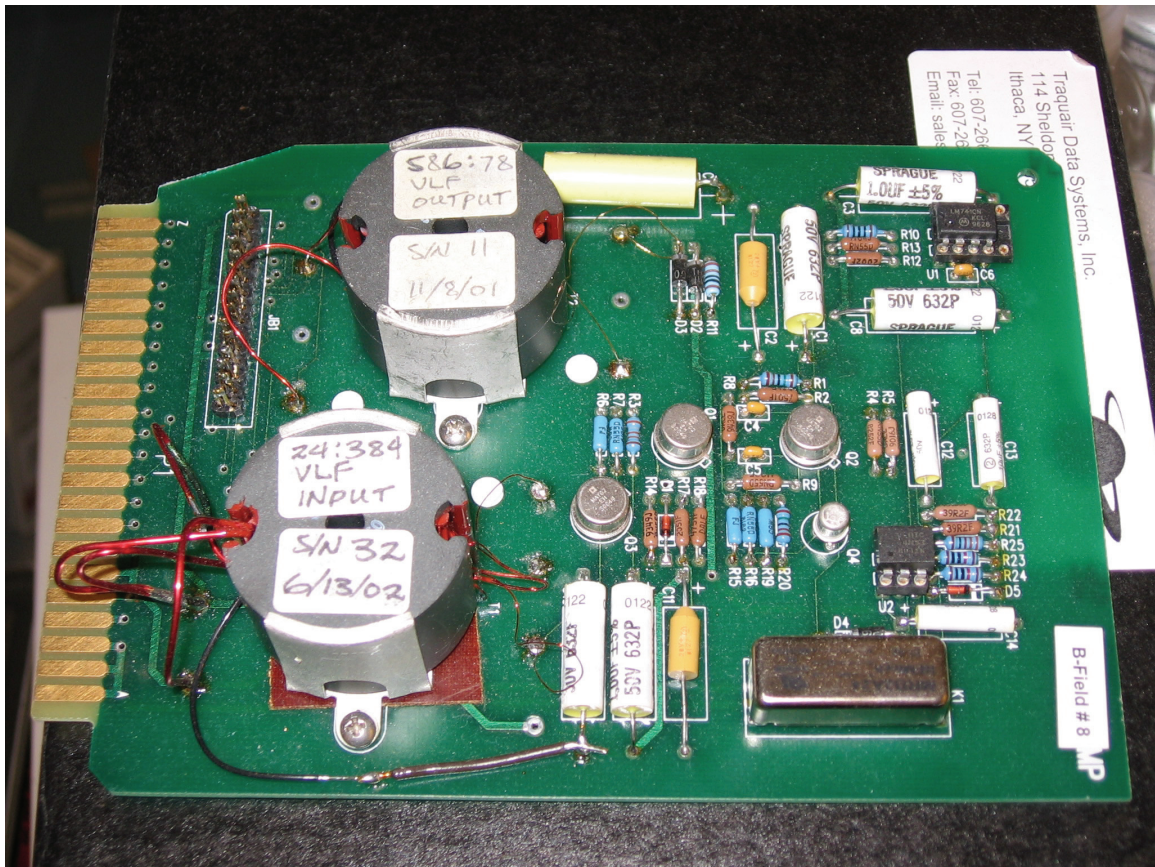
Figure A.16: BField Preamp Card Photograph

Figure A.17: EField Preamp Card Schematic
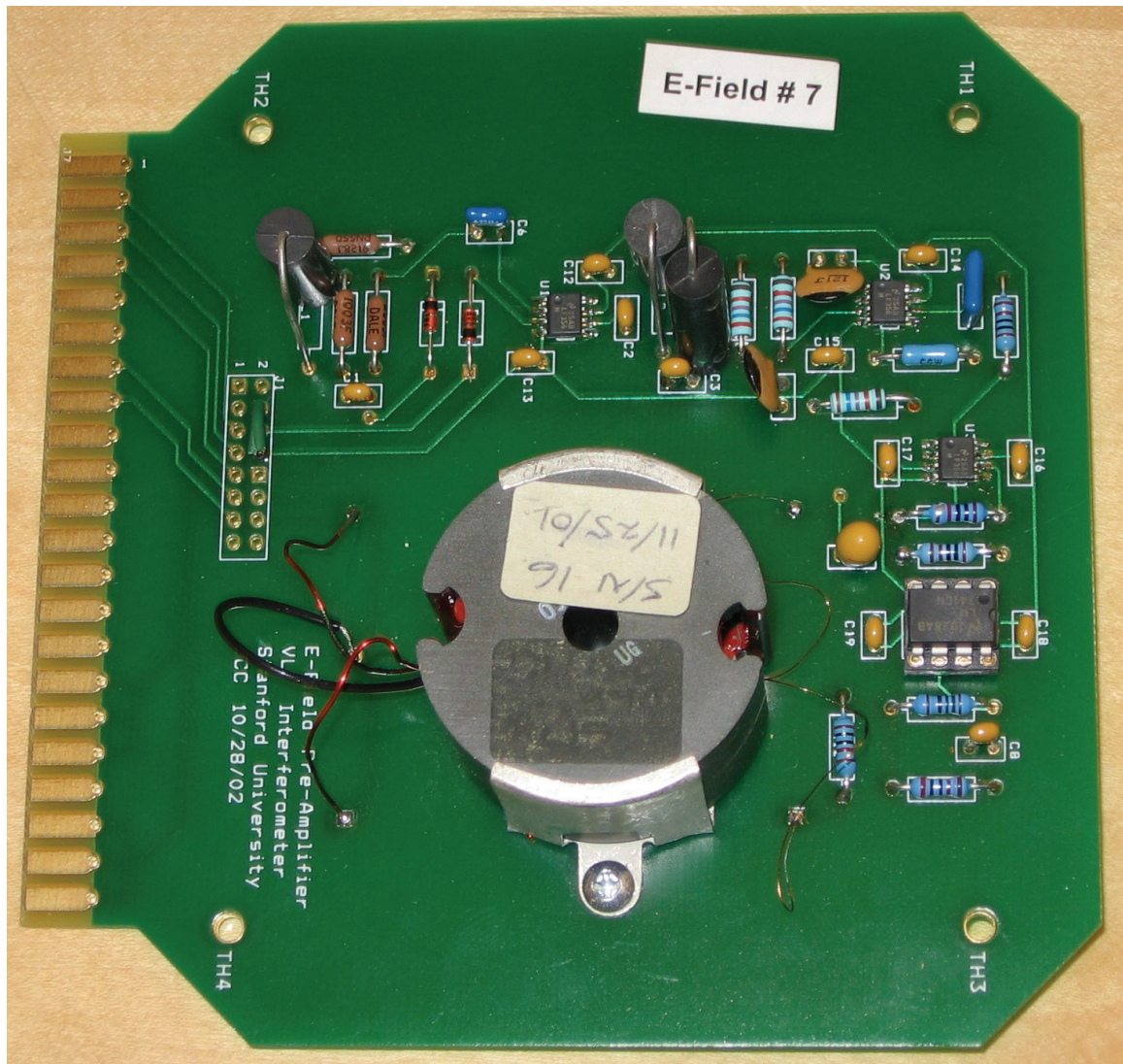
Figure A.18: EField Preamp Photograph

Appendix B

Calibration Results

In this appendix, the raw calibration values for the magnetic and electric field channels are presented.

B.1   Magnetic Channels

As explained in Chapter 2, the magnetic field channels are calibrated by using a secondary circuit to simulate the impedance of the antenna. In this section, the total system gain and phase delay are measured and recorded for each magnetic channel on the gain settings that were utilized during the Interferometer Campaign.

Antenna	Gain Setting	Frequency (Hz)	Gain	Phase Delay (rad)
NS	3	1875	27.5	-4.665265091
NS	3	2500	28.0	-0.502654825
NS	4	1875	43.0	-4.71238898
NS	4	2500	42.5	-0.439822972
EW	3	1875	30.5	-4.71238898
EW	3	2500	26.5	-0.439822972
EW	4	1875	47.5	-4.71238898
EW	4	2500	41.5	-0.502654825

Table B.1: BLK Magnetic Calibration Results

Antenna	Gain Setting	Frequency (Hz)	Gain	Phase Delay (rad)
NS	3	1875	27.5	-4.80663676
NS	3	2500	21.5	-0.439822972
NS	4	1875	42.0	-4.75951287
NS	4	2500	33.0	-0.502654825
EW	3	1875	28.5	-4.71238898
EW	3	2500	25.0	-0.565486678
EW	4	1875	43.0	-4.71238898
EW	4	2500	36.0	-0.691150384

Table B.2: HRP Magnetic Calibration Results

Antenna	Gain Setting	Frequency (Hz)	Gain	Phase Delay (rad)
NS	3	1875	38.5	-4.571017311
NS	3	2500	35.0	-0.628318531
NS	4	1875	58.0	-4.618141201
NS	4	2500	53.0	-0.565486678
EW	3	1875	27.5	-4.75951287
EW	3	2500	23.0	-0.502654825
EW	4	1875	42.5	-4.75951287
EW	4	2500	36.0	-0.502654825

Table B.3: KNL Magnetic Calibration Results

Antenna	Gain Setting	Frequency (Hz)	Gain	Phase Delay (rad)
NS	3	1875	27.0	-4.618141201
NS	3	2500	25.0	-0.314159265
NS	4	1875	39.0	-4.665265091
NS	4	2500	37.0	-0.314159265
EW	3	1875	29.0	-4.665265091
EW	3	2500	27.5	-0.628318531
EW	4	1875	42.0	-4.75951287
EW	4	2500	39.5	-0.502654825

Table B.4: LKL Magnetic Calibration Results

Antenna	Gain Setting	Frequency (Hz)	Gain	Phase Delay (rad)
NS	3	1875	28.0	-4.71238898
NS	3	2500	28.0	-0.628318531
NS	4	1875	41.5	-4.75951287
NS	4	2500	41.0	-0.628318531
EW	3	1875	26.0	-4.618141201
EW	3	2500	26.0	-0.471238898
EW	4	1875	39.0	-4.618141201
EW	4	2500	39.0	-0.471238898

Table B.5: PAX Magnetic Calibration Results

Antenna	Gain Setting	Frequency (Hz)	Gain	Phase Delay (rad)
NS	3	1875	29.2	-4.71238898
NS	3	2500	28.0	-0.565486678
NS	4	1875	46.0	-4.71238898
NS	4	2500	44.0	-0.565486678
EW	3	1875	28.5	-4.665265091
EW	3	2500	30.0	-0.502654825
EW	4	1875	46.5	-4.71238898
EW	4	2500	47.0	-0.502654825

Table B.6: SHP Magnetic Calibration Results

Antenna	Gain Setting	Frequency (Hz)	Gain	Phase Delay (rad)
NS	3	1875	28.5	-4.71238898
NS	3	2500	26.0	-0.565486678
NS	4	1875	43.0	-4.71238898
NS	4	2500	37.0	-0.565486678
EW	3	1875	29.0	-4.71238898
EW	3	2500	26.0	-0.565486678
EW	4	1875	43.0	-4.71238898
EW	4	2500	38.0	-0.565486678

Table B.7: SLA Magnetic Calibration Results

Antenna	Gain Setting	Frequency (Hz)	Gain	Phase Delay (rad)
NS	3	1875	28.0	-4.71238898
NS	3	2500	25.0	-0.628318531
NS	4	1875	44.0	-4.71238898
NS	4	2500	38.5	-0.628318531
EW	3	1875	30.0	-4.71238898
EW	3	2500	28.0	-0.691150384
EW	4	1875	46.0	-4.75951287
EW	4	2500	43.0	-0.691150384

Table B.8: TOK Magnetic Calibration Results

Antenna	Gain Setting	Frequency (Hz)	Gain	Phase Delay (rad)
NS	3	1875	27.5	-4.75951287
NS	3	2500	26.0	-0.565486678
NS	4	1875	45.0	-4.85376065
NS	4	2500	40.5	-0.565486678
EW	3	1875	28.0	-4.75951287
EW	3	2500	25.0	-0.502654825
EW	4	1875	43.0	-4.75951287
EW	4	2500	40.0	-0.628318531

Table B.9: VAL Magnetic Calibration Results

B.2 Electric Field

In Table B.10, the ratios of recorded sferics on the electric channel to the magnetic channels are listed. Using the calibration for the magnetic antennas, the strength of each electric field antenna can be determined from this ratio as described in Chapter 2.

For this measurement, the KNL system was broken for nearly the entire campaign and did not record a usable calibration spheric. The electric field antenna at VAL did not record usable data and its calibration is missing from the table as well. Finally, the electric antenna at LKL was extremely noisy and it was very difficult to selectively measure sferic signals. The calibration value is included in the table, but the electric measurement for LKL was not used in any data processing because of its inconsistency with other measurements.

Site	E/B Recorded Ratio
BLK	1.29
HRP	1.11
KNL	N/A
LKL	0.066
PAX	0.69
SHP	0.92
SLA	1.09
TOK	0.85
VAL	N/A

Table B.10: Sferic Electric Field Calibration

Appendix C

Derivation of Electromagnetic Equations

In this appendix, the equations used to propagate the electromagnetic fields generated by radiating currents in the ionosphere to a ground location are derived in Cartesian coordinates. First, the vector magnetic potential is derived. Second, the time harmonic magnetic fields are derived from the vector magnetic potential. Finally, the time harmonic electric fields are derived from the vector potential.

C.1   Derivation of the Vector Magnetic Potential

The starting point for the vector magnetic potential derivation is the solution to the vector wave equation

$$\mathbf{A}(\mathbf{r}) = \mu \int \int \int^{v'} \mathbf{J}(\mathbf{r}') \frac{e^{-ikR}}{4\pi R} dv' \tag{C.1}$$

where $\mathbf{r}'$ is the position of the radiating current element, $\mathbf{J}(\mathbf{r}')$ is the current density, μ is the permeability, k is the magnitude of the wavevector, R is the distance between points $\mathbf{r}'$ and $\mathbf{r}$, $\mathbf{r}$ is the point where the potential is measured, and v' is the volume space that contains the current elements [*Stutzman and Thiele*, 1998, p19].

130

Expand R by using its definition:

$$\mathbf{A}(\mathbf{r}) = \mu \int \int \int^{v'} \mathbf{J}(\mathbf{r}') \frac{e^{-ik|\mathbf{r}-\mathbf{r}'|}}{4\pi |\mathbf{r} - \mathbf{r}'|} dv' \tag{C.2}$$

Discretize the current elements:

$$\mathbf{A}(\mathbf{r}) \simeq \frac{\mu}{4\pi} \sum_{n=1}^{N} \mathbf{J}(\mathbf{r}_n) \frac{e^{-ik|\mathbf{r}-\mathbf{r}'|}}{|\mathbf{r} - \mathbf{r}'|} \Delta x_n \Delta y_n \Delta z_n \tag{C.3}$$

Assume volume elements have the same size:

$$\mathbf{A}(\mathbf{r}) \simeq \frac{\mu}{4\pi} \Delta V \sum_{n=1}^{N} \mathbf{J}(\mathbf{r}_n) \frac{e^{-ik|\mathbf{r}-\mathbf{r}'|}}{|\mathbf{r} - \mathbf{r}'|} \tag{C.4}$$

Break r and r' into Cartesian coordinates:

$$\mathbf{A}(\mathbf{r}) = \frac{\mu}{4\pi} \Delta V \sum_{n=1}^{N} \mathbf{J}(\mathbf{r}_n) \frac{e^{-ik\sqrt{(x-x_n)^2+(y-y_n)^2+(z-z_n)^2}}}{\sqrt{(x - x_n)^2 + (y - y_n)^2 + (z - z_n)^2}} \tag{C.5}$$

The above equation is the solution to the vector magnetic potential in free space given a number of discrete current dipole elements.

C.2 Solve Magnetic Field

Solve for the magnetic field by starting with the definition of the vector magnetic potential:

$$\mathbf{B} = \nabla \times \mathbf{A} \tag{C.6}$$

Apply the results from Equation C.5:

$$\mathbf{B} = \frac{\mu}{4\pi} \Delta V \sum_{n=1}^{N} \left\{ \nabla \times [J_{x_n}\widehat{x} + J_{y_n}\widehat{y} + J_{z_n}\widehat{z}] \frac{e^{-ik\sqrt{(x-x_n)^2+(y-y_n)^2+(z-z_n)^2}}}{\sqrt{(x - x_n)^2 + (y - y_n)^2 + (z - z_n)^2}} \right\} \tag{C.7}$$

Break the solution into a separate equation for each Cartesian component and use $\mathbf{R} = (x - x_n)\,\hat{\mathbf{x}} + (y - y_n)\,\hat{\mathbf{y}} + (z - z_n)\,\hat{\mathbf{z}}$ and $R = |\mathbf{R}|$:

$$B_x = \frac{\mu}{4\pi}\Delta V \sum_{n=1}^{N}\left[J_{y_n}\left(z - z_n\right) - J_{z_n}\left(y - y_n\right)\right]\frac{(1 + ikR)}{R^3}e^{-ikR} \qquad \text{(C.8)}$$

$$B_y = \frac{\mu}{4\pi}\Delta V \sum_{n=1}^{N}\left[J_{z_n}\left(x - x_n\right) - J_{x_n}\left(z - z_n\right)\right]\frac{(1 + ikR)}{R^3}e^{-ikR} \qquad \text{(C.9)}$$

$$B_z = \frac{\mu}{4\pi}\Delta V \sum_{n=1}^{N}\left[J_{x_n}\left(y - y_n\right) - J_{y_n}\left(x - x_n\right)\right]\frac{(1 + ikR)}{R^3}e^{-ikR} \qquad \text{(C.10)}$$

The above three equations represent the magnetic field at a location due to a set of radiating current dipole elements in free space.

C.3   Solve Electric Field

Solve for the ground based electric field by assuming the Lorentz condition on the vector magnetic potential:

$$\mathbf{E} = -i\omega\mathbf{A} - \mathbf{i}\frac{\nabla\left(\nabla \cdot \mathbf{A}\right)}{\omega\mu\epsilon} \qquad \text{(C.11)}$$

Discretize the current elements:

$$\mathbf{E} = \frac{-i\omega\frac{\mu}{4\pi}\Delta V \sum_{n=1}^{N}\mathbf{J}(\mathbf{r}_n)\frac{e^{-ikR}}{R} - i\frac{\mu}{4\pi}\Delta V \frac{1}{\omega\mu\epsilon}\cdot}{\sum_{n=1}^{N}\nabla\left\{\nabla \cdot \left(\left[J_{x_n}\hat{x} + J_{y_n}\hat{y} + J_{z_n}\hat{z}\right]\frac{e^{-ik\sqrt{(x-x_n)^2+(y-y_n)^2+(z-z_n)^2}}}{\sqrt{(x-x_n)^2+(y-y_n)^2+(z-z_n)^2}}\right)\right\}} \qquad \text{(C.12)}$$

Group like terms:

$$\mathbf{E} = -i\frac{\mu}{4\pi}\Delta V \sum_{n=1}^{N}\left\{\begin{array}{c}\omega\mathbf{J}(\mathbf{r}_n)\frac{e^{-ikR}}{R} - \frac{1}{\omega\mu\epsilon}\\ \nabla\left[\frac{(1+ikR)}{R^3}\left[J_{x_n}\left(x - x_n\right) + J_{y_n}\left(y - y_n\right) + J_{z_n}\left(z - z_n\right)\right]e^{-ikR}\right]\end{array}\right\} \qquad \text{(C.13)}$$

Break the solution into Cartesian components and use the following simplifying relationship:

$$\mathbf{J} \cdot \mathbf{R} = J_{x_n} \left(x - x_n \right) + J_{y_n} \left(y - y_n \right) + J_{z_n} \left(z - z_n \right) \tag{C.14}$$

$$E_x = i\frac{1}{4\pi\omega\epsilon}\Delta V \sum_{n=1}^{N} \left\{ \begin{array}{l} J_{x_n} \left(-\omega^2\mu\epsilon R^4 + ikR^3 + R^2 \right) + \\ \left(\mathbf{J} \cdot \mathbf{R} \right) \left(x - x_n \right) \left(-3 - 3ikR + k^2R^2 \right) \end{array} \right\} \frac{e^{-ikR}}{R^5} \tag{C.15}$$

$$E_y = i\frac{1}{4\pi\omega\epsilon}\Delta V \sum_{n=1}^{N} \left\{ \begin{array}{l} J_{y_n} \left(-\omega^2\mu\epsilon R^4 + ikR^3 + R^2 \right) + \\ \left(\mathbf{J} \cdot \mathbf{R} \right) \left(y - y_n \right) \left(-3 - 3ikR + k^2R^2 \right) \end{array} \right\} \frac{e^{-ikR}}{R^5} \tag{C.16}$$

$$E_z = i\frac{1}{4\pi\omega\epsilon}\Delta V \sum_{n=1}^{N} \left\{ \begin{array}{l} J_{z_n} \left(-\omega^2\mu\epsilon R^4 + ikR^3 + R^2 \right) + \\ \left(\mathbf{J} \cdot \mathbf{R} \right) \left(z - z_n \right) \left(-3 - 3ikR + k^2R^2 \right) \end{array} \right\} \frac{e^{-ikR}}{R^5} \tag{C.17}$$

Substitute $k = \omega\sqrt{\mu\epsilon}$

$$E_x = i\frac{\Delta V}{4\pi k}\sqrt{\frac{\mu}{\epsilon}} \sum_{n=1}^{N} \left\{ \begin{array}{l} J_{x_n} \left(-k^2 R^4 + ikR^3 + R^2 \right) + \\ \left(\mathbf{J} \cdot \mathbf{R} \right) \left(x - x_n \right) \left(-3 - 3ikR + k^2R^2 \right) \end{array} \right\} \frac{e^{-ikR}}{R^5} \tag{C.18}$$

$$E_y = i\frac{\Delta V}{4\pi k}\sqrt{\frac{\mu}{\epsilon}} \sum_{n=1}^{N} \left\{ \begin{array}{l} J_{y_n} \left(-k^2 R^4 + ikR^3 + R^2 \right) + \\ \left(\mathbf{J} \cdot \mathbf{R} \right) \left(y - y_n \right) \left(-3 - 3ikR + k^2R^2 \right) \end{array} \right\} \frac{e^{-ikR}}{R^5} \tag{C.19}$$

$$E_z = i\frac{\Delta V}{4\pi k}\sqrt{\frac{\mu}{\epsilon}} \sum_{n=1}^{N} \left\{ \begin{array}{l} J_{z_n} \left(-k^2 R^4 + ikR^3 + R^2 \right) + \\ \left(\mathbf{J} \cdot \mathbf{R} \right) \left(z - z_n \right) \left(-3 - 3ikR + k^2R^2 \right) \end{array} \right\} \frac{e^{-ikR}}{R^5} \tag{C.20}$$

The above three equations represent the electric field at a location due to a set of radiating current dipole elements in free space.

C.4   Image Currents

Because the ground conductivity at low frequencies is fairly large[1], the ground is treated as a perfect conductor when predicting the radiation pattern generated from ionospheric currents. The easiest way to model this is to place image currents below the conducting plane [*Pirjola and Viljanen*, 1998].

Assuming a perfect conductor, the original current element is decomposed into an in-plane component ($\mathbf{J}_{||}$), and a normal component ($\mathbf{J_n}$). The image current then takes on the following form:

$$\mathbf{J_{image}} = -\mathbf{J}_{||} + \mathbf{J_n} \tag{C.21}$$

The image current is located at a depth below the conducting plane equivalent to the height above the conducting plane of the original current. An image current of this form matches the necessary boundary conditions at the interface between free space and the perfect conductor.

---

[1]The ground conductivity in Alaska at very low frequencies is between 2 and 4 mS/m. The FCC maintains a ground conductivity map of the US at the URL: (http://www.fcc.gov/mb/audio/m3/).

Appendix D

Effective Loss Rates for Heating Model

To approximate the loss terms, elastic collisions, rotational excitation, and vibrational excitation for both N_2 and O_2 molecules are modeled. Following the formulas derived in [*Rodriguez*, 1994, p176-177], the elastic loss terms in Watts per degree kelvin (W/K) are:

$$L_{\text{elast}}(N_2) = 1.89 \times 10^{-44} N_e N_{N_2} \left(1 - 1.21 \times 10^{-4} T_e\right) T_e \left(T_e - T_n\right) \quad \text{(D.1)}$$

$$L_{\text{elast}}(O_2) = 1.29 \times 10^{-43} N_e N_{O_2} \left(1 - 3.6 \times 10^{-2} T_e^{1/2}\right) T_e^{1/2} \left(T_e - T_n\right) \quad \text{(D.2)}$$

where N_e is the electron density, N_{N_2} is the concentration of N_2, N_{O_2} is the concentration of O_2, T_n is the neutral temperature of the plasma, and T_e is the electron temperature of the plasma measured in degrees Kelvin.

The rotation excitation terms in W/K are [*Rodriguez*, 1994, p177]

$$L_{\text{rot}}(N_2) = 4.65 \times 10^{-39} N_e N_{N_2} \left(\frac{T_e - T_n}{T_e^{0.5}}\right) \quad \text{(D.3)}$$

$$L_{\text{rot}}(O_2) = 1.11 \times 10^{-38} N_e N_{O_2} \left(\frac{T_e - T_n}{T_e^{0.5}}\right) \quad \text{(D.4)}$$

The vibrational excitation loss terms for N_2 in W/K is [*Rodriguez*, 1994, p178]

$$L_{\text{vib}}(N_2) = 4.79 \times 10^{-37} N_e N_{N_2} \exp\left(f\frac{T_e - 2000}{2000 T_e}\right)\left[1 - \exp\left(-g\frac{T_e - T_n}{T_n T_e}\right)\right] \quad \text{(D.5)}$$

where f is a dimensionless quantity defined below

$$f = 1.06 \times 10^4 + 7.51 \times 10^3 \text{tanh}[0.0011(T_e - 1800)] \quad \text{(D.6)}$$

and g is also a dimensionless quantity defined as

$$g = 3300 + 1.233(T_e - 1000) - 2.056 \times 10^{-4}(T_e - 1000)(T_e - 4000) \quad \text{(D.7)}$$

The vibrational excitation loss term for O_2 in W/K is [*Rodriguez*, 1994, p178]

$$L_{\text{vib}}(O_2) = 8.32 \times 10^{-38} N_e N_{O_2} \exp\left(f\frac{T_e - 700}{700 T_e}\right)\left[1 - \exp\left(-2700\frac{T_e - T_n}{T_n T_e}\right)\right] \quad \text{(D.8)}$$

where f is a dimensionless quantity defined as

$$f = 3300 - 839 \cdot \sin[0.000191(T_e - 2700)] \quad \text{(D.9)}$$

ν_{eff} is calculated by summing the collision rate from O_2 and N_2 [*Rodriguez*, 1994, p176]. The units are in s^{-1}.

$$\nu_{\text{eff}}(N_2) = \left(\frac{5}{3}\right) \cdot 2.33 \times 10^{-17} N_{N_2}(1 - 1.21 \times 10^{-4} T_e) T_e \quad \text{(D.10)}$$

$$\nu_{\text{eff}}(O_2) = \left(\frac{5}{3}\right) \cdot 1.82 \times 10^{-16} N_{O_2}(1 + 3.60 \times 10^{-2} T_e^{1/2}) T_e^{1/2} \quad \text{(D.11)}$$

The additional 5/3 factors in the equations above are to make the collision rate consistent with quasi-longitudinal propagation [*Rodriguez*, 1994, p32-33].

Bibliography

Akasofu, S.-I., S. Chapman, and C.-I. Meng (1965), The polar electrojet, *Journal of Atmospheric and Terrestrial Physics*, *27*, 1275–1305.

Banks, P. M., and J. R. Doupnik (1975), A review of auroral zone electrodynamics deduced from incoherent scatter radar observations, *Journal of Atmospheric and Terrestrial Physics*, *37*, 951–972.

Barr, R. (1998), The generation of ELF and VLF radio waves in the ionosphere using powerful HF transmitters, *Advances in Space Research*, *21*, 677–687.

Barr, R., and P. Stubbe (1984), ELF and VLF radiation from the 'polar electrojet antenna', *Radio Science*, *19*, 1111–1122.

Barr, R., and P. Stubbe (1991a), On the ELF generation efficiency of the Tromsø heater facility, *Geophys. Res. Lett.*, *18*, 1971–1974.

Barr, R., and P. Stubbe (1991b), ELF radiation from the Tromsø 'super heater' facility, *Geophys. Res. Lett.*, *18*, 1035–1038.

Barr, R., and P. Stubbe (1993), ELF harmonic radiation from the Tromsø heating facility, *Geophys. Res. Lett.*, *20*, 2243–2246.

Barr, R., M. T. Rietveld, H. Kopka, P. Stubbe, and E. Nielsen (1985), Extra-low-frequency radiation from the polar electrojet antenna, *Nature*, *317*, 155–157.

Barr, R., P. Stubbe, M. T. Rietveld, and H. Kopka (1986), ELF and VLF signals radiated by the 'polar electrojet antenna' - experimental results, *J. Geophys. Res.*, *91*, 4451–4459.

Bell, T. F., U. S. Inan, M. T. Danielson, and S. A. Cummer (1995), VLF signatures of ionospheric heating by HIPAS, *Radio Science*, *30*, 1855–1868, doi: 10.1029/95RS02191.

Bell, T. F., U. S. Inan, M. Platino, J. S. Pickett, P. A. Kossey, and E. J. Kennedy (2004), CLUSTER observations of lower hybrid waves excited at high altitudes by electromagnetic whistler mode signals from the HAARP facility, *Geophys. Res. Lett.*, *31*, L06,811, doi:10.1029/2003GL018855.

Bittencourt, J. A. (2003), *Fundamentals of Plasma Physics*, Bittencourt, J. A.

Boyd, S., and L. Vandenberghe (2004), *Convex Optimization*, Cambridge University Press, New York, NY, USA.

Budden, K. G. (1985), *The Propagation of Radio Waves*, Press Syndicate of the University of Cambridge, 32 East 57th Street, New York, NY 10022, USA.

Budilin, L. V., et al. (1977), Localization of the altitude of nonlinear currents responsible for low-frequency emission in the ionosphere, *Radiofizika*, *20*, 83–86.

Carroll, K. J., and A. J. Ferraro (1990), Computer simulation of ELF injection in the earth-ionosphere waveguide, *Radio Science*, *25*, 1363–1367.

Casey, J. P. (2005), Overview of the equatorial electrojet and related ionospheric current systems, *Tech. rep.*, Naval Undersea Warfare Center Division, Newport, Rhode Island.

Chevalier, M. W. (2006), Advances in the perfectly matched layer absorbing boundary condition and a technique for efficiently modeling long path propagation with applications to finite-difference grid techniques, Ph.D. thesis, Stanford University.

Chevalier, T. W., U. S. Inan, and T. F. Bell (2007), Terminal impedance and antenna current distribution of a VLF electric dipole in the inner magnetosphere, in submission to IEEE Transactions on Antennas and Propagation.

Davies, K. (1990), *Ionospheric Radio*, Peter Peregrinus Ltd.

Ferraro, A. J., H. S. Lee, R. A. Allshouse, K. Carroll, A. A. Tomko, F. J. Kelly, and R. G. Joiner (1982), VLF/ELF radiation from the ionospheric dynamo current system modulated by powerful HF signals, *Journal of Atmospheric and Terrestrial Physics*, *44*, 1113–1122.

Ferraro, A. J., H. S. Lee, R. Allshouse, K. Carroll, R. Lunnen, and T. Collins (1984), Characteristics of ionospheric ELF radiation generated by HF heating, *Journal of Atmospheric and Terrestrial Physics*, *46*, 855–865.

Ferraro, A. J., H. S. Lee, T. W. Collins, M. Baker, and D. Werner (1989), Measurements of extremely low frequency signals from modulation of the polar electrojet above Fairbanks, Alaska, *IEEE Transactions on Antennas and Propagation*, *37*, 802–805.

Getmantsev, G. G., N. A. Zuikov, D. S. Kotik, L. F. Mironenko, N. A. Mitiakov, V. O. Rapoport, I. A. Sazonov, V. I. Trakhtengerts, and V. I. Eidman (1974), Combination frequencies in the interaction between high-power short-wave radiation and ionospheric plasma, *ZhETF Pis ma Redaktsiiu*, *20*, 229–232.

Golub, G. H., and C. F. V. Loan (1996), *Matrix Computations*, Johns Hopkins University Press, Baltimore, MD, USA.

Hansen, P. C. (1998), *Rank-deficient and discrete ill-posed problems: numerical aspects of linear inversion*, Society for Industrial and Applied Mathematics, Philadelphia, PA, USA.

Horowitz, P., and W. Hill (1989), *The Art of Electronics*, 2 ed., Cambridge University Press.

Inan, U. S., F. A. Knifsend, and J. Oh (1990), Subionospheric VLF 'imaging' of lightning-induced electron precipitation from the magnetosphere, *J. Geophys. Res.*, *95*, 17,217–17,231.

Inan, U. S., et al. (2004), Multi-hop whistler-mode ELF/VLF signals and triggered emissions excited by the HAARP HF heater, *Geophys. Res. Lett.*, *31*, L24,805, doi:10.1029/2004GL021647.

James, H. G., R. L. Dowden, M. T. Rietveld, P. Stubbe, and H. Kopka (1984), Simultaneous observations of ELF waves from an artificially modulated auroral electrojet in space and on the ground, *J. Geophys. Res.*, *89*, 1655–1666.

James, H. G., U. S. Inan, and M. T. Rietveld (1990), Observations on the DE 1 spacecraft of ELF/VLF waves generated by an ionospheric heater, *J. Geophys. Res.*, *95*, 12,187–12,195.

Kamide, Y., and A. Brekke (1993), Altitude variations of ionospheric currents at auroral latitudes, *Geophys. Res. Lett.*, *20*, 309–312.

Kamide, Y., S.-I. Akasofu, B.-H. Ahn, W. Baumjohann, and J. L. Kisabeth (1982), Total current of the auroral electrojet estimated from the IMS Alaska meridian chain of magnetic observatories, *Planet. Space Sci.*, *30*, 621–625, doi:10.1016/0032-0633(82)90022-8.

Kapustin, I. N., R. A. Pertsovskii, A. N. Vasilev, V. S. Smirnov, O. M. Raspopov, L. E. Soloveva, A. A. Uliachenko, A. A. Arykov, and N. V. Galakhova (1977), Generation of radiation at combination frequencies in the region of the auroral electric jet, *ZhETF Pis ma Redaktsiiu*, *25*, 248–251.

Knecht, D. F. (1972), *The Geomagnetic Field, A Revision of Chapter 11 of Handbook of Geophysics and Space Environments*, Air Force Cambridge Research Laboratories, Hanscom Field, Bedford, MA.

Lee, J., and D. Kalluri (1999), Three-dimensional fdtd simulation of electromagnetic wave transformation in a dynamic inhomogeneous magnetized plasma, *IEEE Transactions on Antennas and Propagation*, *47*(7), 1146–1151.

McCarrick, M. J., A. Y. Wong, R. F. Wuerker, B. Chouinard, and D. D. Sentman (1990), Excitation of ELF waves in the Schumann resonance range by modulated HF heating of the polar electrojet, *Radio Science*, *25*, 1291–1298.

Milikh, G., K. Papadopoulos, M. McCarrick, and J. Preston (1999), ELF emission generated by the HAARP HF-heater using varying frequency and polarization, *Radiophysics and Quantum Electronics*, *42*, 639–646.

Moore, R. C. (2007), ELF/VLF wave generation by modulated HF heating of the auroral electrojet, Ph.D. thesis, Stanford University.

Moore, R. C., U. S. Inan, and T. F. Bell (2006), Observations of amplitude saturation in ELF/VLF wave generation by modulated HF heating of the auroral electrojet, *Geophys. Res. Lett.*, *33*, L12,106, doi:10.1029/2006GL025934.

Papadopoulos, K., C. L. Chang, P. Vitello, and A. Drobot (1990), On the efficiency of ionospheric ELF generation, *Radio Science*, *25*, 1311–1320.

Papadopoulos, K., T. Wallace, M. McCarrick, G. M. Milikh, and X. Yang (2003), On the efficiency of ELF/VLF generation using HF heating of the auroral electrojet, *Plasma Physics Reports*, *29*(7), 561–565, doi:10.1134/1.1592554.

Papadopoulos, K., T. Wallace, G. M. Milikh, W. Peter, and M. McCarrick (2005), The magnetic response of the ionosphere to pulsed HF heating, *Geophysical Research Letters*, *32*, L13,101, doi:10.1029/2005GL023185.

Paschal, E. W. (1988), The design of broad-band VLF receivers with air-core loop antennas, internal Stanford Report.

Pasko, V. P., and U. S. Inan (1994), Recovery signatures of lightning-associated VLF perturbations as a measure of the lower ionosphere, *J. Geophys. Res.*, *99*, 17,523–17,538, doi:10.1029/94JA01378.

Pirjola, R., and A. Viljanen (1998), Complex image method for calculating electric and magnetic fields produced by an auroral electrojet of finite length, *Annales Geophysicae*, *16*, 1434–1444.

Platino, M., U. Inan, T. Bell, J. Pickett, E. Kennedy, J. Trotignon, J. Rauch, and P. Canu (2004), Cluster observations of ELF/VLF signals generated by modulated heating of the lower ionosphere with the HAARP HF transmitter, *Annales Geophysicae*, *22*, 2643–2653.

Platino, M., U. S. Inan, T. F. Bell, M. Parrot, and E. J. Kennedy (2006), DEME-TER observations of ELF waves injected with the HAARP HF transmitter, *Geophys. Res. Lett.*, *33*, L16,101, doi:10.1029/2006GL026462.

Potemra, T. A., and A. J. Zmuda (1970), Precipitating energetic electrons as an ionization source in the midlatitude nighttime D region., *J. Geophys. Res.*, *75*, 7161–7167.

Poulsen, W. L. (1991), Modeling of very low frequency wave propagation and scattering within the earth-ionopshere waveguide in the presence of lower ionospheric disturbances, Ph.D. thesis, Stanford University.

Ratcliffe, J. A. (1972), *An Introduction to the Ionosphere and Magnetosphere*, Cambridge University Press.

Reid, G. C. (1976), Ion chemistry in the D region, *Advanced Atomic Molecular Physics*, *12*, 375–413.

Rietveld, M. T., H. Kopka, E. Nielsen, P. Stubbe, and R. L. Dowden (1983), Ionospheric electric field pulsations - a comparison between VLF results from an ionospheric heating experiment and STARE, *J. Geophys. Res.*, *88*, 2140–2146.

Rietveld, M. T., H. Kopka, and P. Stubbe (1986), D-region characteristics deduced from pulsed ionospheric heating under auroral electrojet conditions, *Journal of Atmospheric and Terrestrial Physics*, *48*, 311–326.

Rietveld, M. T., H.-P. Mauelshagen, P. Stubbe, H. Kopka, and E. Nielsen (1987), The characteristics of ionospheric heating-produced ELF/VLF waves over 32 hours, *J. Geophys. Res.*, *92*, 8707–8722.

Rodriguez, J. V. (1994), Modification of the earth's ionosphere by very-low frequency transmitters, Ph.D. thesis, Stanford Unversity.

Rodriguez, J. V., U. S. Inan, and T. F. Bell (1994), Heating of the nighttime D region by very low frequency transmitters, *J. Geophys. Res.*, *99*, 23,329–23,338.

Sechrist, C. F., Jr. (1974), Comparisons of techniques for measurement of D-region electron densities, *Radio Science*, *9*, 137–149.

Shafer, D. (1992), *AGO VLF Receiver Field Manual*, Stanford University.

Stubbe, P. (1996), Review of ionospheric modification experiments at Tromsø , *Journal of Atmospheric and Terrestrial Physics*, *58*, 349–368.

Stubbe, P., and H. Kopka (1977), Modulation of polar electrojet by powerful HF waves, *J. Geophys. Res.*, *82*, 2319–2325.

Stubbe, P., H. Kopka, and R. L. Dowden (1981), Generation of ELF and VLF waves by polar electrojet modulation experimental results, *J. Geophys. Res.*, *86*, 9073–9078.

Stubbe, P., H. Kopka, M. T. Rietveld, and R. L. Dowden (1982), ELF and VLF wave generation by modulated HF heating of the current carrying lower ionosphere, *Journal of Atmospheric and Terrestrial Physics*, *44*, 1123–1131.

Stutzman, W. L., and G. A. Thiele (1998), *Antenna Theory and Design*, 2 ed., John Wiley & Sons, Inc.

Taflove, A., and S. C. Hagness (2000), *Computational Electrodynamics: The Finite-Difference Time-Domain Method*, 2 ed., Artech House.

Tascione, T. F. (1994), *Introduction to the Space Enviroment*, Krieger Publishing Company, Malabar, FL, USA.

Tomko, A. A. (1981), Nonlinear phenomena arising from radio wave heating of the lower ionosphere, Ph.D. thesis, The Pennysylvania State University.

Tomko, A. A., A. J. Ferraro, and H. S. Lee (1980), D region absorption effects during high-power radio wave heating, *Radio Science*, *15*, 675–682.

Wait, J. R. (1957), The attenuation vs frequency characteristics of VLF radio waves, in *Proceedings of the IRE*.

Wait, J. R., and K. P. Spies (1964), Characteristics of the earth-ionosphere waveguide for VLF radio waves, *Tech. Rep. 300*, National Bureau of Standards.

Watt, A. D. (1967), *V.L.F. Radio Engineering*, 1 ed., Pergamon Press.

Werner, D. H., and A. J. Ferraro (1990), Mapping of the polar electrojet current down to ionospheric D region altitudes, *Radio Science*, *25*, 1375–1386.

Zhou, H. B., K. Papadopoulos, A. S. Sharma, and C. L. Chang (1996), Electromagnetohydrodynamic response of a plasma to an external current pulse, *Physics of Plasmas*, *3*, 1484–1494.